AUTONOMOUS CARRIER LANDING OF A FIXED-WING UAV WITH AIRBORNE DECK MOTION ESTIMATION

by

METIN KUS

Presented to the Faculty of the Graduate School of
The University of Texas at Arlington in Partial Fulfillment
of the Requirements for the Degree of

MASTER OF SCIENCE IN AEROSPACE ENGINEERING

THE UNIVERSITY OF TEXAS AT ARLINGTON

December 2019

To my parents, Fatma and Ozkan

and sisters, Merve and Busra

ACKNOWLEDGEMENTS

First of all, I would like to express my most profound appreciation to Turkish Aerospace Industries, Inc. and those who participated in this sponsorship program for making this research possible. I am especially grateful to Dr. Atilla Dogan for his efforts and dedication in initiating and leading this program. I am forever in debt to my superiors Dr. Mustafa Cavcar, Dr. Erhan Solakoglu, Cem Talip Ondes, and Dr. Kagan Cakir of Turkish Aerospace Industries, Inc. for allowing me to join this program and tolerating my absence. I want to thank my colleagues, Dr. Ender Ozden, Dr. Kutlay Odaci, Tolga Ciftci, Huseyin Boyaci, Ali Polat, Erhan Feyzioglu, and Nermin Ugur, for their encouragement and understanding.

Amongst many individuals who have helped me in this journey, I am most thankful to my advisor, one of the smartest people I know, Dr. Kamesh Subbarao for his invaluable guidance. I also wish to express my gratitude to Dr.Animesh Chakravarthy for participating in my thesis committee. The knowledge I gathered in his Guidance, Navigation and Control Systems class has been the backbone of this study. I also can't help but mention my gratitude to Dr. Christopher M. Elliot of Skunk Works at Lockheed Martin Corporation for his interest and feedback at the initial stages of this study.

I thank Yuchun Shih and my brothers for their support, encouragement, and assistance in proofreading.

Finally, I thank all my teachers from first grade to this day and everyone who has helped me in this research whose names are not mentioned.

November 26, 2019

ABSTRACT

AUTONOMOUS CARRIER LANDING OF A FIXED-WING UAV WITH AIRBORNE DECK MOTION ESTIMATION

METIN KUS, M.S. Aerospace Engineering

The University of Texas at Arlington, 2019

Supervising Professor: Dr. Kamesh Subbarao

This study focuses on the design, implementation, and evaluation of an autonomous carrier landing system featuring an airborne deck motion estimation module. The three-dimensional dynamics of a fixed-wing UAV with the actuator and engine dynamics are considered. A carrier motion model that accounts for the perturbations caused by various sea states is built.

An airborne measurement system, which is composed of a calibrated camera and light-emitting beacons, is utilized to detect several coplanar target points on the moving carrier deck. The known correspondence between the locations of the target points and their coordinates on the focal plane of the camera is exploited in the estimation of the desired touchdown point location and runway attitude. The estimation problem is posed as a nonlinear least-squares problem where the error between the actual value and a current estimate of the measurement is minimized in successive iterations. A second-order, low-pass filter is employed to estimate the velocity of the desired touchdown point.

A reference trajectory is generated based on the estimated motion of the desired touchdown point and a glide path. The dynamic inversion technique is used in the derivation of guidance laws to produce a flight-path command to achieve the reference trajectory. A Linear-Quadratic-Integral (LQI) optimal controller is designed to track the flight-path command and stabilize the aircraft around an equilibrium point.

The system is evaluated through simulation. Monte Carlo simulations for various sea states with randomized initial conditions demonstrate robustness, ensuring a wide range of initial conditions and possible scenarios are covered. The system performance is shown to be satisfactory based on several figures of merit, including boarding rate, landing dispersion, angular alignment, and impact velocity even in the worst sea condition considered in this study. Also, the efficiency of the estimation algorithm indicates the feasibility of real-time implementations.

In the navigation system, a Position Sensing Diode (PSD) is located on the focal plane of the camera to detect the modulated light emitted by the beacons. The system performance is evaluated for a range of sampling rates of the PSD. Monte Carlo simulations indicate satisfactory performance for a wide range of sampling rates, from $5\,Hz$ to $100\,Hz$.

TABLE OF CONTENTS

ACKNOWLEDGEMENTS iv

ABSTRACT v

LIST OF ILLUSTRATIONS x

LIST OF TABLES xiii

Chapter Page

1. INTRODUCTION 1

1.1 Background and Motivation 1

1.2 Related Work 3

1.3 Thesis Outline 5

2. PROBLEM DESCRIPTION 6

2.1 Problem Components 6

2.2 Nomenclature 7

2.3 Physical Models 9

2.4 Objective and System Architecture 10

2.5 Figures of Merit 11

3. SYSTEM DYNAMICS 15

3.1 Aircraft Carrier Dynamics 15

3.2 Aircraft Dynamics 20

3.2.1 Equations of Motion 20

3.2.2 Aerodynamic Model 22

3.2.3 Actuator and Engine Models 25

4. REFERENCE TRAJECTORY AND GUIDANCE 28

4.1 Landing Kinematics 28
4.2 Reference Trajectory Generation 30
4.3 Guidance Laws 32
4.3.1 Angle-Based Guidance 34
4.3.2 Position-Based Guidance 35
4.3.3 Guidance Strategy 36
5. CONTROL SYSTEM 38
5.1 Linear Model 38
5.1.1 Steady-State Flight and Equilibrium 40
5.1.2 Linearization 44
5.2 Appended Dynamics 46
5.3 Controller 47
5.3.1 Servo System Architecture and Error Dynamics 47
5.3.2 Linear Quadratic Integral Optimal Controller 49
5.3.3 Weighting Matrices 51
6. DECK MOTION ESTIMATION 54
6.1 Introduction 54
6.2 Position and Attitude Estimation 55
6.2.1 Observation Model 57
6.2.2 Nonlinear Least Squares Estimation 59
6.2.3 System Configuration 61
6.3 Velocity Estimation 63
7. RESULTS AND DISCUSSION 65
7.1 Deck Motion Estimation 68
7.2 Autonomous Carrier Landing System Performance 70
7.2.1 Single Simulation Time Histories 70

7.2.2 A Monte Carlo Approach 73
8. CONCLUDING REMARKS AND FUTURE WORK 96
REFERENCES 101
BIOGRAPHICAL STATEMENT 107

LIST OF ILLUSTRATIONS

Figure		Page
2.1	Landing geometry	7
2.2	Schematic of the CVN-65 Enterprise [20]	9
2.3	General dimensions of the SIAI Marhetti S211 aircraft [21]	10
2.4	Overall system architecture	11
2.5	Landing area	14
3.1	Free-floating body motions caused by wave excitation [23]	16
3.2	The influence of sea states on the motion of the carrier's center of gravity	19
3.3	The influence of sea states on the motion of the desired touchdown point	20
3.4	Structure of the actuators and engine model	26
4.1	Representation of $\boldsymbol{x}_1 = \begin{bmatrix} d & \lambda & \eta \end{bmatrix}^T$ and $\boldsymbol{x}_{1c} = \begin{bmatrix} d_c & \lambda_c & \eta_c \end{bmatrix}^T$	29
4.2	Range dependent sensitivity of angle-based guidance law	33
5.1	Linearization about point A [31]	39
5.2	Block diagram for a type 1 servo system with integral compensator [30]	48
6.1	Vision-based measurement system	55
6.2	Object space to image plane projection for a pinhole camera model	57
6.3	NLS algorithm [44]	62
6.4	Locations of the beacons on the carrier deck	63
7.1	Touchdown condition	65
7.2	Zero-crossing in z-axis	66
7.3	Estimation of the inertial position of the desired touchdown point	78
7.4	Estimation of the attitude of the runway with respect to inertial frame	79

7.5 Estimation of the inertial velocity of the desired touchdown point . . 80
7.6 Number of iterations for $\varepsilon = 10^{-7}$ 81
7.7 (a) The mean and (b) the standard deviation of the deck motion estimation error calculated from 100 carrier landing simulations 82
7.8 The maximum number of iterations in each time step for 100 carrier landings 83
7.9 Time histories of components of $\boldsymbol{x}_1$; distance (d), elevation angle(λ) and azimuth angle(η) at sea state 6 84
7.10 Time histories of components of $\boldsymbol{x}_5$; longitudinal ($(\boldsymbol{x}_5)_x$), lateral ($(\boldsymbol{x}_5)_y$) and vertical($(\boldsymbol{x}_5)_z$) at sea state 6 85
7.11 Time histories of components of $\boldsymbol{x}_2$; velocity (V), course angle (χ) and flight-path angle (γ) at sea state 6 86
7.12 Time histories of flight-path commands generated by angle-based and position-based guidance laws at sea state 6 87
7.13 Time histories of components of $\boldsymbol{x}_3$; roll angle (ϕ), angle of attack (α) and sideslip angle (β) at sea state 6 88
7.14 Time histories of components of $\boldsymbol{x}_4$; angular velocities about body-fixed axes, p, q and r at sea state 6 89
7.15 Time histories of components of $\boldsymbol{\delta}$; throttle (δ_t), elevator deflection (δ_e), aileron deflection (δ_a) and rudder deflection (δ_r) at sea state 6 90
7.16 Time histories of components of $\dot{\boldsymbol{\delta}}$; throttle rate($\dot{\delta}_t$), elevator deflection rate ($\dot{\delta}_e$), aileron deflection rate ($\dot{\delta}_a$) and rudder deflection rate ($\dot{\delta}_r$) at sea state 6 91
7.17 Landing dispersion at sea state 0 92
7.18 Landing dispersion at sea state 4 92
7.19 Landing dispersion at sea state 5 93

7.20 Landing dispersion at sea state 6 93
7.21 Landing region at sea state 0 for various PSD sampling rates 94
7.22 Landing region at sea state 4 for various PSD sampling rates 94
7.23 Landing region at sea state 5 for various PSD sampling rates 95
7.24 Landing region at sea state 6 for various PSD sampling rates 95

LIST OF TABLES

Table		Page
3.1	The World Meteorological Organization sea state code [26]	17
3.2	Perturbation motion constants for various sea states [7, 8, 25]	18
3.3	Sign convention for control surfaces	24
3.4	Data for SIAI Marchetti S211 [21]	25
3.5	Actuator and engine Model specifications	27
5.1	Results of the trim algorithm	43
5.2	Maximum allowable deviations	53
7.1	Landing statistics	75

CHAPTER 1

INTRODUCTION

1.1 Background and Motivation

An increased range of operation has always been one of the most important goals of aviation. The appearance of aircraft carriers in armed forces has increased the range of operation beyond measure by allowing aircraft to take off and land closer to their targets. More sorties have also been made possible in a given time due to the shortened distance between aircraft and targets.

Besides all the strategical advantages, aircraft carriers have given rise to some technical difficulties, and the most challenging task in naval operations is considered to be the landing. Due to the restrictions on the touchdown area and short runway, the aircraft must follow a glide path with a small margin of error while maintaining a high angle of attack and controlling airspeed. The effectiveness of the control surfaces is reduced due to low airspeed and high angle of attack. The motion of the deck makes the task even more challenging because the glide path and the touchdown area moves in space as the deck moves due to the current state of the sea. The motion of the deck relative to the aircraft right before the touchdown may result in an extremely harsh landing, which may fail the aircraft structure. Even small vertical displacements caused by pitch and heave motions of the carrier may lead to catastrophic longitudinal landing error considering the small value of the flight-path angle during the descent. Also, angled runways of the carriers make the landing task very difficult since the aircraft must descend along a glide path that is not aligned with the carrier's longitudinal axis.

All these difficulties combined make the landing on an aircraft carrier a perilous task for human pilots. In a classical manned carrier landing operation, three main concerns of the human pilot are the meatball (also called the Optical Landing System), lineup, and airspeed [1]. The meatball is an optical device located usually on the port side of the carrier deck. The human pilot must follow the visual cues of the meatball and lineup at the same time to ensure the aircraft is within the glide slope beam. The beam extends aft from the desired touchdown point and becomes narrower towards the runway; hence, corrections near touchdown become extremely difficult. Furthermore, all these considerations are highly coupled. Lineup corrections cause both glide slope and airspeed problems. For example, the additional drag introduced by an aileron deflection for a lineup correction may cause the approach to be low and slow. Therefore, a lineup correction must be accompanied by an adequate throttle deflection.

Even the minimum skill set required for human pilots to achieve successful carrier landings consistently can only be acquired through hard training and experience, which requires many hours of flight and is a financial burden. The U.S. Navy announced that most of the accidents between 1947 and 1988 are concentrated on takeoff and landing operations, and they are closely related to human factors [2, 3]. The accidents that might occur during a carrier landing operation include but are not limited to ramp strikes, liquid landings, landing gear failures, arresting gear failures, and in-flight wire engagement. These accidents often have catastrophic consequences such as the loss of the pilot, crew members, and aircraft. It is evident from the complexity of the task and irreversible consequences associated with the accidents that the development of autonomous carrier landing systems is a necessity.

1.2 Related Work

Many autonomous carrier landing systems have been proposed in the past. The classical Navy F/A-18A Automatic Carrier Landing System (ACLS) is defined in [4] as an integrated control system with a shipboard tracking radar and digital computer. The shipboard radar measures the aircraft position and calculates pitch and bank steering commands that are transmitted to the aircraft using a radio data link. The aircraft flight control system uses these commands together with an Approach Power Compensation System (APCS) to generate flight and thrust control. It is designed to reduce the load on the human pilot under suboptimal conditions such as low-visibility, night operations, and high sea states. Lee et al. [2] proposed sliding mode guidance and control, which incorporates a deck motion compensation logic that predicts the location of the desired touchdown point at touchdown. Another integrated carrier landing system is suggested by Zhen et al. [5] which employs particle filtering method for carrier motion prediction and an optimal preview control (OPC) scheme for an integrated guidance and control (IGC) module. Nonlinear dynamic inversion control theory was also applied in the guidance and control of carrier landing; however, the fact that this method relies on the exact system model caused performance degradation in the presence of sea state disturbances and other uncertainties [6, 7, 5]. Lu and Liu [8] addressed this problem in their study. They suggested a L_1 adaptive controller augmenting a dynamic inversion controller to account for matched and unmatched system uncertainties, which may cause degradation of performance on the unaugmented, baseline controller.

Although various autonomous carrier landing systems are found in the literature, most of them relied solely on a shipboard measurement system and a data link through which information related to deck motion is transferred to generate control action. The design of an airborne measurement system for navigation to eliminate

the necessity for healthy communication between the carrier and the aircraft has also drawn attention in the field. The studies that incorporated airborne measurement systems for landing predominantly employed vision-based navigation systems since it is a cheap, passive, and information-rich option [9, 10, 11, 12, 13, 14]. Vision-based navigation was used for both classical landing with a stationary touchdown point [9, 11, 12, 13] and carrier landing with a nonstationary touchdown point [10, 15, 14]. Yakimenko et al. [14] proposed a numerical solution to the problem of determining the relative position and orientation of a UAV with respect to a ship using three visible points with known separation. Although simulation and flight test results were presented, the flight test involved a stationary runway. Hence, the robustness of the system concerning sea state disturbances was not evaluated. Meng et al. [15] used four coplanar point correspondences to solve the same estimation problem. The Pose from Orthographic Projection and Scaling with Iterations (POSIT) algorithm was utilized for this purpose. The estimation results were presented using a Monte Carlo approach, and high performance was observed; however, the estimation results were limited to approximately $200\,m$ of distance to the touchdown. No results or discussion regarding the estimation performance in terms of robustness near touchdown was found. The performance of the Guidance, Navigation and Control (GNC) system in terms of the landing error was given only for a single simulation, which may not reflect the overall GNC system performance. The study focused almost purely on the estimation performance with minimal emphasis on controller performance. Hence, the interoperability and robustness of the deck motion estimation and control systems were not shown for a range of initial conditions and sea states by presenting landing dispersion and boarding rate statistics. Coutard et al. [10] proposed a new set of visual features from a camera view of the deck to be used in the state feedback con-

trol law. Similarly, the results were provided for a single simulation and satisfactory performance was achieved.

1.3 Thesis Outline

Chapter 2 forms a basis for the rest of the document by describing the components of the carrier landing problem. The physical reference models for the carrier and aircraft are given. The nomenclature that is used throughout the document is explained. The objective of the study and the performance criteria upon which a carrier landing task might be evaluated are also discussed in Chapter 2. The carrier, aircraft, actuator, and engine dynamics are presented in Chapter 3. Chapter 4 involves trajectory planning and guidance phases. The relative motion between the carrier and the aircraft is studied in this chapter, allowing the generation of a reference trajectory. A guidance strategy and guidance laws to achieve the reference trajectory are also presented. Chapter 5 contains a theoretical development for the controller. Steady-state flight conditions, equilibrium points, and controller structure are discussed. A navigation strategy is proposed in Chapter 6. An observation model and a deck motion estimation algorithm are implemented in the system to estimate the deck motion via an airborne vision-based sensor and target points on the deck with known correspondences. The system performance is presented and discussed using simulation results in Chapter 7. Monte Carlo simulations are performed at different sea states covering a wide range of initial conditions. Concluding remarks are made in Chapter 8, and possible ways to improve the system performance are discussed.

CHAPTER 2

PROBLEM DESCRIPTION

2.1 Problem Components

In this section, the geometry of the carrier landing in three-dimensional space is explained. Three main components of this problem are the aircraft, the aircraft carrier, and the Earth. These components are represented through right-handed, Cartesian, body-fixed frames. The origin of the aircraft's body-fixed frame (denoted as A-frame) is attached to its center of gravity. A Forward-Right-Down (FRD) coordinate system is chosen in the body [16]. There are two body-fixed frames associated with the carrier, which are ship's body-fixed frame (denoted as S-frame) and deck's body-fixed frame (denoted as D-frame). The origin of the S-frame is fixed at the carrier's center of gravity. The x-axis of the S-frame is parallel to the longitudinal axis of the carrier, and the z-axis is parallel to the inward-facing unit normal vector of the deck surface. The origin of the D-frame coincides with the desired touchdown point on the runway. Its x-axis is parallel to the runway centerline. The z-axis is parallel to the inward-facing unit normal vector of the deck surface, just like the z-axis of the S-frame. A tangent-plane coordinate system with North-East-Down (NED) orientation on the Earth surface is selected as the inertial frame. This coordinate system is compatible with the non-rotating, flat-Earth equations of motion [16].

A schematic that describes the geometry of the landing problem is given in Figure 2.1. In this figure, three main components and corresponding body frames are visualized, the position vectors between the body frames are drawn as well as the inertial position vectors of each component.

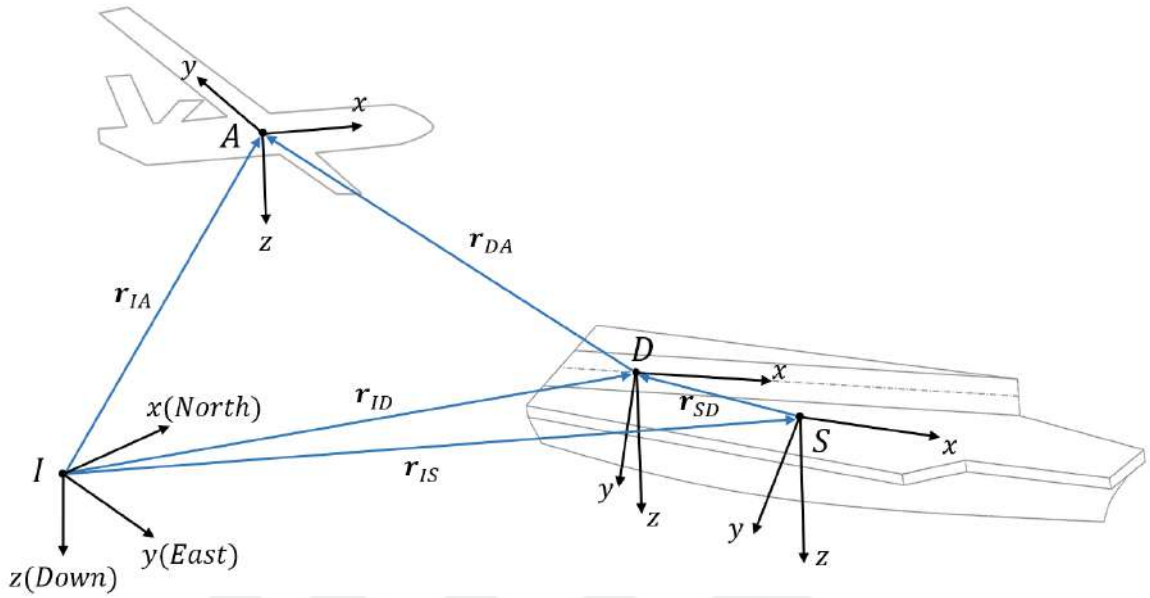

Figure 2.1. Landing geometry.

2.2 Nomenclature

In this study, a consistent nomenclature is applied. Scalars are denoted by italic and lowercase letters, vectors are denoted by bold-italic and lowercase letters, matrices are denoted by bold-italic and uppercase letters.

Position vectors are denoted by $\boldsymbol{r}$. The subscript of a position vector consists of two capital letters. These capital letters are associated with the origins of the frames, and the first and the second letters denote the tail and head of the position vector, respectively. A superscript on a position vector specifies the frame in which the vector components are expressed. A similar method is used to express angular quantities. A subscript involves two letters each associated with a frame, and the angular quantity is measured from the second frame to the first frame. For Euler angles representation, the inertial frame is usually omitted in the subscript such that, for example, subscript AI is written as A.

Vectrix formalism from [17] is utilized to express and manipulate the vectors in matrix form. The vectrix of a frame, let us consider the A-frame in this example, is defined as

$$[\boldsymbol{A}] = \begin{bmatrix} i_A & j_A & k_A \end{bmatrix}^T \tag{2.1}$$

where i_A, j_A, k_A are the unit normal vectors in x,y and z directions, respectively. A vector, let us consider $\boldsymbol{r}_{IA}$, can be written in terms of its representation in the A-frame as

$$\boldsymbol{r}_{IA} = [\boldsymbol{A}]^T \, \boldsymbol{r}^A_{IA} \tag{2.2}$$

The rotation between the vectrices of two frames are defined by a rotation matrix as

$$[\boldsymbol{A}] = \boldsymbol{R}_{AD} \, [\boldsymbol{D}] \tag{2.3}$$

where a rotation matrix is given by the Euler angles of the rotation in 3-2-1 sequence as [17]

$$\begin{aligned} \boldsymbol{R} =& \boldsymbol{R}(\phi, \theta, \psi) \\ =& \left[\begin{array}{c|c|c} \cos\theta\cos\psi & \cos\theta\sin\psi & -\sin\theta \\ \hline -\cos\phi\sin\psi & \cos\phi\cos\psi & \\ +\sin\phi\sin\theta\cos\psi & +\sin\phi\sin\theta\sin(\psi) & \sin\phi\cos\theta \\ \hline \sin\phi\sin\psi & -\sin\phi\cos\psi & \\ +\cos\phi\sin\theta\cos\psi & +\cos\phi\sin\theta\sin\psi & \cos\phi\cos\theta \end{array}\right] \end{aligned} \tag{2.4}$$

The nomenclature and vectrix formalism used in this study makes it very easy for the reader to follow the equations presented in the following chapters. Note that representation of a vector can easily be transferred between frames using rotation matrices and translation vectors. For example, $\boldsymbol{r}^D_{ID} = \boldsymbol{R}_{DI} \, \boldsymbol{r}^I_{ID} = \boldsymbol{R}_{DI} \, (\boldsymbol{r}^I_{IA} + \boldsymbol{r}^I_{AD}) = \boldsymbol{R}_{DI} \, (\boldsymbol{R}^T_{SI} \, \boldsymbol{r}^S_{IA} + \boldsymbol{R}^T_{AI} \, \boldsymbol{r}^A_{AD})$.

2.3 Physical Models

The CVN-65 Enterprise aircraft carrier is used as the reference carrier model in this study. A schematic of top and side views of the CVN-65 is given in Figure 2.2. The overall length and extreme beam of the carrier are given as $331\,m$, and $75.6\,m$ [18]. Other important quantities, such as the angle between longitudinal axes of the runway and carrier, denoted as ψ_{DS}, and the translation vector between S-frame and D-frame, denoted as $\boldsymbol{r}_{SD}^{S}$, are given as $-9\,deg$ and $\begin{bmatrix} -68 & -3 & -20 \end{bmatrix}^T\,m$ [19].

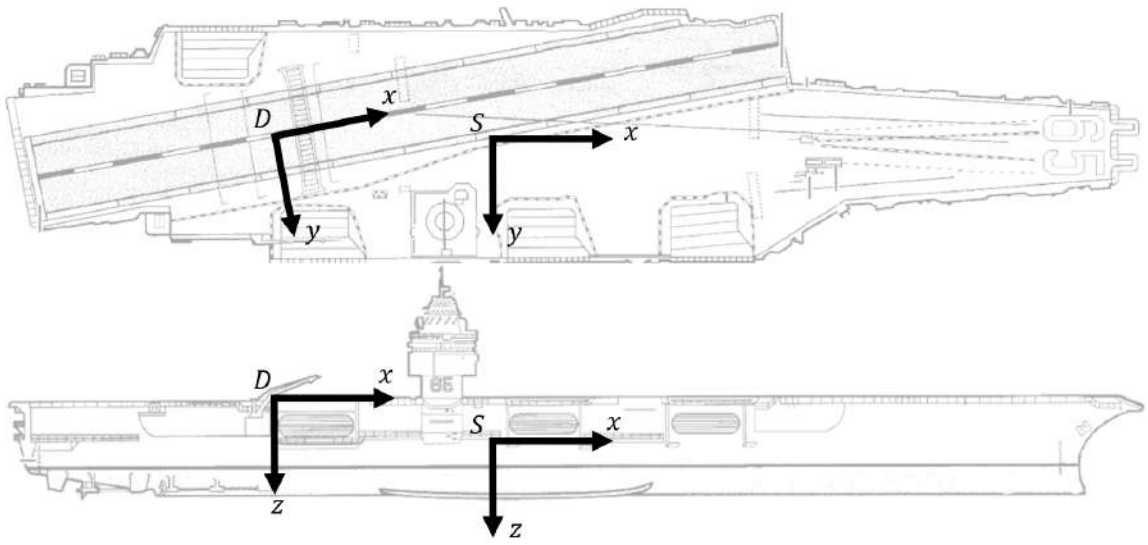

Figure 2.2. Schematic of the CVN-65 Enterprise [20].

Thee SIAI Marchetti S211 aircraft model is used as a reference aircraft model in this study. General dimensions of this aircraft are given in Figure 2.3. This aircraft is chosen due to its longitudinal maneuverability characteristics and availability of aerodynamics data. General dimensions of SIAI Marchetti also makes it a suitable candidate for carrier landing operations.

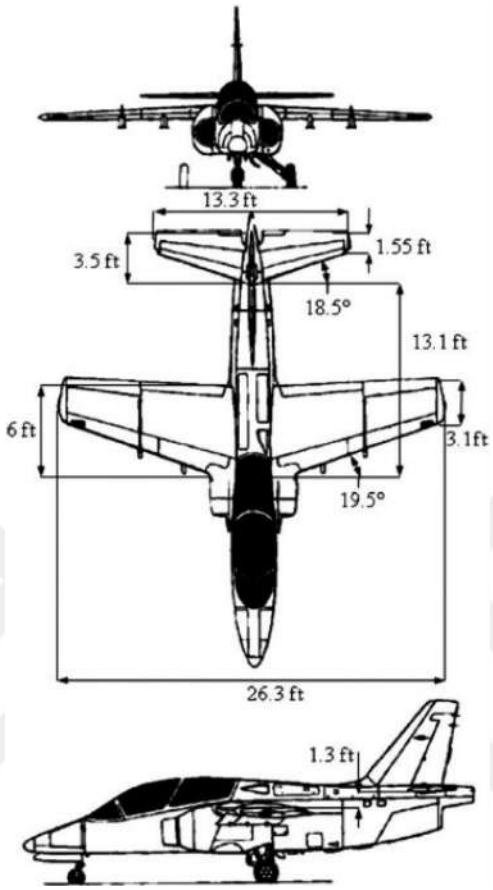

Figure 2.3. General dimensions of the SIAI Marhetti S211 aircraft [21].

2.4 Objective and System Architecture

The objective of this study is to design, implement, and evaluate a guidance and control system driven by airborne measurement and estimation of deck motion for carrier landing operations of fixed-wing UAVs.

A system with the structure given in Figure 2.4 is constructed to accomplish this objective. In this system, a vision-based measurement model detects the known target points located on the deck. An estimation algorithm estimates the position of the desired touchdown point and attitude of the runway using the image coordinates of these target points. A low-pass filter is employed to estimate the velocity from the estimated position. The estimated states of the deck motion are used to generate a

reference trajectory for the aircraft. A guidance law generates a flight-path command to compensate for the difference between the actual trajectory of the aircraft and the reference trajectory. A control system produces control input commands to track the flight-path command and stabilize the aircraft.

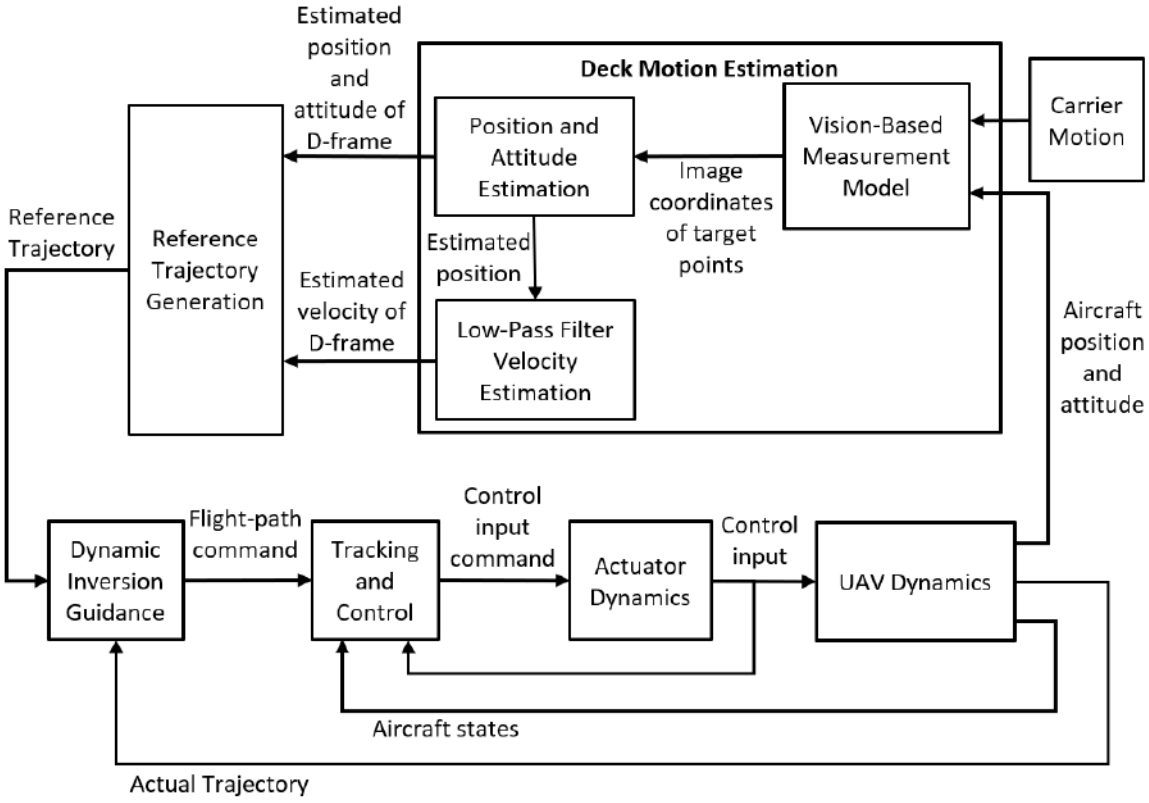

Figure 2.4. Overall system architecture.

2.5 Figures of Merit

Performance criteria upon which the system performance is evaluated are discussed in this section. The ultimate indicator of the system performance is the boarding rate. The boarding rate is defined as the ratio of successful to unsuccessful attempts. Several other figures of merit can be derived from the boarding rate. These

figures of merit are necessary to be able to quantify the success of an attempt. In order for an attempt to be reckoned as successful:

- Landing error must be lower than the maximum allowable limits that are dictated by the dimensions of the runway and landing area.
- The relative Euler angles between the aircraft and the runway at touchdown must be lower than maximum allowable limits.
- The relative velocity between the aircraft and the touchdown point at impact must be low enough for the structural integrities of the landing and arresting gears.

The dimensions of the landing area of the CVN-65 carrier are given in Figure 2.5. Four arresting wires, which are $40\,ft \approx 12\,m$ apart form the landing area [19]. The desired touchdown point is specified as the center of the four arresting wires. The width of the runway is assumed to be $20\,m$. The safe landing zone is assumed to have a width of $16\,m$. In this study, any landing outside the safe landing zone is considered unsuccessful.

The relative Euler angles from the D-frame to the A-frame at touchdown are expected to be $\phi_{AD} = 0\,deg$, $\theta_{AD} = 6\,deg$ and $\psi_{AD} = 0\,deg$ with $\pm 5\,deg$ on the upper and lower bounds for optimal hook engagement and alignment.

The upper limit on the vertical component of the impact velocity is dictated by the structural limits of the landing gear. According to [22], Boeing commercial airplanes have been designed for a $10\,ft/s$ sink rate at or below the maximum design landing weight. The flare maneuver considerably reduces the impact velocity in land-based landing operations; however, this maneuver is not performed in carrier landings due the short runway and required landing precision. Hence, naval fleet aircraft are designed for a higher sink rate. In his study [19], Sweger achieved a relative sink rate of slightly above $10\,ft/s$ with respect to the touchdown point. For this reason,

the upper limit on the vertical component of the relative velocity at the impact is taken as $3\,m/s$ in this study. No information was found regarding the upper limits on the longitudinal and lateral components of the relative velocity at the impact. It is assumed that the arresting gear is designed with a large safety factor, and longitudinal and lateral components are not significant factors. In this study, the impact velocity is not calculated as the relative sink rate between the aircraft and the desired touchdown point due to the rotational motion of the deck and the resulting Coriolis effect. Instead, the relative velocity of the A-frame with respect to the D-frame is expressed in the D-frame so that the vertical component is in the direction of the unit normal vector of the deck surface. The position vector from the D-frame to the A-frame can be expressed in the D-frame as

$$\boldsymbol{r}_{DA}^{D} = \boldsymbol{R}_{DI}\boldsymbol{r}_{DA}^{I} = \boldsymbol{R}_{DI}(\boldsymbol{r}_{IA}^{I} - \boldsymbol{r}_{ID}^{I}) \tag{2.5}$$

The derivative of Equation 2.5 gives the relative velocity in the D-frame as

$$\dot{\boldsymbol{r}}_{DA}^{D} = \dot{\boldsymbol{R}}_{DI}(\boldsymbol{r}_{IA}^{I} - \boldsymbol{r}_{ID}^{I}) + \boldsymbol{R}_{DI}(\dot{\boldsymbol{r}}_{IA}^{I} - \dot{\boldsymbol{r}}_{ID}^{I}) \tag{2.6}$$

Note that the first term in Equation 2.6 is for the Coriolis effect due to the landing error, and the second term is for the relative velocity of the aircraft with respect to the desired touchdown point.

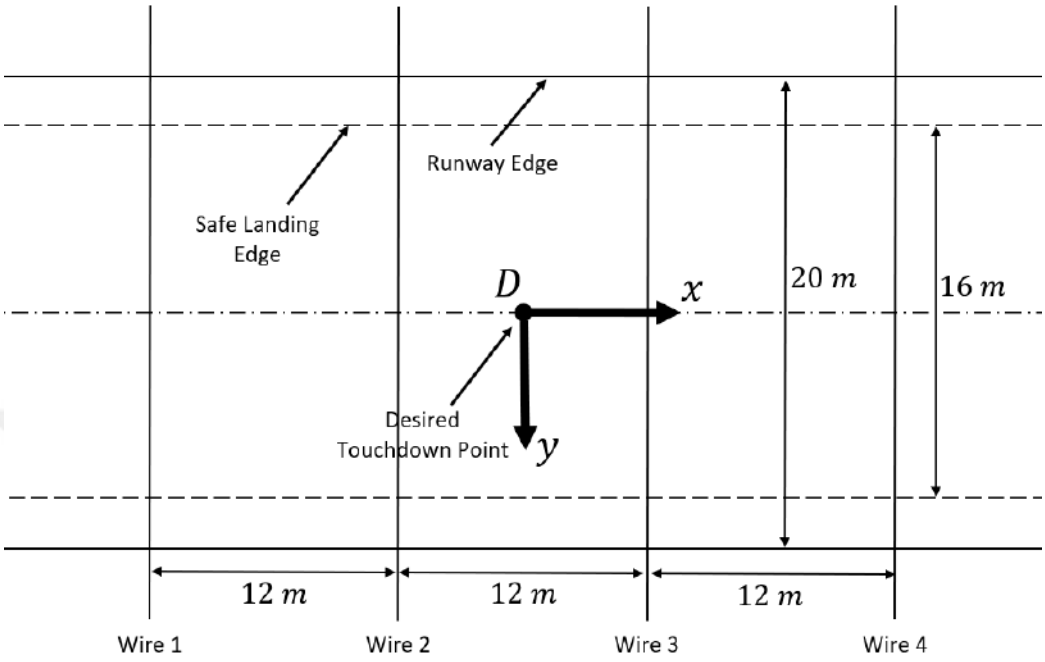

Figure 2.5. Landing area.

CHAPTER 3

SYSTEM DYNAMICS

3.1 Aircraft Carrier Dynamics

The motion of the carrier is modeled in six degrees of freedom in accordance with [2]. Superposition of the carrier's maneuver and sea state perturbations defines the translational motion of the carrier at its center of gravity. The carrier is assumed to be cruising at a constant speed, V_S, along the longitudinal axis, so the maneuver velocity is expressed in the S-frame as

$$\boldsymbol{V}^S_{man} = \begin{bmatrix} V_S & 0 & 0 \end{bmatrix}^T \tag{3.1}$$

where y and z components are assumed to be negligible. The sea state perturbations are due to the wave excitation. The translational and rotational dynamics of the sea state perturbations are modeled in terms of free-floating body motions, which are illustrated in Figure 3.1. The translational displacements in the S-frame due to the wave excitation are called surge, sway and heave. They refer to back and forth, sideways, and up and down rocking motions of the carrier. These motions are formulated as sinusoidal waves:

$$\boldsymbol{r}^S_{sea} = \begin{bmatrix} r^S_{surge} \\ r^S_{sway} \\ r^S_{heave} \end{bmatrix} = \begin{bmatrix} A_{surge}\sin(w_{surge}t + \Delta_{surge}) \\ A_{sway}\sin(w_{sway}t + \Delta_{sway}) \\ A_{heave}\sin(w_{heave}t + \Delta_{heave}) \end{bmatrix} \tag{3.2}$$

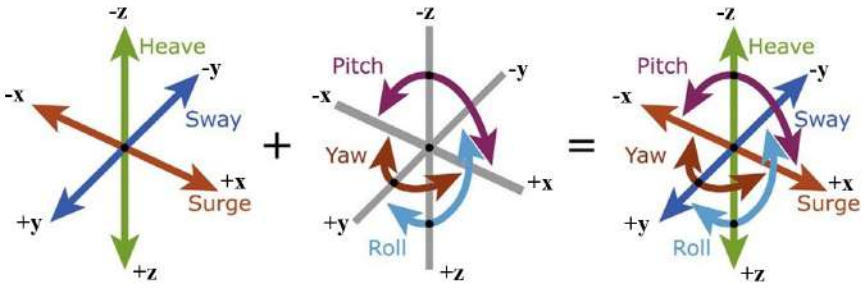

Figure 3.1. Free-floating body motions caused by wave excitation [23].

Once the derivative of Equation 3.2 is taken, the component of the carrier's velocity due to the wave excitation is found as

$$\boldsymbol{V}_{sea}^{S} = \begin{bmatrix} \dot{r}_{surge}^{S} \\ \dot{r}_{sway}^{S} \\ \dot{r}_{heave}^{S} \end{bmatrix} = \begin{bmatrix} A_{surge} w_{surge} \cos(w_{surge} t + \Delta_{surge}) \\ A_{sway} w_{sway} \cos(w_{sway} t + \Delta_{sway}) \\ A_{heave} w_{heave} \cos(w_{heave} t + \Delta_{heave}) \end{bmatrix} \tag{3.3}$$

After the two elements of the velocity of the center of gravity are formulated, they are superposed to find the total velocity in the S-frame as

$$\dot{\boldsymbol{r}}_{IS}^{S} = \boldsymbol{V}_{man}^{S} + \boldsymbol{V}_{sea}^{S} \tag{3.4}$$

The rotation matrix from the inertial frame to the S-frame is used to find the inertial velocity as follows:

$$\dot{\boldsymbol{r}}_{IS}^{I} = \boldsymbol{R}_{SI}^{T} \dot{\boldsymbol{r}}_{IS}^{S} + \dot{\boldsymbol{R}}_{SI}^{T} \boldsymbol{r}_{IS}^{S} \tag{3.5}$$

The rotational motion of the CVN-65 is solely due to the wave excitation. The rotational dynamics of the sea state perturbations are modeled in a similar way to the translational dynamics such that the Euler angle displacements are formulated as sinusoidal waves [2]:

$$\boldsymbol{\Phi}_{S} = \begin{bmatrix} \phi_S \\ \theta_S \\ \psi_S \end{bmatrix} = \begin{bmatrix} A_\phi \sin(w_\phi t + \Delta_\phi) \\ A_\theta \sin(w_\theta t + \Delta_\theta) \\ A_\psi \sin(w_\psi t + \Delta_\psi) \end{bmatrix} \tag{3.6}$$

The Euler rates can be found by taking the derivative of Equation 3.6 as

$$\dot{\mathbf{\Phi}}_S = \begin{bmatrix} \dot{\phi}_S \\ \dot{\theta}_S \\ \dot{\psi}_S \end{bmatrix} = \begin{bmatrix} A_\phi w_\phi \cos(w_\phi t + \Delta_\phi) \\ A_\theta w_\theta \cos(w_\theta t + \Delta_\theta) \\ A_\psi w_\psi \cos(w_\psi t + \Delta_\psi) \end{bmatrix} \tag{3.7}$$

Euler rate equations from [24] are used to convert Euler rates to angular velocities:

$$\boldsymbol{w}_S = \begin{bmatrix} p_S \\ q_S \\ r_S \end{bmatrix} = \begin{bmatrix} 1 & 0 & -\sin\theta_S \\ 0 & \cos\phi_S & \cos\theta_S \sin\phi_S \\ 0 & -\sin\phi_S & \cos\theta_S \cos\phi_S \end{bmatrix} \begin{bmatrix} \dot{\phi}_S \\ \dot{\theta}_S \\ \dot{\psi}_S \end{bmatrix} \tag{3.8}$$

The rotational kinematics of the carrier in the form of Poisson's kinematical equations [16] is given by

$$\dot{\boldsymbol{R}}_{SI} = S(\boldsymbol{w}_S)\boldsymbol{R}_{SI} \tag{3.9}$$

The motion constants which define the amplitudes and frequencies of the sea state perturbations are generated by [25]. The World Meteorological Organization sea state code is adopted to define the sea states. The description and corresponding wave height for each sea state are given in Table 3.1. Only sea states 0, 4, 5, and 6 are considered in this research. The carrier motion constants regarding these sea states are given in Table 3.2. All perturbation amplitudes at sea state 0 are zero.

Table 3.1. The World Meteorological Organization sea state code [26]

Code Figure	**Descriptive Terms**	**Wave Height(in meters)**
0	Calm(glassy)	0
1	Calm(rippled)	0 - 0.1
2	Smooth(wavelets)	0.1 - 0.5
3	Slight	0.5 - 1.25
4	Moderate	1.25 - 2.5
5	Rough	2.5 - 4
6	Very rough	4 - 6

Table 3.2. Perturbation motion constants for various sea states [7, 8, 25]

Sea State	Perturbation	Amplitude	Frequency
4	Surge	0.9546 ft	0.3307 rad/s
	Sway	1.4142 ft	0.3307 rad/s
	Heave	2.2274 ft	0.3491 rad/s
	Roll	0.6223 deg	0.2856 rad/s
	Pitch	0.5162 deg	0.5236 rad/s
	Yaw	0.1800 deg	0.5200 rad/s
5	Surge	1.5203 ft	0.3307 rad/s
	Sway	2.2627 ft	0.3307 rad/s
	Heave	3.5638 ft	0.3491 rad/s
	Roll	0.9829 deg	0.2856 rad/s
	Pitch	0.8202 deg	0.5236 rad/s
	Yaw	0.3075 deg	0.5200 rad/s
6	Surge	2.2840 ft	0.3307 rad/s
	Sway	3.3941 ft	0.3307 rad/s
	Heave	5.3528 ft	0.3491 rad/s
	Roll	1.4425 deg	0.2856 rad/s
	Pitch	1.2374 deg	0.5236 rad/s
	Yaw	0.4350 deg	0.5200 rad/s

So far, the carrier dynamics are formulated at the center of gravity. Although the motion of the desired touchdown point is a function of the motion of the center of gravity, it differs significantly because of the relative position vector between the two points. The motion of the desired touchdown point is calculated assuming the carrier is a rigid body; hence, the representation of relative position vector in the S-frame and the rotation matrix from the S-frame to the D-frame are constant. The inertial position of the desired touchdown point can be calculated using simple vector addition as

$$\boldsymbol{r}_{ID} = \boldsymbol{r}_{IS} + \boldsymbol{r}_{SD} \tag{3.10}$$

Next, the relative position vector is represented in the S-frame to exploit rigid body assumption:

$$\boldsymbol{r}^I_{ID} = \boldsymbol{r}^I_{IS} + \boldsymbol{R}^T_{SI}\boldsymbol{r}^S_{SD} \tag{3.11}$$

Taking the derivative of Equation 3.11 and applying the rigid body assumption, $\dot{\boldsymbol{r}}^S_{SD} = 0$, gives the translational dynamics of the desired touchdown point in the inertial frame as

$$\dot{\boldsymbol{r}}^I_{ID} = \dot{\boldsymbol{r}}^I_{IS} + \dot{\boldsymbol{R}}^T_{SI}\boldsymbol{r}^S_{SD} \tag{3.12}$$

The rotation matrix from the inertial frame to the D-frame is given as

$$\boldsymbol{R}_{DI} = \boldsymbol{R}_{DS}\boldsymbol{R}_{SI} \tag{3.13}$$

The rotational dynamics of the desired touchdown point is found by taking the derivative of Equation 3.13 and substituting Equation 3.9 and $\dot{\boldsymbol{R}}_{SD} = 0$:

$$\dot{\boldsymbol{R}}_{DI} = \boldsymbol{R}_{DS}S(\boldsymbol{w}_S)\boldsymbol{R}_{SI} \tag{3.14}$$

The influence of the sea state on the translational and rotational dynamics of the carrier's center of gravity and desired touchdown point is presented in Figure 3.2 and Figure 3.3, respectively. The initial phase angles Δ_{surge}, Δ_{sway}, Δ_{heave}, Δ_{ϕ}, Δ_{θ}, Δ_{ψ} are all taken as zero and the cruise speed, V_S, is $10\,m/s$.

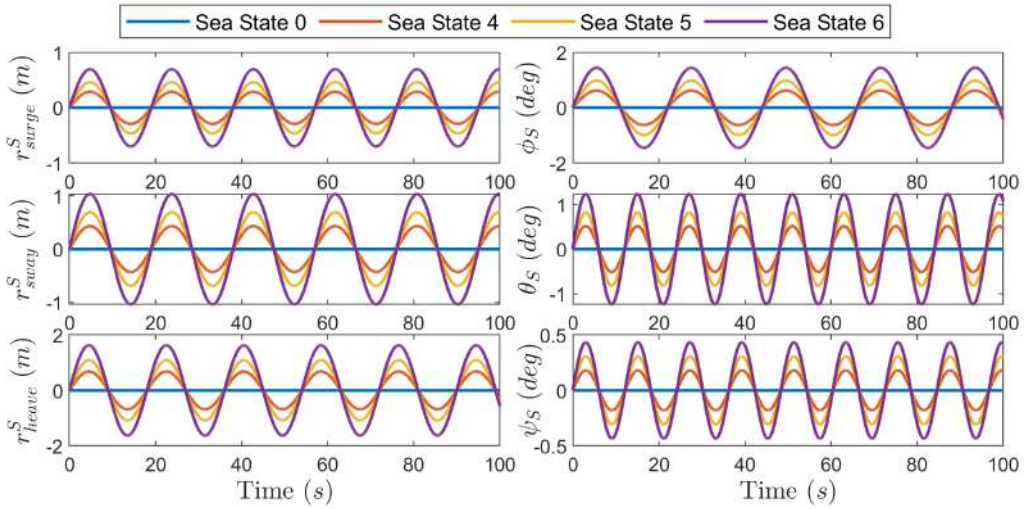

Figure 3.2. The influence of sea states on the motion of the carrier's center of gravity.

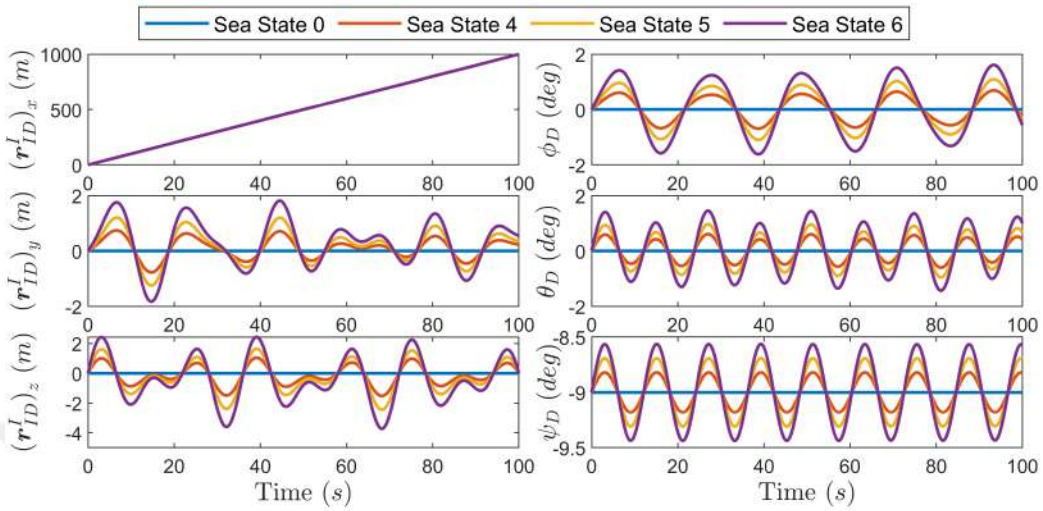

Figure 3.3. The influence of sea states on the motion of the desired touchdown point.

3.2 Aircraft Dynamics

In this section, the modeling phase of the SIAI Marchetti S211 aircraft is explained in detail. The nonlinear equations of motion are presented to define the dynamics of the aircraft in six degrees of freedom. The aerodynamic properties of the aircraft are described. Also, actuators for the control surfaces and an engine model are implemented.

3.2.1 Equations of Motion

The force equations in the wind-axes system and the moment equations in the body-axes system are used [27]. The flat-Earth assumption is made. In the flat-Earth equations, a North-East-Down (NED) coordinate system is fixed in the Earth as the inertial coordinate system. The nonlinear set of equations that describes the state space of the aircraft is presented using the vectors, $\boldsymbol{x}_2 = \begin{bmatrix} V & \chi & \gamma \end{bmatrix}^T$, $\boldsymbol{x}_3 = \begin{bmatrix} \phi & \alpha & \beta \end{bmatrix}^T$, and $\boldsymbol{x}_4 = \begin{bmatrix} p & q & r \end{bmatrix}^T$ [2, 27]:

$$
\begin{aligned}
\dot{\boldsymbol{x}}_2 &= \begin{bmatrix} -g\sin\gamma \\ 0 \\ -\frac{g}{V}\cos\gamma \end{bmatrix} + \begin{bmatrix} \frac{-D+T_{max}\delta_t\cos\alpha\cos\beta}{m} \\ \frac{-Y\cos\phi+L\sin\phi+T_{max}\delta_t(\sin\alpha\sin\phi-\cos\alpha\sin\beta\cos\phi)}{mV\cos\gamma} \\ \frac{Y\sin\phi+L\cos\phi+T_{max}\delta_t(\cos\alpha\sin\beta\sin\phi+\sin\alpha\cos\phi)}{mV} \end{bmatrix} \\
&\triangleq \boldsymbol{f_2} + \boldsymbol{g_2}
\end{aligned} \tag{3.15}
$$

$$
\begin{aligned}
\dot{\boldsymbol{x}}_3 = &\begin{bmatrix} 0 & \sin\gamma+\cos\gamma\sin\phi\tan\beta & \cos\phi\tan\beta \\ 0 & -\frac{\cos\gamma\sin\phi}{\cos\beta} & \frac{\cos\phi}{\cos\beta} \\ 0 & \cos\gamma\cos\phi & -\sin\phi \end{bmatrix} (\boldsymbol{f_2}+\boldsymbol{g_2}) \\
&+ \begin{bmatrix} \frac{\cos\alpha}{\cos\beta} & 0 & \frac{\sin\alpha}{\cos\beta} \\ -\cos\alpha\tan\beta & 1 & -\sin\alpha\tan\beta \\ \sin\alpha & 0 & -\cos\alpha \end{bmatrix} \boldsymbol{x}_4
\end{aligned} \tag{3.16}
$$

$$
\dot{\boldsymbol{x}}_4 = \begin{bmatrix} I_1qr + I_2pq \\ I_5pr + I_6(r^2-p^2) \\ -I_2qr + I_8pq \end{bmatrix} + \begin{bmatrix} I_3 & 0 & I_4 \\ 0 & I_7 & 0 \\ I_4 & 0 & I_9 \end{bmatrix} \begin{bmatrix} M_l \\ M_m \\ M_n \end{bmatrix} \tag{3.17}
$$

where V, χ, γ are the velocity, course angle, and flight-path angle. ϕ, α, β, are the roll angle, angle of attack, and sideslip angle. p, q, r are the components of the angular velocity in the body frame. g is the gravitational acceleration, m is the mass of the aircraft, T_{max} is the maximum thrust and δ_t is the throttle. The inertia terms are

$$
\begin{aligned}
&I_1 = -\frac{I_z(I_z-I_y)+I_{xz}^2}{I_xI_z-I_{xz}^2}, \quad I_2 = \frac{I_{xz}(I_x-I_y+I_z)}{I_xI_z-I_{xz}^2}, \quad I_3 = \frac{I_z}{I_xI_z-I_{xz}^2} \\
&I_4 = \frac{I_{xz}}{I_xI_z-I_{xz}^2}, \qquad I_5 = \frac{I_z-I_x}{I_y}, \qquad I_6 = \frac{I_xz}{I_y} \\
&I_7 = \frac{1}{I_y}, \qquad I_8 = \frac{I_x(I_x-I_y)+I_{xz}^2}{I_xI_z-I_{xz}^2}, \quad I_9 = \frac{I_x}{I_xI_z-I_{xz}^2}
\end{aligned} \tag{3.18}
$$

where I_x, I_y, I_z, I_{xz} are the moment of inertia about the x-axis, the moment of inertia about the y-axis, the moment of inertia about the z-axis and the product of inertia about the xz-plane, respectively.

3.2.2 Aerodynamic Model

The aerodynamic forces and moments that appear in the equations of motion are modeled using the aerodynamic coefficients as [16]

$$\begin{gathered} D = \bar{q}SC_L, \quad L = \bar{q}SC_D, \quad Y = \bar{q}SC_Y \\ M_l = \bar{q}SbC_l, \quad M_m = \bar{q}S\bar{c}C_m, \quad M_n = \bar{q}SbC_n \end{gathered} \tag{3.19}$$

where $\bar{q}$ and S are the dynamic pressure and wing surface area. $\bar{c}$ and b indicate the mean aerodynamic chord and wingspan. C_D, C_L, C_Y, C_l, C_m, C_n indicate the drag, lift, side force, rolling moment, pitching moment and yawing moment coefficients, respectively. The aerodynamic coefficients are calculated as [21]

$$\begin{aligned} C_D &= C_{D0} + C_{D\alpha}\alpha + C_{Dq}\frac{\bar{c}q}{2V} + C_{D\delta e}\delta_e \\ C_L &= C_{L0} + C_{L\alpha}\alpha + C_{Lq}\frac{\bar{c}q}{2V} + C_{L\delta e}\delta_e \\ C_Y &= C_{Y0} + C_{Y\beta}\beta + C_{Yp}\frac{bp}{2V} + C_{Yr}\frac{br}{2V} + C_{Y\delta a}\delta_a + C_{Y\delta r}\delta_r \\ C_l &= C_{l0} + C_{l\beta}\beta + C_{lp}\frac{bp}{2V} + C_{lr}\frac{br}{2V} + C_{l\delta a}\delta_a + C_{l\delta r}\delta_r \\ C_m &= C_{m0} + C_{m\alpha}\alpha + C_{mq}\frac{\bar{c}q}{2V} + C_{m\delta e}\delta_e \\ C_n &= C_{n0} + C_{n\beta}\beta + C_{np}\frac{bp}{2V} + C_{nr}\frac{br}{2V} + C_{n\delta a}\delta_a + C_{n\delta r}\delta_r \end{aligned} \tag{3.20}$$

where C_{D0}, $C_{D\alpha}$, C_{Dq}, C_{L0}, $C_{L\alpha}$, C_{Lq}, C_{m0}, $C_{m\alpha}$, C_{mq} are called the longitudinal stability derivatives. C_{Y0}, $C_{Y\beta}$, C_{Yp}, C_{Yr}, C_{l0}, $C_{l\beta}$, C_{lp}, C_{lr}, C_{n0}, $C_{n\beta}$, C_{np}, C_{nr} are called the lateral-directional stability derivatives. $C_{D\delta e}$, $C_{L\delta e}$, $C_{m\delta e}$ are called the longitudinal control derivatives and, finally, $C_{Y\delta a}$ $C_{Y\delta r}$, $C_{l\delta a}$, $C_{l\delta r}$, $C_{n\delta a}$, $C_{n\delta r}$ are called the lateral-directional control derivatives. The stability and control derivatives

define the aerodynamic characteristics of an aircraft. Detailed information on this topic can be found in [21, 28, 16].

The aerodynamic characteristics of the aircraft are as important as the GNC system to the success of the carrier landing. As mentioned previously in Chapter 1, even a small altitude error can result in an unacceptable landing error when mapped on to the longitudinal axis because of the small elevation angle of the glide path. Thus, the commanded altitude or the flight-path angle must be followed precisely for a successful landing.

In a study by Sweger [19], where the performance and maneuverability criteria that ensure satisfactory carrier landing precision and consistency were investigated, it is stated that the most unstable configurations in the longitudinal axis were the most desirable ones for every figure of merit evaluated. However, the study does not indicate a limit on suitable stability characteristics for a carrier-based aircraft. The most important quantity governing the longitudinal stability of an aircraft is the pitch stiffness derivative, C_{m_α}. Negative C_{m_α} implies positive pitch stiffness whereas positive C_{m_α} implies negative pitch stiffness. The same study also shows the drag coefficient, C_D, has an insignificant effect on the landing performance.

The most prominent outcome of [19] is about the longitudinal maneuverability. The lift curve slope is regarded as the most dominant factor in all aspects of performance for the carrier landing task. The lift curve slope governs the sensitivity of the flight-path angle to a change in the angle of attack and is denoted by C_{L_α}. A minimum value of 2.9 for C_{L_α} is suggested in the study. Although not mentioned in [19], elevator control power $C_{m_{\delta_e}}$ could also be a significant factor because it also improves the longitudinal maneuverability. Note that only longitudinal aerodynamic characteristics are discussed, although all six degrees of freedom are considered since the longitudinal tracking is the determining factor for a satisfactory landing dispersion.

To conclude, a suitable aircraft for carrier landing task must have high $C_{L\alpha}$, positive $C_{m\alpha}$ and a high negative $C_{m\delta_e}$. High negative $C_{m\delta_e}$ stems from the sign convention of the control surfaces deflections and choice of aircraft body axes coordinate system. An elevator-up input is negative and causes a positive (nose-up) moment about the y-axis of the body frame. The sign convention for the control surfaces are given in Table 3.3.

Table 3.3. Sign convention for control surfaces

Control Surface	**Positive Deflection**	**Negative Deflection**
Elevator	Trailing edge down	Trailing edge up
Aileron	Trailing edge up(right wing)	Trailing edge down(right wing)
Rudder	Trailing edge left	Trailing edge right

The aircraft models provided in [21] are considered as candidates for this research. Unfortunately, none of them satisfied all of the aerodynamic requirements discussed above. However, the SIAI Marchetti S211 aircraft is found to be the most suitable amongst all because of its excellent longitudinal maneuverability characteristics; thus, implemented in this study.

The aerodynamic stability and control derivatives are functions of the aircraft states and flight conditions. Conventionally, they are calculated by interpolation from high dimensional look-up tables, which account for the complete flight envelope of the aircraft. In this research, a linear aerodynamic model is implemented due to data availability on trusted and accessible sources such as [21, 28]. The model assumes the aerodynamic derivatives are constant, and they are calculated at a single point within the flight envelope. Strict control authority over the aircraft states during the landing operation confines the flight to a tiny region within the envelope, supporting

the linear aerodynamics assumption. The data for the aerodynamic model of the SIAI Marchetti S211 is presented in Table 3.4.

Table 3.4. Data for SIAI Marchetti S211 [21]

Classification	**Data Type**	**Value**
Flight Conditions	Altitude, h	0 ft
	Mach Number, M	0.111
	True Airspeed, V_P	124 ft/s
	Dynamic Pressure, $\bar{q}$	18.2 lbs/ft^2
	Angle of Attack, α	8 deg
Geometry	Wing Surface, S	136 ft^2
	Mean Aerodynamic Chord, $\bar{c}$	5.4 ft
	Wing Span, b	26.3 ft
Mass and Inertia	Mass, m	3500 lbs
	Moment of Inertia, x-axis, I_x	750 $slug \cdot ft^2$
	Moment of Inertia, y-axis, I_y	4600 $slug \cdot ft^2$
	Moment of Inertia, z-axis, I_z	5000 $slug \cdot ft^2$
	Product of inertia, xz-plane, I_{xz}	200 $slug \cdot ft^2$
Longitudinal Stability and Control Derivatives	(C_{D0},$C_{D\alpha}$,C_{Dq})	(0.09,1.14,0)
	(C_{L0},$C_{L\alpha}$,C_{Lq})	(0.65,5.0,9.0)
	(C_{m0},$C_{m\alpha}$,C_{mq})	(-0.07,-0.60,-15.7)
	($C_{D\delta e}$,$C_{L\delta e}$,$C_{m\delta e}$)	(0,0.39,-0.90)
Lateral-Directional Stability and Control Derivatives	(C_{Y0},$C_{Y\beta}$,C_{Yp},C_{Yr})	(0,-0.94,-0.01,0.59)
	(C_{l0},$C_{l\beta}$,C_{lp},C_{lr})	(0,-0.14,-0.35,0.56)
	(C_{n0},$C_{n\beta}$,C_{np},C_{nr})	(0,0.16,-0.03,-0.31)
	($C_{Y\delta a}$,$C_{l\delta a}$,$C_{n\delta a}$)	(0,0.11,-0.03)
	($C_{Y\delta r}$,$C_{l\delta r}$,$C_{n\delta r}$)	(0.26,0.03,-0.11)

3.2.3 Actuator and Engine Models

The control surface deflection and throttle inputs to the aircraft come from a state-space model that accounts for the actuator and engine dynamics. The inputs to this state space model are the commanded input signals that are generated by the controller. A first-order model in which the lag between the commanded signals

and actual deflections are defined by time constants is implemented. Also, saturation functions are used as rate and position limiters. The structure of the actuator and engine models is given in Figure 3.4 where $\boldsymbol{\delta} = [\delta_t \ \delta_e \ \delta_a \ \delta_r]^T$ and $\boldsymbol{\delta}_c = [\delta_{tc} \ \delta_{ec} \ \delta_{ac} \ \delta_{rc}]^T$ represent the actual and commanded input signals, respectively. The subscripts t, e, a and r indicate that the signal corresponds to the throttle, elevator, aileron and rudder inputs, respectively.

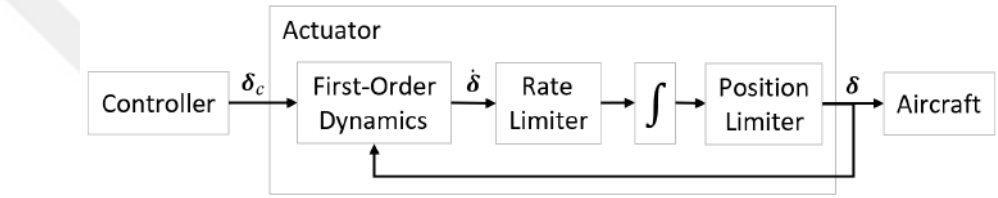

Figure 3.4. Structure of the actuators and engine model.

The mathematical model for the first-order dynamics is given as

$$\dot{\delta}_i = -\frac{1}{\tau_i}\,\delta_i + \frac{1}{\tau_i}\,\delta_{ic} \tag{3.21}$$

where i is to be replaced by t, e, a, or r, and τ_i represents the corresponding time constant.

An F-16 aircraft model acquired from [29] provides the quantities that define the control surface actuators, and the engine is modeled with one second of lag in response to a commanded signal. The actuator and engine model data are given in Table 3.5.

The actuator and engine models are later appended with the aircraft dynamics resulting in new plant dynamics where the actual surface deflection and throttle inputs are considered as additional states. The new control inputs of the appended system become the commanded input signals generated by the controller.

Table 3.5. Actuator and engine Model specifications

	Rate Limit	**Position Limit**	**Time Constant**
Throttle	$1/s$	$[0, 1]$	$1\ s$ lag
Elevator	$60\ deg/s$	$[-25\ deg, 25\ deg]$	$0.0495\ s$ lag
Aileron	$80\ deg/s$	$[-21.5\ deg, 21.5\ deg]$	$0.0495\ s$ lag
Rudder	$120\ deg/s$	$[-30\ deg, 30\ deg]$	$0.0495\ s$ lag

CHAPTER 4

REFERENCE TRAJECTORY AND GUIDANCE

4.1 Landing Kinematics

The derivation of relative kinematics between the aircraft and the carrier plays a crucial role in flight-path planning and guidance. The methods from [2] are adopted and applied in this section.

The distance, elevation angle and azimuth angle from the desired touchdown point to the aircraft are represented by d, λ and η, respectively. These variables are depicted in Figure 4.1. The relative position vector from the D-frame to A-frame can be expressed as

$$\boldsymbol{r}_{DA}^{I} = \boldsymbol{f}(\boldsymbol{x}_1) = \begin{bmatrix} d\cos\lambda\cos\eta \\ d\cos\lambda\sin\eta \\ -d\sin\lambda \end{bmatrix} \tag{4.1}$$

where $\boldsymbol{x}_1 = \begin{bmatrix} d & \lambda & \eta \end{bmatrix}^T$. Note that elevation and azimuth angles are, by definition, measured from the horizon and the North. Hence, the expression of the vector is in the inertial frame. The derivative of Equation 4.1 gives the relative velocity as

$$\dot{\boldsymbol{r}}_{DA}^{I} = \frac{\partial \boldsymbol{r}_{DA}^{I}}{\partial d}\,\dot{d} + \frac{\partial \boldsymbol{r}_{DA}^{I}}{\partial \lambda}\,\dot{\lambda} + \frac{\partial \boldsymbol{r}_{DA}^{I}}{\partial \eta}\,\dot{\eta} \tag{4.2}$$

The relative velocity of the aircraft with respect to the desired touchdown point can also be expressed by a simple vector operation:

$$\dot{\boldsymbol{r}}_{DA}^{I} = \dot{\boldsymbol{r}}_{IA}^{I} - \dot{\boldsymbol{r}}_{ID}^{I} \tag{4.3}$$

Combining Equations 4.2 and 4.3 gives

$$\frac{\partial \boldsymbol{r}_{DA}^{I}}{\partial d}\,\dot{d} + \frac{\partial \boldsymbol{r}_{DA}^{I}}{\partial \lambda}\,\dot{\lambda} + \frac{\partial \boldsymbol{r}_{DA}^{I}}{\partial \eta}\,\dot{\eta} = \dot{\boldsymbol{r}}_{IA}^{I} - \dot{\boldsymbol{r}}_{ID}^{I} \tag{4.4}$$

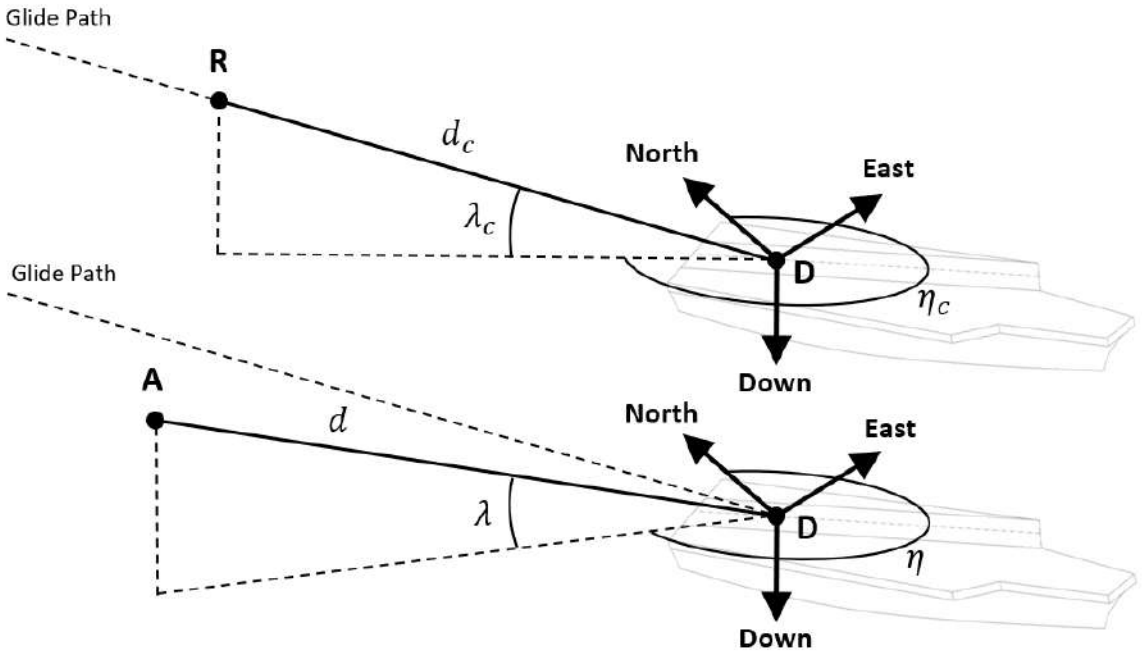

Figure 4.1. Representation of $\boldsymbol{x}_1 = [d \quad \lambda \quad \eta]^T$ and $\boldsymbol{x}_{1c} = [d_c \quad \lambda_c \quad \eta_c]^T$.

Equation 4.4 can be rearranged to provide an equation for the landing kinematics in terms of $\boldsymbol{x}_1$:

$$\begin{aligned} \boldsymbol{M}\dot{\boldsymbol{x}}_1 &= \dot{\boldsymbol{r}}^I_{IA} - \dot{\boldsymbol{r}}^I_{ID} \\ \dot{\boldsymbol{x}}_1 &= \boldsymbol{M}^{-1}(\dot{\boldsymbol{r}}^I_{IA} - \dot{\boldsymbol{r}}^I_{ID}) \end{aligned} \tag{4.5}$$

where $\boldsymbol{M} = \left[\frac{\partial \boldsymbol{r}^I_{DA}}{\partial d} \quad \frac{\partial \boldsymbol{r}^I_{DA}}{\partial \lambda} \quad \frac{\partial \boldsymbol{r}^I_{DA}}{\partial \eta}\right]$ is the Jacobian matrix of $\boldsymbol{r}^I_{DA}$ and $\dot{\boldsymbol{x}}_1 = \left[\dot{d} \quad \dot{\lambda} \quad \dot{\eta}\right]^T$. The elements of the Jacobian matrix are found by partial differentiation of Equation 4.1 as

$$\begin{aligned} \frac{\partial \boldsymbol{r}^I_{DA}}{\partial d} &= \left[\cos\lambda\cos\eta \quad \cos\lambda\sin\eta \quad -\sin\lambda\right]^T \\ \frac{\partial \boldsymbol{r}^I_{DA}}{\partial \lambda} &= \left[-d\sin\lambda\cos\eta \quad -d\sin\lambda\sin\eta \quad -d\cos\lambda\right]^T \\ \frac{\partial \boldsymbol{r}^I_{DA}}{\partial \eta} &= \left[-d\cos\lambda\sin\eta \quad d\cos\lambda\cos\eta \quad 0\right]^T \end{aligned} \tag{4.6}$$

4.2 Reference Trajectory Generation

In trajectory planning, a reference point that represents the desired location of the aircraft in space must be chosen. Also, a reference trajectory must be formulated so that the reference point is assigned the desired dynamics. Thus, the reference trajectory defines not only the desired path but also the velocity and acceleration profile along this path. The method by which the reference trajectory is generated is adopted from [2] and explained in this section.

The inertial location of the reference point can be expressed as

$$\boldsymbol{r}^I_{IR} = \boldsymbol{r}^I_{ID} + \boldsymbol{r}^I_{DR} \tag{4.7}$$

where subscript R indicates the reference point. The derivative of Equation 4.7 gives the dynamics of the reference point as

$$\dot{\boldsymbol{r}}^I_{IR} = \dot{\boldsymbol{r}}^I_{ID} + \dot{\boldsymbol{r}}^I_{DR} \tag{4.8}$$

The glide path is an imaginary line in space that extends aft from the desired touchdown point and is defined by the elevation angle, λ_c and azimuth angle, η_c. Remember, elevation and azimuth angles are, by definition, measured from the horizon and the North, respectively. Figure 4.1 depicts the glide path and the reference point. The reference point must move towards the touchdown point along the glide path. Similar to Equation 4.1, the location of the reference point with respect to the touchdown point at any given time can be expressed as

$$\boldsymbol{r}^I_{DR} = \boldsymbol{f}(\boldsymbol{x}_{1c}) = \begin{bmatrix} d_c \cos\lambda_c \cos\eta_c \\ d_c \cos\lambda_c \sin\eta_c \\ -d_c \sin\lambda_c \end{bmatrix} \tag{4.9}$$

where $\boldsymbol{x}_{1c} = \begin{bmatrix} d_c & \lambda_c & \eta_c \end{bmatrix}^T$. Following the same procedure which is explained in Section 4.1, the kinematics of the reference point is found as

$$\dot{\boldsymbol{r}}^I_{IR} = \dot{\boldsymbol{r}}^I_{ID} + \frac{\partial \boldsymbol{r}^I_{DR}}{\partial d_c}\ \dot{d}_c + \frac{\partial \boldsymbol{r}^I_{DR}}{\partial \lambda_c}\ \dot{\lambda}_c + \frac{\partial \boldsymbol{r}^I_{DR}}{\partial \eta_c}\ \dot{\eta}_c \tag{4.10}$$

where the partial derivatives are given as

$$\begin{aligned}
\frac{\partial \boldsymbol{r}^I_{DR}}{\partial d_c} &= \begin{bmatrix} \cos\lambda_c \cos\eta_c & \cos\lambda_c \sin\eta_c & -\sin\lambda_c \end{bmatrix}^T \\
\frac{\partial \boldsymbol{r}^I_{DR}}{\partial \lambda_c} &= \begin{bmatrix} -d_c \sin\lambda_c \cos\eta_c & -d_c \sin\lambda_c \sin\eta_c & -d_c \cos\lambda_c \end{bmatrix}^T \\
\frac{\partial \boldsymbol{r}^I_{DR}}{\partial \eta_c} &= \begin{bmatrix} -d_c \cos\lambda_c \sin\eta_c & d_c \cos\lambda_c \cos\eta_c & 0 \end{bmatrix}^T
\end{aligned} \tag{4.11}$$

Note that the kinematics of the reference point can be assigned by the appropriate selection of $\dot{\boldsymbol{x}}_{1c} = \begin{bmatrix} \dot{d}_c & \dot{\lambda}_c & \dot{\eta}_c \end{bmatrix}^T$. It is desired to have a glide path with constant elevation angle. The azimuth angle can be calculated such that the glide path is always aligned with the longitudinal axis of the D-frame, i.e, $\eta_c = \pi + \psi_D$. However, η_c is also assumed to be constant because of the very small magnitude of yaw oscillation of the deck. Substitution of $\dot{\lambda}_c = 0$ and $\dot{\eta}_c = 0$ simplifies Equation 4.10 to

$$\dot{\boldsymbol{r}}^I_{IR} = \dot{\boldsymbol{r}}^I_{ID} + \frac{\partial \boldsymbol{r}^I_{DR}}{\partial d_c}\ \dot{d}_c \tag{4.12}$$

Taking the norm of Equation 4.12 to solve for $\dot{d}_c$ gives

$$\begin{aligned}
\left\|\dot{\boldsymbol{r}}^I_{IR}\right\|^2 &= \left((\dot{\boldsymbol{r}}^I_{ID})^T + \dot{d}_c \left(\frac{\partial \boldsymbol{r}^I_{DR}}{\partial d_c} \right)^T \right) \left(\dot{\boldsymbol{r}}^I_{ID} + \frac{\partial \boldsymbol{r}^I_{DR}}{\partial d_c}\ \dot{d}_c \right) \\
&= \left\|\dot{\boldsymbol{r}}^I_{ID})\right\|^2 + \dot{d}_c\ (\dot{\boldsymbol{r}}^I_{ID})^T\ \frac{\partial \boldsymbol{r}^I_{DR}}{\partial d_c} + \dot{d}_c\ \left(\frac{\partial \boldsymbol{r}^I_{DR}}{\partial d_c} \right)^T\ \dot{\boldsymbol{r}}^I_{ID} \\
&\quad + {\dot{d}_c}^2\ \left(\frac{\partial \boldsymbol{r}^I_{DR}}{\partial d_c} \right)^T\ \frac{\partial \boldsymbol{r}^I_{DR}}{\partial d_c}
\end{aligned} \tag{4.13}$$

Note that $a = (\dot{\boldsymbol{r}}^I_{ID})^T\ \frac{\partial \boldsymbol{r}^I_{DR}}{\partial d_c}$ is a scalar. Hence, we have $a^T = \left(\frac{\partial \boldsymbol{r}^I_{DR}}{\partial d_c} \right)^T \dot{\boldsymbol{r}}^I_{ID} = a$ and $\left(\frac{\partial \boldsymbol{r}^I_{DR}}{\partial d_c} \right)^T\ \frac{\partial \boldsymbol{r}^I_{DR}}{\partial d_c} = 1$. With these properties, Equation 4.13 simplifies to

$${\dot{d}_c}^2 + 2\ \dot{d}_c \left(\frac{\partial \boldsymbol{r}^I_{DR}}{\partial d_c} \right)^T\ \dot{\boldsymbol{r}}^I_{ID} + \left\|\dot{\boldsymbol{r}}^I_{ID})\right\|^2 - \left\|\dot{\boldsymbol{r}}^I_{IR}\right\|^2 = 0 \tag{4.14}$$

Solving Equation 4.14 for $\dot{d}_c$ gives

$$\dot{d}_c = -\left(\frac{\partial \boldsymbol{r}^I_{DR}}{\partial d_c}\right)^T \dot{\boldsymbol{r}}^I_{ID} - \sqrt{\left(\left(\frac{\partial \boldsymbol{r}^I_{DR}}{\partial d_c}\right)^T \dot{\boldsymbol{r}}^I_{ID}\right)^2 - \|\dot{\boldsymbol{r}}^I_{ID})\|^2 + \|\dot{\boldsymbol{r}}^I_{IR}\|^2} \tag{4.15}$$

Note that Equation 4.14 is a second-order equation; thus, has two solutions for $\dot{d}_c$. The positive solution is ignored because the aircraft must move towards the touchdown point. Also, the reference point is assumed to have a constant speed, which is given by the trim velocity, V_0, for which the controller is designed, and aerodynamic coefficients are calculated, i.e., $\|\dot{\boldsymbol{r}}^I_{IR}\| = V_0$.

4.3 Guidance Laws

The landing kinematics and reference trajectory generation are described previously. The guidance provides the means to relate the aircraft states to the reference trajectory by using landing kinematics. The objective of the guidance is to generate a flight-path command, $\boldsymbol{x}_{2c} = \begin{bmatrix} V_c & \chi_c & \gamma_c \end{bmatrix}^T$, to achieve the reference trajectory.

The carrier landing task is investigated in two phases. The first phase is called the approach phase, and the second phase is called the touchdown phase. Two guidance laws are employed in this study to satisfy the unique and somehow contrasting requirements of these two phases. Two guidance laws have mutual objectives, yet they are different in their strengths and weaknesses. The distinction is in the error signals that drive each guidance signal.

The first guidance law employs the difference between the actual and commanded signals of the vector $\boldsymbol{x}_1$ as the error signal. This guidance strategy works well in the approach phase of the carrier landing task. As the aircraft gets closer to the desired touchdown point, the guidance law becomes more sensitive to position errors because the same positional error causes a greater angular error in short-range in

comparison to the long-range. This behavior is depicted in the vertical plane in Figure 4.2. In this figure, the positions of the aircraft, the reference point, and the desired touchdown point are shown by A, R, and D, respectively. The altitude and elevation errors are shown by e_h and e_λ. The subscripts 1 and 2 correspond to the time instants in the long-range and the short-range, respectively. Note that for $e_{h1} = e_{h2}$, we have $e_{\lambda 1} < e_{\lambda 2}$. This feature of the guidance law is, in fact, desirable because nonresponsiveness of the guidance law to the positional error in long-range saves control power when precision tracking is not essential. Also, position and attitude estimation errors of the carrier deck diminish with the closing range, which is discussed in Chapter 6. Hence, it is beneficial to introduce a guidance law that is insensitive to the estimation errors in the long-range.

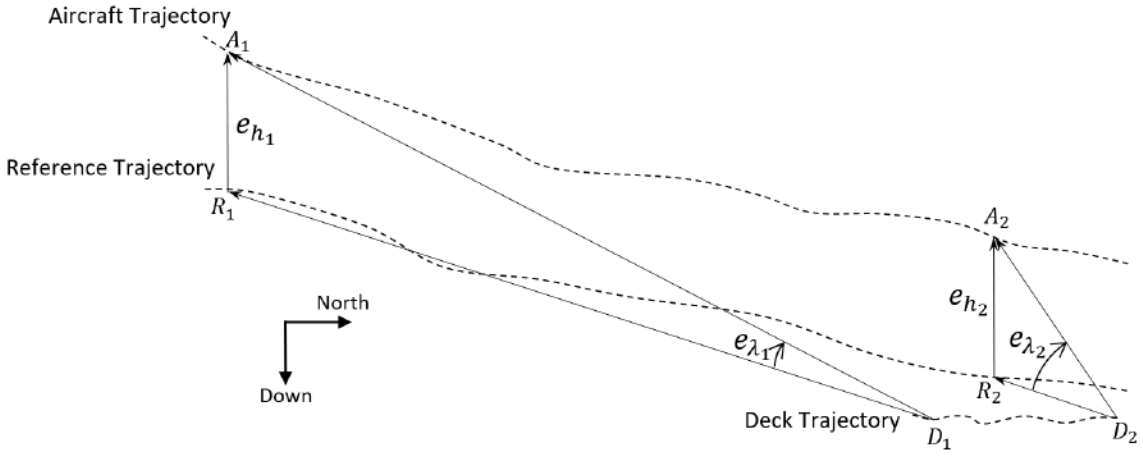

Figure 4.2. Range dependent sensitivity of angle-based guidance law.

There is also a downside of the first guidance strategy; that is, even the smallest position errors give rise to extreme errors in elevation and azimuth angles right before touchdown occurs, causing abrupt control inputs and changes in the attitude of the aircraft. Simulations show these abrupt changes pose a severe threat because it may

lead to dangerous situations such as the aircraft hitting its nose or wings on the deck surface.

A second guidance law is proposed to be employed during the touchdown phase to avoid the dangerous nature of the first guidance strategy without compromising precision. In this guidance law, the flight-path command is driven by a positional error vector, $\boldsymbol{r}_{RA}^{I}$. This guidance law does not possess the positive features of the first guidance law in long-range; however, supersedes it in terms of reliability and consistency in the touchdown phase.

4.3.1 Angle-Based Guidance

The first guidance law is formulated in this section. It is referred to as angle-based guidance law because the flight-path command is driven by angular quantities. The error signal is given as

$$\boldsymbol{e}_1 = \boldsymbol{x}_1 - \boldsymbol{x}_{1c} \tag{4.16}$$

The error dynamics is found by differentiating Equation 4.16 and substituting Equation 4.5 as

$$\begin{aligned} \dot{\boldsymbol{e}}_1 =& \dot{\boldsymbol{x}}_1 - \dot{\boldsymbol{x}}_{1c} \\ =& \boldsymbol{M}^{-1}(\dot{\boldsymbol{r}}_{IA}^{I} - \dot{\boldsymbol{r}}_{ID}^{I}) - \dot{\boldsymbol{x}}_{1c} \\ =& \boldsymbol{f_1} + \boldsymbol{g_1}\boldsymbol{v} - \dot{\boldsymbol{x}}_{1c} \end{aligned} \tag{4.17}$$

where $\boldsymbol{f_1} = -\boldsymbol{M}^{-1}\dot{\boldsymbol{r}}_{ID}^{I}$, $\boldsymbol{g_1} = \boldsymbol{M}^{-1}$ and $\boldsymbol{v} = \dot{\boldsymbol{r}}_{IA}^{I}$ is a virtual guidance input [2]. Remember, $\dot{\boldsymbol{x}}_{1c} = \begin{bmatrix} \dot{d}_c & \dot{\lambda}_c & \dot{\eta_c} \end{bmatrix}^T$ where $\dot{d}_c$ is given by Equation 4.15, $\dot{\lambda}_c = 0$ and $\dot{\eta}_c = 0$.

In order to find a virtual guidance input that results in stable error dynamics, we employ dynamic inversion technique. Firstly, the desired dynamics of the error, $\boldsymbol{e}_1$, are proposed as

$$\dot{\boldsymbol{e}}_1 = -\boldsymbol{K}_{ab}\, \boldsymbol{e}_1 \tag{4.18}$$

where $\boldsymbol{K}_{ab}$ is a diagonal, three by three, positive definite matrix. Positive definiteness of $\boldsymbol{K}_{ab}$ ensures stable error dynamics. Substitution of desired error dynamics into Equation 4.17 and application of dynamic inversion to solve for virtual guidance input, $\boldsymbol{v}$, gives

$$\boldsymbol{v} = \boldsymbol{M}\left(-\boldsymbol{f_1} + \dot{\boldsymbol{x}}_{1c} - \boldsymbol{K}_{ab}\, \boldsymbol{e}_1\right) \tag{4.19}$$

The inertial velocity of the aircraft can be calculated as

$$\dot{\boldsymbol{r}}_{IA}^{I} = \boldsymbol{f}(\boldsymbol{x}_2) = V \begin{bmatrix} \cos\gamma\cos\chi \\ \cos\gamma\sin\chi \\ -\sin\gamma \end{bmatrix} \tag{4.20}$$

One-to-one correspondence between the inertial velocity of the aircraft, $\dot{\boldsymbol{r}}_{IA}^{I}$, and $\boldsymbol{x}_2$, is exploited to calculate the guidance signal, $\boldsymbol{x}_{2c} = \begin{bmatrix} V_c & \chi_c & \gamma_c \end{bmatrix}^T$ for a given $\boldsymbol{v} = \begin{bmatrix} v_1 & v_2 & v_3 \end{bmatrix}^T$ as

$$\begin{aligned} V_c &= \|\boldsymbol{v}\| \\ \chi_c &= \tan^{-1}\frac{v_2}{v_1} \\ \gamma_c &= -\sin^{-1}\frac{v_3}{V_c} \end{aligned} \tag{4.21}$$

4.3.2 Position-Based Guidance

The second guidance law is formulated in this section. It is referred to as position-based guidance law because the flight-path command is driven by positional quantities. The error signal that drives this guidance law is given as

$$\boldsymbol{e}_5 = \boldsymbol{x}_5 - \boldsymbol{x}_{5c} \tag{4.22}$$

where $\boldsymbol{x}_5 = \boldsymbol{r}^I_{DA}$ and $\boldsymbol{x}_{5c} = \boldsymbol{r}^I_{DR}$. Note that both $\boldsymbol{x}_1$ and $\boldsymbol{x}_5$ are vector representations for the relative location of the aircraft with respect to the desired touchdown point but they are composed of different quantities. The error dynamics are found by differentiating Equation 4.22 as

$$\dot{\boldsymbol{e}}_5 = \dot{\boldsymbol{x}}_5 - \dot{\boldsymbol{x}}_{5c} \tag{4.23}$$

where $\dot{\boldsymbol{x}}_5 = \dot{\boldsymbol{r}}^I_{IA} - \dot{\boldsymbol{r}}^I_{ID}$ and $\dot{\boldsymbol{x}}_{5c} = \dot{\boldsymbol{r}}^I_{DR} = \frac{\partial \boldsymbol{r}^I_{DR}}{\partial \boldsymbol{x}_{1c}}\, \dot{\boldsymbol{x}}_{1c}$. Similar to the previous section, we want to assign stable dynamics to the error signal such that

$$\dot{\boldsymbol{e}}_5 = -\boldsymbol{K}_{pb}\, \boldsymbol{e}_5 \tag{4.24}$$

where $\boldsymbol{K}_{pb}$ is a diagonal, three by three, positive definite matrix. The same procedure as the previous section is followed to calculate the virtual guidance input as

$$\boldsymbol{v} = -\boldsymbol{K}_{pb}\, \boldsymbol{e}_5 + \dot{\boldsymbol{x}}_{5c} + \dot{\boldsymbol{r}}^I_{ID} \tag{4.25}$$

Equation 4.21 is used to calculate the flight-path command from virtual guidance input.

4.3.3 Guidance Strategy

Angle-based and position-based guidance laws are introduced in Section 4.3. This section explains how these guidance laws are utilized during the carrier landing task and how the switch from angle-based to position-based is performed.

The most straightforward approach is to switch from the angle-based scheme to the position-based scheme at a prespecified distance from the touchdown point. A sudden switch causes a piecewise, discontinuous flight-path command signal. Simulation shows the system often cannot adapt to this jump in the guidance command and go unstable. This problem can be minimized by specifying a distance such that

the guidance laws produce a similar flight-path command but is not fully avoided. A smoother transition can be achieved by specifying two distances between which flight-path commands from the two guidance laws are interpolated and fed to the controller. Let these two distances be denoted by d_4 and d_5. Then, the guidance strategy is given by a linear interpolation as

$$\boldsymbol{x}_{2_c} = \begin{cases} \boldsymbol{x}_{2_c}^{ab}, & \hat{d} \geq d_4 \\ \boldsymbol{x}_{2_c}^{ab} - \frac{d_4 - \hat{d}}{d4 - d5}(\boldsymbol{x}_{2_c}^{ab} - \boldsymbol{x}_{2_c}^{pb}), & d_4 > \hat{d} > d_5 \\ \boldsymbol{x}_{2_c}^{pb}, & d_5 \geq \hat{d} \end{cases} \tag{4.26}$$

where $\boldsymbol{x}_{2_c}^{ab}$ and $\boldsymbol{x}_{2_c}^{pb}$ correspond to flight-path command signals generated by angle-based and position-based guidance laws; respectively, and $\hat{d}$ denotes estimated distance from the aircraft to the desired touchdown point. The guidance laws yield similar flight-path commands for $500\,m > d > 50\,m$; hence, we choose $d_4 = 500\,m$ and $d_5 = 50\,m$.

The elements of the gain matrices, $\boldsymbol{K}_{ab}$ and $\boldsymbol{K}_{pb}$ are assigned using time constants since the error dynamics are in first-order. The time constants regarding the error dynamics of d, λ, η, $(\boldsymbol{r}_{DA}^I)_x$, $(\boldsymbol{r}_{DA}^I)_y$, $(\boldsymbol{r}_{DA}^I)_z$ are chosen as $10s$, $10s$, $1000s$, $10s$, $20s$, $0.5s$; respectively, which yields the following gain matrices:

$$\boldsymbol{K}_{ab} = \begin{bmatrix} 0.1 & 0 & 0 \\ 0 & 0.1 & 0 \\ 0 & 0 & 0.001 \end{bmatrix}, \quad \boldsymbol{K}_{pb} = \begin{bmatrix} 0.1 & 0 & 0 \\ 0 & 0.05 & 0 \\ 0 & 0 & 2 \end{bmatrix} \tag{4.27}$$

Note that the guidance in the lateral axis is relaxed by assigning relatively greater time constants to error dynamics of η and $(\boldsymbol{r}_{DA}^I)_y$ since the lateral requirements of the carrier landing task are easier to satisfy.

CHAPTER 5

CONTROL SYSTEM

5.1 Linear Model

A nonlinear mathematical model that represents the aircraft dynamics in six degrees of freedom is explained in Section 3.2. In this study, a control system is implemented in this nonlinear mathematical model; however, it is designed based on a linear approximation. A nonlinear model describes the global behavior of a system; yet, the local behavior of the same system at an operating point can be approximated by its linearization.

Assume a nonlinear dynamic system is given as

$$\dot{x} = f(x) \tag{5.1}$$

and the output of function f at an operating point x_0 is $f(x_0)$. Using Taylor series expansion, function f can be expressed as [30]

$$\begin{aligned} f(x) =& \sum_{n=0}^{\infty} \left.\frac{d^{(n)}f}{dx^{(n)}}\right|_{x_0} \frac{(x-x_0)^n}{n!} \\ =& f(x_0) + \left.\frac{df}{dx}\right|_{x_0} (x-x_0) + H.O.T. \end{aligned} \tag{5.2}$$

where H.O.T. stands for higher order terms and is given as

$$H.O.T. = \left.\frac{d^2f}{dx^2}\right|_{x_0} \frac{(x-x_0)^2}{2!} + \left.\frac{d^3f}{dx^3}\right|_{x_0} \frac{(x-x_0)^3}{3!} + ... \tag{5.3}$$

Let us define the distance from the operating point as $\Delta x = x - x_0$. Note that a sufficiently small displacement of x from the operating point implies $\Delta x << 1$. Also, $\Delta x^n << ... << \Delta x^2 << \Delta x << 1$. Hence, higher order terms become negligible for

a small perturbance of x from the operating point and the nonlinear function, f, can be approximated by its first-order Taylor series expansion as

$$f(x) \approx f(x_0) + \left.\frac{df}{dx}\right|_{x_0} (x - x_0) \tag{5.4}$$

Let us now define the change in output as $\Delta f(x) = f(x) - f(x_0)$. Equation 5.4 can be rearranged to find an expression for $\Delta f(x)$ as

$$\Delta f(x) \approx \left.\frac{df}{dx}\right|_{x_0} \Delta x \tag{5.5}$$

Note that Equation 5.5 is linear because $\left.\frac{df}{dx}\right|_{x_0}$ is a constant. A simple graphical illustration of the small perturbance and linearization theory given in Figure 5.1. In this figure, a nonlinear system whose input-output relationship is given by the black curve is linearized at point A. The linearized system is given by the blue line whose slope is $\left.\frac{df}{dx}\right|_{x_0}$ and it is evaluated in a new coordinate system having its origin at point A and a new set of axes, δx and $\delta f(x)$.

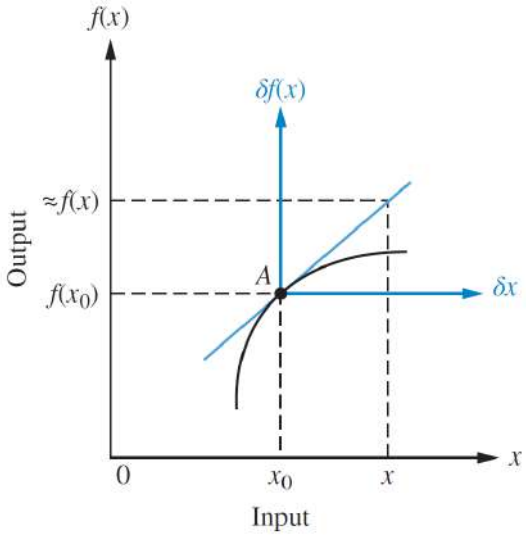

Figure 5.1. Linearization about point A [31].

5.1.1 Steady-State Flight and Equilibrium

An introduction to the small perturbance and linearization theory is given previously. It is mentioned that the local behavior of a nonlinear system around an operating point can be approximated by a linear system. Hence, an operating point must be chosen prior to the linearization.

The concept of steady-state aircraft flight is the key to the selection of a proper operating point about which we want to perform a linearization. The definition and properties of the steady-state flight are taken from [16]. For a given dynamical system,

$$\dot{\boldsymbol{x}} = \boldsymbol{f}(\boldsymbol{x}, \boldsymbol{\delta}) \tag{5.6}$$

where $\boldsymbol{f}$ is an array of n scalar nonlinear functions, $\boldsymbol{x}$ is a state vector and $\boldsymbol{\delta}$ is an input vector, the coordinates of a steady-state or equilibrium point are given by the solution, $\boldsymbol{x} = \boldsymbol{x}_0$, which satisfies

$$\dot{\boldsymbol{x}} = \boldsymbol{f}(\boldsymbol{x}, \boldsymbol{\delta}) = 0, \; with \;\; \boldsymbol{\delta} = \boldsymbol{\delta}_0 = constant \tag{5.7}$$

The most general case of steady-state flight implies all of the force and moment components in the body-fixed coordinate system must be zero. All the force components being zero requires velocity and aerodynamics angles; all the moment components being zero requires angular rates to be constant.

In this study, wings-level descent is chosen as the steady-state flight condition. Wings-level descent is permitted as a steady-state flight condition if the change in atmospheric density with altitude is neglected. In this case, inertial position equations do not couple back into the equations of motion and need not be used in finding a steady-state condition [16]. The landing operation is performed in a small range of altitudes; therefore, atmospheric density can be assumed as constant.

In wings-level descent, roll angle, roll rate, pitch rate, and yaw rate must also be zero in addition to constraints of the most general case of steady-state flight. Euler rates being zero implies angular rates are not only constant but also zero.

Applying all the constraints of wings-level descent to the aircraft dynamics gives

$$\begin{aligned} States: &\quad \dot{V}, \dot{\chi}, \dot{\gamma}, \dot{\phi}, \dot{\alpha}, \dot{\beta}, p, q, r \equiv 0 \\ Controls: &\quad \dot{\delta}_t, \dot{\delta}_e, \dot{\delta}_a, \dot{\delta}_r \equiv 0 \end{aligned} \tag{5.8}$$

The linearization approximation holds only for small perturbances. Thus, an equilibrium point which satisfies the conditions of wings-level descent must be selected carefully. Also, the performance of a linear control system is guaranteed only at the operating point for which it is designed. All the perturbations must be tolerated by the stability margins.

The nonlinear equations that describe the aircraft dynamics are highly coupled. Therefore, finding an equilibrium point requires the simultaneous solution of Equations 3.15-3.17. An exact solution by analytic methods is often impossible due to the complexity and nonlinearity of these equations. Instead, numerical methods are employed to find approximate solutions. In this study, the trim function of MATLAB's linear analysis toolbox is utilized to find an equilibrium point. This function starts at an initial point provided by the user and searches an equilibrium point using a sequential quadratic programming algorithm. More detailed information about the trim function can be found in [32].

The uniqueness of the solution to a set of simultaneous nonlinear equations is not guaranteed. In other words, there may be multiple equilibrium points for the nonlinear system subjected to constraints of wings-level descent. Additional constraints must be provided to find an appropriate equilibrium point amongst many. In this research, some aircraft states at the equilibrium point are provided as hard constraints to the trim algorithm. Fixed control inputs are subjected to maximum and minimum

deflection limits that are given in Table 3.5. Hence, the trim algorithm is forced to find fixed control inputs within the physical limits of actuators, which would keep the aircraft at the desired equilibrium. Several factors are taken into consideration when selecting the hard constraints on the aircraft states at the equilibrium point. These factors are

- flight conditions for which aerodynamics derivatives are calculated,
- maximum allowable structural loads on landing gear at touchdown,
- aerodynamic stall margin,
- and optimal hook engagement.

The factors listed above dictate opposing requirements for the steady-state values of the aircraft states. For example, the maximum allowable structural load determines the flight-path angle and velocity. A more negative flight-path angle and higher velocity would put more load on the landing gear; hence, they are undesirable. However, a less negative flight-path angle and low speed might cause an unacceptably small aerodynamic stall margin. For this reason, a trade-off must be performed to find the ideal values for the steady-state.

The flight conditions for which the aerodynamics derivatives are calculated are given in Table 3.4. They are essential for the sake of consistency between the aerodynamic model and the controller.

According to [19], the optimal value of the pitch angle of the aircraft relative to the runway is dictated by the hook engagement geometry and is given as $5\,deg$. Also, a flight-path angle of $-3\,deg$ is suggested for carrier landing tasks. A more negative flight-path angle could positively affect the longitudinal landing error because the mapping of the altitude error on the longitudinal plane would be smaller.

The aerodynamic stall margin is most closely related to the angle of attack. A high angle of attack allows a lower speed at equilibrium, but the aerodynamic stall

margin might suffer. A steady-state angle of attack of 9 deg allows a good compromise between the approach speed and aerodynamic stall margin. Also, a near-optimal pitch angle is achieved at steady-state because $\theta_0 = \alpha_0 + \gamma_0 = 6\,deg$.

Finally, the additional hard constraints that are provided to the optimization algorithm to narrow down the search of the equilibrium point are determined as

$$\gamma \equiv \gamma_0 = -0.05236\ rad, \quad \alpha \equiv \alpha_0 = 0.15708\ rad, \quad \beta \equiv \beta_0 = 0\ rad \tag{5.9}$$

The steady-state values of V, δ_t, δ_e, δ_a, δ_r are found by the algorithm as

$$\begin{gathered} V \equiv V_0 = 37.9523\ m/s, \quad \delta_t \equiv \delta_{t0} = 0.22114, \quad \delta_e \equiv \delta_{e0} = -0.18250\ rad, \\ \delta_a \equiv \delta_{a0} = 0\ rad, \quad \delta_r \equiv \delta_{r0} = 0\ rad \end{gathered} \tag{5.10}$$

Table 5.1 summarizes the equilibrium point and optimization constraints. Note that χ may have any constant value at the equilibrium; therefore, is not assigned any desired value.

Table 5.1. Results of the trim algorithm

		Value		**Time Derivative**	
		Desired	**Actual**	**Desired**	**Actual**
States	$V\ (m/s)$	$[20, 60]$	37.9523	0	-4.07×10^{-9}
	$\chi\ (rad)$	-	0	0	0
	$\gamma\ (rad)$	-0.05236	-0.05236	0	-2.12×10^{-9}
	$\phi\ (rad)$	0	0	0	0
	$\alpha\ (rad)$	0.15708	0.15708	0	2.12×10^{-9}
	$\beta\ (rad)$	0	0	0	0
	$p\ (rad/s)$	0	0	0	0
	$q\ (rad/s)$	0	0	0	1.12×10^{-7}
	$r\ (rad/s)$	0	0	0	0
Control Inputs	δ_t	$[0, 1]$	0.22114	0	0
	$\delta_e\ (rad)$	$[-0.44, 0.44]$	-0.18250	0	0
	$\delta_a\ (rad)$	$[-0.38, 0.38]$	0	0	0
	$\delta_r\ (rad)$	$[-0.52, 0.52]$	0	0	0

5.1.2 Linearization

A brief explanation of linearization is given for a first-order autonomous system in Section 5.1, and a graphical illustration is given in Figure 5.1. In this section, the same idea is extended to multi-order nonautonomous dynamical systems.

Consider the n^{th} order nonautomous system given in Equation 5.6 with a control input $\boldsymbol{\delta}$. The Taylor series approximation of this system is given as [33]

$$\boldsymbol{f}(\boldsymbol{x},\boldsymbol{\delta}) = \boldsymbol{f}(\boldsymbol{x}_0,\boldsymbol{\delta}_0) + \left.\frac{\partial \boldsymbol{f}}{\partial \boldsymbol{x}}\right|_{\boldsymbol{x}_0,\boldsymbol{\delta}_0} (\boldsymbol{x}-\boldsymbol{x}_0) + \left.\frac{\partial \boldsymbol{f}}{\partial \boldsymbol{\delta}}\right|_{\boldsymbol{x}_0,\boldsymbol{\delta}_0} (\boldsymbol{\delta}-\boldsymbol{\delta}_0) + H.O.T. \tag{5.11}$$

The linear approximation of the original system at the equilibrium point can be found by neglecting the higher-order terms in Equation 5.11 as

$$\Delta\dot{\boldsymbol{x}} = \boldsymbol{A}\Delta\boldsymbol{x} + \boldsymbol{B}\Delta\boldsymbol{\delta} \tag{5.12}$$

where $\Delta\dot{\boldsymbol{x}} = \boldsymbol{f}(\boldsymbol{x},\boldsymbol{\delta}) - \boldsymbol{f}(\boldsymbol{x}_0,\boldsymbol{\delta}_0)$, $\Delta\boldsymbol{x} = \boldsymbol{x}-\boldsymbol{x}_0$ and $\Delta\boldsymbol{\delta} = \boldsymbol{\delta}-\boldsymbol{\delta}_0$. $\boldsymbol{A}$ and $\boldsymbol{B}$ matrices denote the Jacobian matrix of $\boldsymbol{f}$ with respect to $\boldsymbol{x}$ and $\boldsymbol{\delta}$; respectively, and are given as

$$\begin{aligned}
\boldsymbol{A} = \left.\frac{\partial \boldsymbol{f}}{\partial \boldsymbol{x}}\right|_{\boldsymbol{x}_0,\boldsymbol{\delta}_0} &= \begin{bmatrix} \frac{\partial f_1}{\partial x_1} & \frac{\partial f_1}{\partial x_2} & \cdots & \frac{\partial f_1}{\partial x_n} \\ \frac{\partial f_2}{\partial x_1} & \frac{\partial f_2}{\partial x_2} & \cdots & \frac{\partial f_2}{\partial x_n} \\ \vdots & \vdots & \ddots & \vdots \\ \frac{\partial f_n}{\partial x_1} & \frac{\partial f_n}{\partial x_2} & \cdots & \frac{\partial f_n}{\partial x_n} \end{bmatrix}_{(\boldsymbol{x}_0,\boldsymbol{\delta}_0)} \\
\boldsymbol{B} = \left.\frac{\partial \boldsymbol{f}}{\partial \boldsymbol{\delta}}\right|_{\boldsymbol{x}_0,\boldsymbol{\delta}_0} &= \begin{bmatrix} \frac{\partial f_1}{\partial \delta_1} & \frac{\partial f_1}{\partial \delta_2} & \cdots & \frac{\partial f_1}{\partial \delta_k} \\ \frac{\partial f_2}{\partial \delta_1} & \frac{\partial f_2}{\partial \delta_2} & \cdots & \frac{\partial f_2}{\partial \delta_k} \\ \vdots & \vdots & \ddots & \vdots \\ \frac{\partial f_n}{\partial \delta_1} & \frac{\partial f_n}{\partial \delta_2} & \cdots & \frac{\partial f_n}{\partial \delta_k} \end{bmatrix}_{(\boldsymbol{x}_0,\boldsymbol{\delta}_0)}
\end{aligned} \tag{5.13}$$

where x_1, x_2, $\cdots$, x_n indicate n states, δ_1, δ_2, $\cdots$, δ_k indicate k control inputs of the system. Therefore, $\boldsymbol{A}$ and $\boldsymbol{B}$ are n by n and n by k matrices, respectively.

In linear systems theory, the Δ notation, which denotes the distance from the equilibrium point is conventionally dropped. The conventional notation is adopted in this research, too. Hence, the linear time-invariant approximation of the original nonlinear system will be represented as $\dot{\boldsymbol{x}} = \boldsymbol{A}\boldsymbol{x} + \boldsymbol{B}\boldsymbol{\delta}$ from this point forward.

In this research, MATLAB's linear analysis toolbox is utilized to linearize the aircraft dynamics. This toolbox linearizes the system numerically by perturbing all the states and control inputs one at a time and measuring the system response to these perturbations [34]. After the linearization is performed, the linearized system with state and input vectors:

$$\begin{aligned} \boldsymbol{x} &= \begin{bmatrix} V & \chi & \gamma & \phi & \alpha & \beta & p & q & r \end{bmatrix}^T \\ \boldsymbol{\delta} &= \begin{bmatrix} \delta_t & \delta_e & \delta_a & \delta_r \end{bmatrix}^T \end{aligned} \tag{5.14}$$

is found as

$$\dot{\boldsymbol{x}} = \boldsymbol{A}\,\boldsymbol{x} + \boldsymbol{B}\,\boldsymbol{\delta}$$

$$\boldsymbol{A} = \begin{bmatrix} -0.0996 & 0 & -9.7966 & 0 & -8.2222 & 0 & 0 & 0 & 0 \\ 0 & 0 & 0 & 0.2585 & 0 & 0.1378 & 0.0002 & 0 & -0.0115 \\ 0.0133 & 0 & -0.0135 & 0 & 0.9613 & 0 & 0 & 0.0361 & 0 \\ 0 & 0 & 0 & -0.0135 & 0 & -0.0072 & 0.9877 & 0 & 0.1570 \\ -0.0133 & 0 & 0.0135 & 0 & -0.9613 & 0 & 0 & 0.9639 & 0 \\ 0 & 0 & 0 & 0.2581 & 0 & 0.1377 & 0.1566 & 0 & -0.9992 \\ 0 & 0 & 0 & 0 & 0 & -11.8665 & -3.2944 & 0 & 5.1367 \\ 0 & 0 & 0 & 0 & -1.7650 & 0 & 0 & -1.0015 & 0 \\ 0 & 0 & 0 & 0 & 0 & 1.6343 & -0.1735 & 0 & -0.2261 \end{bmatrix} \tag{5.15}$$

$$\boldsymbol{B} = \begin{bmatrix} 6.2214 & 0 & 0 & 0 \\ 0 & 0 & 0 & -0.0482 \\ 0.0260 & 0.0722 & 0 & 0 \\ 0 & 0 & 0 & 0.0025 \\ -0.0260 & -0.0722 & 0 & 0 \\ 0 & 0 & 0 & -0.0481 \\ 0 & 0 & 9.6637 & 2.2738 \\ 0 & -2.6475 & 0 & 0 \\ 0 & 0 & -0.0089 & -1.3590 \end{bmatrix}$$

5.2 Appended Dynamics

The aircraft dynamics are linearized at the equilibrium point in the previous section. In this section, this linear model and actuator model are appended because the controller generates commanded input signals to the appended system rather than direct inputs to the aircraft. This way, the actuator dynamics are accounted for in the design of the controller.

The actuator dynamics are described in Section 3.2.3. Note that this system is not a linear system because of the nonlinearities introduced by the rate and position limiters.

In Section 5.1.1, fixed control inputs at the equilibrium point are found, and the results are given in Table 5.1. The control inputs being fixed dictates $\dot{\delta}_t, \dot{\delta}_e, \dot{\delta}_a, \dot{\delta}_r \equiv 0$. Also, the steady-state values of the control inputs are within the position limits, so the nonlinearities introduced by the limiters are not a concern at the equilibrium point, and the system behavior is linear. So the behavior of the system at the equilibrium point is given by the following state-space model:

$$\dot{\boldsymbol{\delta}} = \boldsymbol{A}_{act}\,\boldsymbol{\delta} + \boldsymbol{B}_{act}\,\boldsymbol{\delta}_c$$

$$\boldsymbol{A}_{act} = \begin{bmatrix} -\frac{1}{\tau_2} & 0 & 0 & 0 \\ 0 & -\frac{1}{\tau_1} & 0 & 0 \\ 0 & 0 & -\frac{1}{\tau_1} & 0 \\ 0 & 0 & 0 & -\frac{1}{\tau_1} \end{bmatrix}, \quad \boldsymbol{B}_{act} = \begin{bmatrix} \frac{1}{\tau_2} & 0 & 0 & 0 \\ 0 & \frac{1}{\tau_1} & 0 & 0 \\ 0 & 0 & \frac{1}{\tau_1} & 0 \\ 0 & 0 & 0 & \frac{1}{\tau_1} \end{bmatrix} \tag{5.16}$$

A composite state-space model is found by appending the state-space models in Equations 5.15 and 5.16 as

$$\dot{\boldsymbol{x}}_{app} = \boldsymbol{A}_{app}\,\boldsymbol{x}_{app} + \boldsymbol{B}_{app}\,\boldsymbol{\delta}_c$$

$$\boldsymbol{x}_{app} = \begin{bmatrix} \boldsymbol{x} \\ \boldsymbol{\delta} \end{bmatrix}, \quad \boldsymbol{A}_{app} = \begin{bmatrix} \boldsymbol{A} & \boldsymbol{B} \\ \boldsymbol{0}_{4x9} & \boldsymbol{A}_{act} \end{bmatrix}, \quad \boldsymbol{B}_{app} = \begin{bmatrix} \boldsymbol{0}_{9x4} \\ \boldsymbol{B}_{act} \end{bmatrix} \tag{5.17}$$

5.3 Controller

The objective of the controller in this study is to provide a control input command to the actuators and the engine to track the flight-path command, $\boldsymbol{x}_{2c}$, that is generated by the guidance laws while keeping the aircraft near steady-state equilibrium point by regulating the states to zero. This objective is achieved with a type 1 servo system.

5.3.1 Servo System Architecture and Error Dynamics

The structure and properties of the type 1 servo system can be found in [30]. In this type of controller, an integral compensator is introduced in the feedforward path between the tracking error signal and the plant (actuator+aircraft) to achieve zero steady-state tracking error for a step reference input. A block diagram for a type 1 servo system is given in Figure 5.2 where

$$
\begin{aligned}
u &\equiv \boldsymbol{\delta}_c = control\ signal \\
y &\equiv \boldsymbol{x}_2 = output\ signal \\
r &\equiv \boldsymbol{x}_{2c} = reference\ input\ signal \\
\dot{\xi} &\equiv \boldsymbol{e}_2 = \boldsymbol{x}_{2c} - \boldsymbol{x}_2 = tracking\ error \\
\xi &\equiv \boldsymbol{\epsilon}_2 = output\ of\ the\ integrator \\
\boldsymbol{A} &\equiv \boldsymbol{A}_{app} = state\ matrix\ of\ the\ appended\ system \\
\boldsymbol{B} &\equiv \boldsymbol{B}_{app} = input\ matrix\ of\ the\ appended\ system \\
\boldsymbol{C} &\equiv \boldsymbol{C}_{app} = output\ matrix\ of\ the\ appended\ system
\end{aligned}
$$

The compensator dynamics are given as

$$
\begin{aligned}
\dot{\boldsymbol{\epsilon}}_2 = \boldsymbol{e}_2 = \boldsymbol{x}_{2c} - \boldsymbol{x}_2 = \boldsymbol{x}_{2c} - \boldsymbol{C}_{app}\boldsymbol{x}_{app} \\
\boldsymbol{C}_{app} = \begin{bmatrix} \boldsymbol{I}_{3x3} & \boldsymbol{0}_{3x10} \end{bmatrix}
\end{aligned}
\tag{5.18}
$$

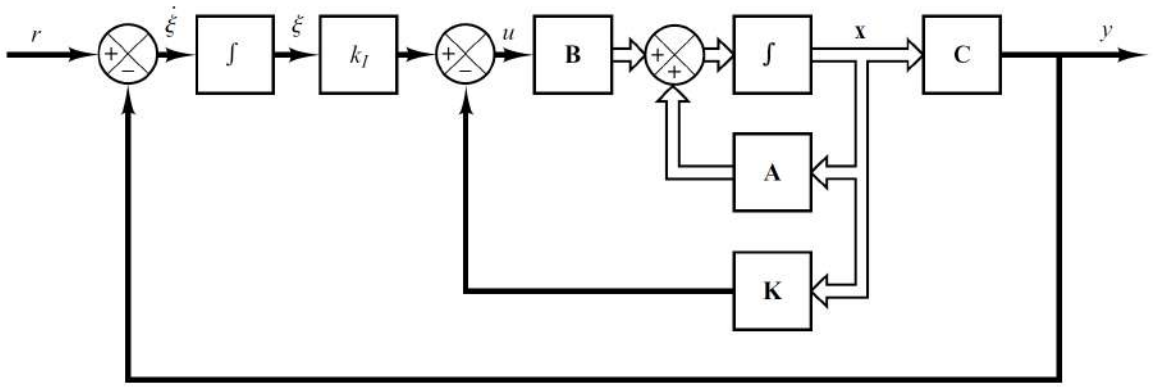

Figure 5.2. Block diagram for a type 1 servo system with integral compensator [30].

The servo system dynamics can be found by appending the plant and compensator dynamics and is given by an augmented state-space model as

$$\dot{\boldsymbol{x}}_{aug} = \boldsymbol{A}_{aug}\, \boldsymbol{x}_{aug} + \boldsymbol{B}_{aug}\, \boldsymbol{\delta}_c + \boldsymbol{F}_{aug}\, \boldsymbol{x}_{2c}$$

$$\boldsymbol{x}_{aug} = \begin{bmatrix} \boldsymbol{x}_{app} \\ \boldsymbol{\epsilon}_2 \end{bmatrix}, \boldsymbol{A}_{aug} = \begin{bmatrix} \boldsymbol{A}_{app} & \boldsymbol{0}_{13x3} \\ -\boldsymbol{C}_{app} & \boldsymbol{0}_{3x3} \end{bmatrix}, \boldsymbol{B}_{aug} = \begin{bmatrix} \boldsymbol{B}_{app} \\ \boldsymbol{0}_{3x4} \end{bmatrix}, \boldsymbol{F}_{aug} = \begin{bmatrix} \boldsymbol{0}_{13x3} \\ \boldsymbol{I}_{3x3} \end{bmatrix} \tag{5.19}$$

where the control law is

$$\begin{aligned} \boldsymbol{\delta}_c &= -\boldsymbol{K}_{aug}\, \boldsymbol{x}_{aug} \\ \boldsymbol{K}_{aug} &= \begin{bmatrix} \boldsymbol{K} & -\boldsymbol{k}_I \end{bmatrix} \end{aligned} \tag{5.20}$$

The goal is to design an asymptotically stable system such that $\boldsymbol{x}_{app}(\infty)$, $\boldsymbol{\epsilon}_2(\infty)$ and $\boldsymbol{\delta}_c(\infty)$ approach constant values. Note that $\boldsymbol{\epsilon}_2(\infty)$ approaching a constant value ensures zero tracking error at steady state for a step reference input. At steady state, we have

$$\dot{\boldsymbol{x}}_{aug}(\infty) = \boldsymbol{A}_{aug}\, \boldsymbol{x}_{aug}(\infty) + \boldsymbol{B}_{aug}\, \boldsymbol{\delta}_c(\infty) + \boldsymbol{F}_{aug}\, \boldsymbol{x}_{2c}(\infty) \tag{5.21}$$

For a step reference input, $\boldsymbol{x}_{2c}(\infty) = \boldsymbol{x}_{2c}$; hence, by subtracting Equation 5.21 from Equation 5.19, we get

$$\begin{aligned} \dot{\boldsymbol{e}}_{\boldsymbol{x}_{aug}} &= \boldsymbol{A}_{aug}\, \boldsymbol{e}_{\boldsymbol{x}_{aug}} + \boldsymbol{B}_{aug}\, \boldsymbol{e}_{\boldsymbol{\delta}_c} \\ \boldsymbol{e}_{\boldsymbol{x}_{aug}} &= \boldsymbol{x}_{aug} - \boldsymbol{x}_{aug}(\infty) \\ \boldsymbol{e}_{\boldsymbol{\delta}_c} &= \boldsymbol{\delta}_c - \boldsymbol{\delta}_c(\infty) \end{aligned} \tag{5.22}$$

The control law for Equation 5.22 is found by substituting the expression for $\boldsymbol{\delta}_c$ in Equation 5.20 into Equation 5.22 as

$$\begin{aligned} \boldsymbol{e}_{\boldsymbol{\delta}_c} &= -\,\boldsymbol{K}_{aug}\,(\boldsymbol{x}_{aug} - \boldsymbol{x}_{aug}(\infty)) \\ &= -\,\boldsymbol{K}_{aug}\,\boldsymbol{e}_{\boldsymbol{x}_{aug}} \end{aligned} \tag{5.23}$$

Substituting the control law into the error dynamics gives the closed loop dynamics as

$$\dot{\boldsymbol{e}}_{\boldsymbol{x}_{aug}} = (\boldsymbol{A}_{aug} - \boldsymbol{B}_{aug}\boldsymbol{K}_{aug})\, \boldsymbol{e}_{\boldsymbol{x}_{aug}} \tag{5.24}$$

Equation 5.24 implies that the stability of the closed loop system is imposed by the eigenvalues of $\boldsymbol{A}_{aug} - \boldsymbol{B}_{aug}\boldsymbol{K}_{aug}$. Therefore, the feedback gain matrix, $\boldsymbol{K}_{aug}$, must be designed so that the closed loop system has the desired stability characteristics.

5.3.2 Linear Quadratic Integral Optimal Controller

A Linear-Quadratic-Integral (LQI) optimal control method is employed in the design of the feedback gain matrix. Note that the integral compensator is already appended to the plant dynamics previously. Hence, the design of an LQI controller for the plant is equivalent to the design of a Linear-Quadratic Regulator(LQR) for the augmented system (plant+compensator). In the LQR design, closed-loop eigenvalues are not specified; instead, they are assigned by an optimization method that minimizes a cost function, which is also called the performance index. In order to understand

the performance index, we need to define state and control energies for an LTI system, which is given by $\dot{\boldsymbol{x}} = \boldsymbol{A}\boldsymbol{x} + \boldsymbol{B}\boldsymbol{u}$, as

$$\begin{aligned} \textit{state energy} &= \int_0^\infty (\boldsymbol{x}^T\boldsymbol{x})\, dt \\ \textit{control energy} &= \int_0^\infty (\boldsymbol{u}^T\boldsymbol{u})\, dt \end{aligned} \tag{5.25}$$

It is desirable to minimize both state and control energies to achieve the controller objective, e.g., tracking a reference input, regulating the states. However, it is often conflicting to do so because low state energy requires high control effort and vice versa. The performance index penalizes both state and control energies in a linear-quadratic form and is given as [35]

$$J = \frac{1}{2}\int_0^\infty (\boldsymbol{x}^T\boldsymbol{Q}\boldsymbol{x} + \boldsymbol{u}^T\boldsymbol{R}\boldsymbol{u})\, dt \tag{5.26}$$

where $\boldsymbol{Q}$ and $\boldsymbol{R}$ matrices are the state and input weighting matrices, respectively. The diagonal elements of the weighting matrices determine the relative contribution of each state and input to the performance index.

In optimal control theory, the Lagrange multipliers, $\boldsymbol{\lambda}$, are introduced to convert the problem of minimizing the performance index subject to the system dynamics into the problem of minimizing the Hamiltonian without constraints [36]. The Hamiltonian is given as

$$H(\boldsymbol{x}, \boldsymbol{u}, \boldsymbol{\lambda}) = J(\boldsymbol{x}, \boldsymbol{u}) + \boldsymbol{\lambda}^T(\boldsymbol{A}\boldsymbol{x} + \boldsymbol{B}\boldsymbol{u}) \tag{5.27}$$

The feedback gain matrix that minimizes the Hamiltonian is calculated as

$$\boldsymbol{K} = \boldsymbol{R}^{-1}\boldsymbol{B}^T\boldsymbol{S} \tag{5.28}$$

where $\boldsymbol{S}$ is the positive definite solution of the matrix Riccati equation:

$$\boldsymbol{A}^T\boldsymbol{S} + \boldsymbol{S}\boldsymbol{A} - \boldsymbol{S}\boldsymbol{B}\boldsymbol{R}^{-1}\boldsymbol{B}^T\boldsymbol{S} + \boldsymbol{Q} = 0 \tag{5.29}$$

In MATLAB, all the steps of the LQR design are streamlined in the "lqr" command. The command forms the matrix Riccati equation, finds the positive definite solution, and returns the optimal feedback gain matrix.

5.3.3 Weighting Matrices

Although the LQR design is theoretically straightforward to apply, it is very challenging to implement for practical applications. This problem arises because the relation between the weights and the response waveforms is not so clear as to enable the designer to perform fine adjustments intuitively to achieve the desired response[37]. This flaw is especially prominent in MIMO systems since multiple weights must be tuned all at once. In this study, there are sixteen states and four inputs constituting the augmented system; hence, twenty weights must be tuned all at once, which is a daunting task. For this reason, trial and error is not an option.

An intuitive approach for selecting appropriate $\boldsymbol{Q}$ and $\boldsymbol{R}$ matrices is suggested by Bryson [38]. In this approach, the maximum allowable displacements of the states and inputs from the steady state are defined by $(x_i)_{max}$ and $(u_i)_{max}$, respectively. The weighting matrices are calculated using these quantities as

$$\boldsymbol{Q} = diag\left(\frac{1}{{(x_i)_{max}}^2}\right), \quad \boldsymbol{R} = diag\left(\frac{1}{{(u_i)_{max}}^2}\right) \tag{5.30}$$

In this study, three controllers are designed. The maximum allowable displacements are varied amongst the three controllers to perform a trade-off between tracking precision and minimal control energy. The tracking precision is favored progressively more over minimal control energy from the first controller to the third controller. The

feedback gain matrices corresponding to the each controller are denoted as $\boldsymbol{K}_{aug_1}$, $\boldsymbol{K}_{aug_2}$ and $\boldsymbol{K}_{aug_3}$. Then the control strategy is given as

$$\boldsymbol{K}_{aug} = \begin{cases} \boldsymbol{K}_{aug_1}, & \hat{d} \geq d_1 \\ \boldsymbol{X}_1\hat{d}^2 + \boldsymbol{Y}_1\hat{d} + \boldsymbol{Z}_1, & d_1 > \hat{d} > d_2 \\ \boldsymbol{X}_2\hat{d}^2 + \boldsymbol{Y}_2\hat{d} + \boldsymbol{Z}_2, & d_2 \geq \hat{d} > d_3 \\ \boldsymbol{K}_{aug_3}, & d_3 \geq \hat{d} \end{cases} \tag{5.31}$$

where $\hat{d}$ is the estimated distance from the aircraft to the desired touchdown point and $d_1 = 1000\,m$, $d_2 = 500\,m$, $d_3 = 50\,m$. A second-order interpolation scheme is used calculate the constants of the interpolation as

$$\begin{aligned} \boldsymbol{X}_1 &= \frac{\boldsymbol{K}_{aug_1} - \boldsymbol{K}_{aug_2}}{(d_1^2 - d_2^2) - 2d_1(d_1 - d_2)}, \quad \boldsymbol{Y}_1 = -2\boldsymbol{X}_1 d_1, \quad \boldsymbol{Z}_1 = \boldsymbol{K}_{aug_1} - \boldsymbol{X}_1 d_1^2 - \boldsymbol{Y}_1 d_1 \\ \boldsymbol{X}_2 &= \frac{\boldsymbol{K}_{aug_2} - \boldsymbol{K}_{aug_3}}{(d_2^2 - d_3^2) - 2d_2(d_2 - d_3)}, \quad \boldsymbol{Y}_2 = -2\boldsymbol{X}_2 d_2, \quad \boldsymbol{Z}_2 = \boldsymbol{K}_{aug_2} - \boldsymbol{X}_2 d_2^2 - \boldsymbol{Y}_2 d_2 \end{aligned} \tag{5.32}$$

The maximum allowable deviations for each controller are given in Table 5.2. Note that the allowable deviation of the course angle is specified as infinity because a desired steady-state value does not exist. The actual value of the course angle is taken as zero for the trim algorithm only to narrow down the scope of the search for the local minimum. Any arbitrary value could have been chosen. Thus, the controller must be designed so that the deviation from the artificially introduced steady-state value of the course angle does not have any effect on the control inputs.

Table 5.2. Maximum allowable deviations

		Controller 1	Controller 2	Controller 3
$(x_i)_{max}$	$V(m/s)$	0.2	0.2	0.2
	$\chi(deg)$	∞	∞	∞
	$\gamma(deg)$	0.1	0.1	0.1
	$\phi(deg)$	2	2	2
	$\alpha(deg)$	1	1	1
	$\beta(deg)$	0.2	0.2	0.2
	$p(deg/s)$	5	5	5
	$q(deg/s)$	5	5	5
	$r(deg/s)$	5	5	5
	δ_t	1	1	1
	$\delta_e(deg)$	10	10	20
	$\delta_a(deg)$	10	10	10
	$\delta_r(deg)$	10	10	10
	ϵ_V	0.4	0.2	0.1
	ϵ_χ	1	1	1
	ϵ_γ	0.2	0.1	0.05
$(u_i)_{max}$	δ_{tc}	4	4	4
	$\delta_{ec}(deg)$	40	40	80
	$\delta_{ac}(deg)$	40	40	40
	$\delta_{rc}(deg)$	40	40	40

CHAPTER 6

DECK MOTION ESTIMATION

6.1 Introduction

In Chapter 4, the reference trajectory is generated. Remember, the reference trajectory refers to the dynamics of the reference point along the glide path, which is an imaginary line between the desired touchdown point and the reference point. A navigation problem arises because the reference trajectory generation requires the knowledge of the desired touchdown point location and the orientation of the runway with respect to the aircraft. Previously, the exact knowledge of the carrier states is assumed. In this chapter, the navigation problem at hand is addressed and the carrier states are estimated using an airborne measurement system. This brings another level of difficulty to this study because the estimation errors must be accounted for in order to achieve a safe and precise landing.

Various navigation systems have been developed to enable autonomous landing of the aircraft on a moving carrier deck such as shipboard tracking radar system and shipboard relative GPS [15]. The classical ACLS (Automatic Carrier Landing System) uses both the shipboard computer from the carrier and the autopilot at the aircraft. Any information required from the carrier for a safe landing is transmitted through a data link, which is vulnerable to communication problems in the shipboard broadcasting system [2]. These systems provide accurate information, but they rely on costly and bulky equipment [39].

Using an airborne measurement system for navigation merges as a way to eliminate the necessity of wireless communication and allows safe landing operations in

the presence of communication problems. It provides abundant information at low-cost thanks to the advancements in the optoelectronics technology [39]. The passive nature of the vision-based systems allows stealtier operations since the UAV is not illuminated by the shipboard radar.

6.2 Position and Attitude Estimation

A vision-based measurement system which is composed of four beacons and an airborne receiver sensor is proposed to estimate the carrier states.

A schematic that describes the geometry of the navigation problem is given in Figure 6.1. In this figure, four beacons that are placed on the deck are shown by the dots. The C-frame corresponds to the body-fixed frame of the airborne sensor.

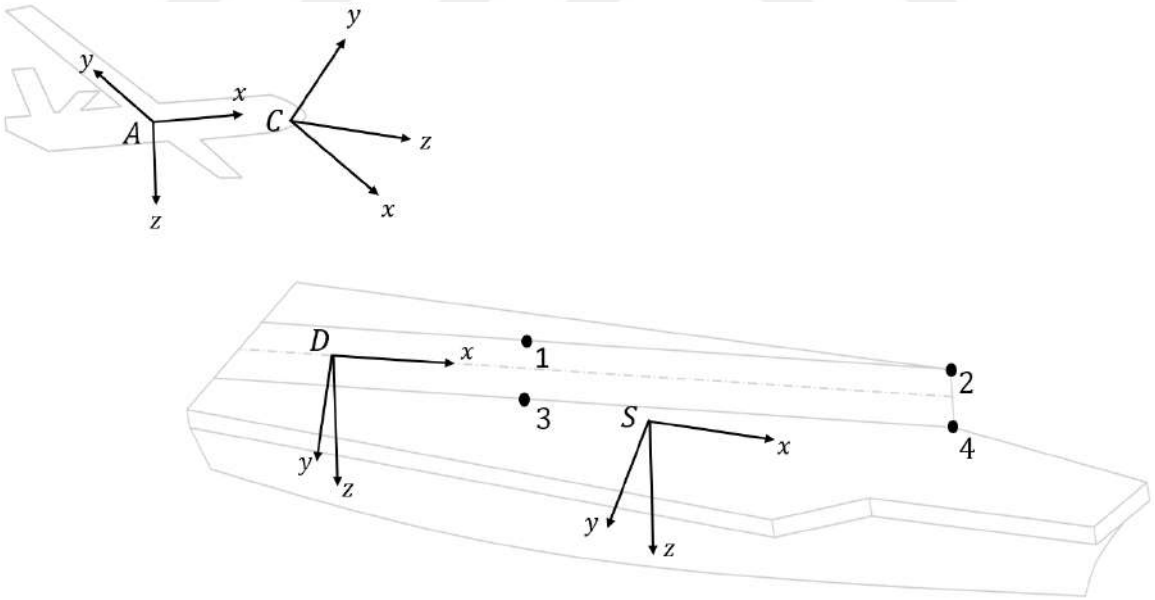

Figure 6.1. Vision-based measurement system.

The vision-based airborne sensor is a camera utilizing Position Sensing Diode (PSD) technology. It receives the light signals that are emitted by the beacons. The

PSD detects the beacons through line-of-sight measurements and forms an image on its focal plane.

The z-axis of the C-frame is directed outward along the boresight of the PSD. The x and y axes constitute a plane parallel to the focal plane. The one-to-one correspondence between the known beacon locations in the D-frame and measured image coordinates on the focal plane is exploited in the estimation of the desired touchdown point location and runway attitude relative to the aircraft.

In the literature, the problem of estimating relative position and attitude of a calibrated camera from a known scene and measured image coordinates is referred to as the Perspective-n-Point (PnP) problem where n indicates the number of known point correspondences in the scene [40]. This problem is discussed in detail in [41] and has been studied extensively in computer vision and robotics fields. At least three noncollinear point correspondences are required to obtain a finite number of solutions to the estimation problem, and various algorithms have been proposed for three (P3P), four (P4P), five (P5P) and a general number of point correspondences (PnP) [42]. The P3P problem can have as many as four possible solutions, while the P4P problem has a single theoretical solution for coplanar, noncollinear points in an ordinary configuration [43].

Iterative and noniterative approaches to the solution of the PnP problem have been proposed in the literature. In general, iterative methods are known to be very robust to noise but computationally costly, whereas noniterative methods are computationally efficient but sensitive to noise. Also, noniterative methods are inherently more susceptible to pose ambiguity [43].

The P4P problem at hand is formulated as a nonlinear least-squares (NLS) problem. In this method, an observation model, which is an object to image projective transformation, is employed. An estimated measurement is calculated based on an

initial estimate of the states of the observation model. The error between the actual and estimated values of the measurement is minimized by applying corrections to the initial estimate of the states. The corrections are applied iteratively until the error is sufficiently small.

6.2.1 Observation Model

The observation model is a projective transformation of the feature points in three-dimensional object space to the two-dimensional image plane, i.e., the observation model finds the image coordinates of the feature points in a given scene.

Note that the position vector from the C-frame to i^{th} beacon can be expressed in the C-frame as

$$\boldsymbol{r}_{Ci}^{C} = \boldsymbol{R}_{CD}\, \boldsymbol{r}_{Ci}^{D} = \boldsymbol{R}_{CD}\, (\boldsymbol{r}_{Di}^{D} - \boldsymbol{r}_{DC}^{D}) = \begin{bmatrix} x_{Ci}^{C} & y_{Ci}^{C} & z_{Ci}^{C} \end{bmatrix}^{T} \tag{6.1}$$

A pinhole camera model is illustrated in Figure 6.2 and used to describe the projection from the C-frame to the image plane as

$$\frac{x_{Ci}^{C}}{-x_{i}^{im}} = \frac{y_{Ci}^{C}}{-y_{i}^{im}} = \frac{z_{Ci}^{C}}{f} \tag{6.2}$$

where f is the focal length of the camera and it is known from the calibration.

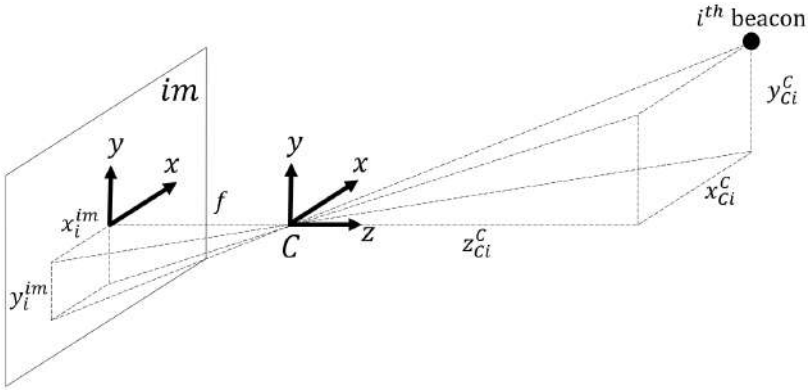

Figure 6.2. Object space to image plane projection for a pinhole camera model.

The image coordinates of the i^{th} beacon can be found as

$$x_i^{im} = -f\frac{x_{Ci}^C}{z_{Ci}^C}, \quad y_i^{im} = -f\frac{y_{Ci}^C}{z_{Ci}^C} \tag{6.3}$$

Substitution of Equation 6.1 into Equation 6.3 gives

$$\begin{aligned} x_i^{im} &= -f\frac{\boldsymbol{R}_{CD}(1,1)\,(x_{Di}^D - x_{DC}^D) + \boldsymbol{R}_{CD}(1,2)\,(y_{Di}^D - y_{DC}^D) + \boldsymbol{R}_{CD}(1,3)\,(z_{Di}^D - z_{DC}^D)}{\boldsymbol{R}_{CD}(3,1)\,(x_{Di}^D - x_{DC}^D) + \boldsymbol{R}_{CD}(3,2)\,(y_{Di}^D - y_{DC}^D) + \boldsymbol{R}_{CD}(3,3)\,(z_{Di}^D - z_{DC}^D)} \\ y_i^{im} &= -f\frac{\boldsymbol{R}_{CD}(2,1)\,(x_{Di}^D - x_{DC}^D) + \boldsymbol{R}_{CD}(2,2)\,(y_{Di}^D - y_{DC}^D) + \boldsymbol{R}_{CD}(2,3)\,(z_{Di}^D - z_{DC}^D)}{\boldsymbol{R}_{CD}(3,1)\,(x_{Di}^D - x_{DC}^D) + \boldsymbol{R}_{CD}(3,2)\,(y_{Di}^D - y_{DC}^D) + \boldsymbol{R}_{CD}(3,3)\,(z_{Di}^D - z_{DC}^D)} \end{aligned} \tag{6.4}$$

Equation 6.4 is also called the collinearity equations. The collinearity equations can be reconstructed in a simpler vector form as [44]

$$\boldsymbol{b}_i = \boldsymbol{R}_{CD}\,\boldsymbol{r}_i \tag{6.5}$$

where

$$\begin{aligned} \boldsymbol{b}_i &= \frac{1}{\sqrt{f^2 + (x_i^{im})^2 + (y_i^{im})^2}} \begin{bmatrix} -x_i^{im} \\ -y_i^{im} \\ f \end{bmatrix} \\ \boldsymbol{r}_i &= \frac{1}{\sqrt{(x_{Di}^D - x_{DC}^D)^2 + (y_{Di}^D - y_{DC}^D)^2 + (z_{Di}^D - z_{DC}^D)^2}} \begin{bmatrix} -x_i^{im} \\ -y_i^{im} \\ f \end{bmatrix} \end{aligned} \tag{6.6}$$

The known quantities in this observation model are x_i^{im}, y_i^{im} and $\boldsymbol{r}_{Di}^D = \begin{bmatrix} x_{Di}^D & y_{Di}^D & z_{Di}^D \end{bmatrix}^T$. The state vector is given as

$$\boldsymbol{x} = \begin{bmatrix} \boldsymbol{x}_1^T & \boldsymbol{x}_2^T \end{bmatrix}^T, \quad \boldsymbol{x}_1 = \boldsymbol{p}, \quad \boldsymbol{x}_2 = \boldsymbol{r}_{DC}^D \tag{6.7}$$

where $\boldsymbol{p}$ represents the modified Rodrigues parameters of the rotation and the rotation matrix is calculated from the modified Rodrigues parameters as follows [44]:

$$\boldsymbol{R}_{CD} = \boldsymbol{I} - \frac{4(1 - \boldsymbol{p}^T\boldsymbol{p})}{(1 + \boldsymbol{p}^T\boldsymbol{p})^2} S(\boldsymbol{p}) + \frac{8}{(1 + \boldsymbol{p}^T\boldsymbol{p})^2} S(\boldsymbol{p})^2 \tag{6.8}$$

6.2.2 Nonlinear Least Squares Estimation

The NLS estimation algorithm from [44] is utilized to estimate the states of the observation model. The observation model is given as, $\boldsymbol{y} = \boldsymbol{f}(\boldsymbol{x})$, where

$$\boldsymbol{y} = \begin{bmatrix} \boldsymbol{b}_1 \\ \boldsymbol{b}_2 \\ \boldsymbol{b}_3 \\ \boldsymbol{b}_4 \end{bmatrix}, \quad \boldsymbol{f}(\boldsymbol{x}) = \begin{bmatrix} \boldsymbol{f}_1(\boldsymbol{x}) \\ \boldsymbol{f}_2(\boldsymbol{x}) \\ \boldsymbol{f}_3(\boldsymbol{x}) \\ \boldsymbol{f}_4(\boldsymbol{x}) \end{bmatrix} = \begin{bmatrix} \boldsymbol{R}_{CD}\boldsymbol{r}_1 \\ \boldsymbol{R}_{CD}\boldsymbol{r}_2 \\ \boldsymbol{R}_{CD}\boldsymbol{r}_3 \\ \boldsymbol{R}_{CD}\boldsymbol{r}_4 \end{bmatrix} \tag{6.9}$$

Let us assume the observed values are corrupted by measurement noise, $\boldsymbol{v}_m$. Hence, the measured values can be expressed as

$$\tilde{\boldsymbol{y}} = \boldsymbol{f}(\boldsymbol{x}) + \boldsymbol{v}_m \tag{6.10}$$

Starting with an initial estimate of the state vector, $\hat{\boldsymbol{x}}$, an estimated output vector, $\hat{\boldsymbol{y}}$, can be calculated using the observation model as

$$\hat{\boldsymbol{y}} = \boldsymbol{f}(\hat{\boldsymbol{x}}) \tag{6.11}$$

A residual error is calculated between the measured and estimated output values as

$$\boldsymbol{e} = \Delta\boldsymbol{y} = \tilde{\boldsymbol{y}} - \hat{\boldsymbol{y}} \tag{6.12}$$

A cost function which penalizes the residual error can now be constructed as

$$J = \frac{1}{2}\boldsymbol{e}^T\boldsymbol{W}\boldsymbol{e} \tag{6.13}$$

where $\boldsymbol{W}$ is a diagonal weighting matrix. The problem is converted into an optimization problem in which the cost function; hence, the residual error is minimized. The strategy to minimize the residual error is to update the current estimate of the states of the observation in successive iterations so that the residual error diminishes. The current estimate of the state vector is denoted as $\boldsymbol{x}_c$ and the estimated state vector

in the next iteration is related to the current estimate of the state vector through an unknown correction, $\Delta \boldsymbol{x}$, such that

$$\hat{\boldsymbol{x}} = \boldsymbol{x}_c + \Delta \boldsymbol{x} \tag{6.14}$$

Assuming that $\Delta \boldsymbol{x}$ is sufficiently small, Taylor series expansion can be used to linearize $\boldsymbol{f}(\hat{\boldsymbol{x}})$ about $\boldsymbol{x}_c$ by neglecting higher order terms as follows:

$$\begin{aligned} \hat{\boldsymbol{y}} = \boldsymbol{f}(\hat{\boldsymbol{x}}) = \boldsymbol{f}(\boldsymbol{x}_c + \Delta \boldsymbol{x}) = \boldsymbol{f}(\boldsymbol{x}_c) + \boldsymbol{H}\, \Delta \boldsymbol{x} + H.O.T. \\ \approx \boldsymbol{f}(\boldsymbol{x}_c) + \boldsymbol{H}\, \Delta \boldsymbol{x} \end{aligned} \tag{6.15}$$

where $\boldsymbol{H}$ is the Jacobian matrix of the observation model and can be calculated as

$$\boldsymbol{H} = \left.\frac{\partial \boldsymbol{f}}{\partial \boldsymbol{x}}\right|_{\boldsymbol{x}_c} = \begin{bmatrix} \frac{\partial \boldsymbol{f}_1}{\partial \boldsymbol{p}} & \frac{\partial \boldsymbol{f}_1}{\partial \boldsymbol{r}_{DC}^D} \\ \vdots & \vdots \\ \frac{\partial \boldsymbol{f}_4}{\partial \boldsymbol{p}} & \frac{\partial \boldsymbol{f}_4}{\partial \boldsymbol{r}_{DC}^D} \end{bmatrix}_{(\boldsymbol{x}_c)} \tag{6.16}$$

The partial derivatives which appear in the Jacobian are given as

$$\begin{aligned} \frac{\partial \boldsymbol{f}_i}{\partial \boldsymbol{p}} = \frac{\partial (\boldsymbol{R}_{CD}\, \boldsymbol{r}_i)}{\partial \boldsymbol{p}} = \frac{4}{\left(1 + \boldsymbol{p}^T \boldsymbol{p}\right)^2} S(\boldsymbol{R}_{CD}\, \boldsymbol{r}_i) \left((1 - \boldsymbol{p}^T \boldsymbol{p}) \boldsymbol{I} - 2S(\boldsymbol{p}) + 2\boldsymbol{p}\boldsymbol{p}^T \right) \\ \frac{\partial \boldsymbol{f}_i}{\partial \boldsymbol{r}_{DC}^D} = \boldsymbol{R}_{CD} \left(\frac{(\boldsymbol{r}_{Di}^D - \boldsymbol{r}_{DC}^D)(\boldsymbol{r}_{Di}^D - \boldsymbol{r}_{DC}^D)^T}{\left\| \boldsymbol{r}_{Di}^D - \boldsymbol{r}_{DC}^D \right\|^3} - \frac{\boldsymbol{I}}{\left\| \boldsymbol{r}_{Di}^D - \boldsymbol{r}_{DC}^D \right\|} \right) \end{aligned} \tag{6.17}$$

Using the linearized model, the residual error can be approximated as

$$\Delta \boldsymbol{y} \approx \Delta \boldsymbol{y}_c - \boldsymbol{H}\, \Delta \boldsymbol{x} \tag{6.18}$$

where $\Delta \boldsymbol{y}_c$ is called the residual error before the correction and is given as

$$\Delta \boldsymbol{y}_c = \tilde{\boldsymbol{y}} - \boldsymbol{f}(\boldsymbol{x}_c) \tag{6.19}$$

Remember the objective is to minimize the cost function J. The local strategy for determining the approximate corrections in $\Delta \boldsymbol{x}$ is to select the particular corrections

that minimize the sum of squares of the linearly predicted residuals J_p which is given as

$$J_p = \frac{1}{2}(\Delta \boldsymbol{y}_c - \boldsymbol{H}\ \Delta \boldsymbol{x})^T \boldsymbol{W} (\Delta \boldsymbol{y}_c - \boldsymbol{H}\ \Delta \boldsymbol{x}) \approx J \tag{6.20}$$

Solving Equation 6.20 for $\Delta \boldsymbol{x}$ that minimizes J_p gives [44]

$$\Delta \boldsymbol{x} = (\boldsymbol{H}^T \boldsymbol{W} \boldsymbol{H})^{-1} \boldsymbol{H}^T \boldsymbol{W} \Delta \boldsymbol{y}_c \tag{6.21}$$

This correction is applied in each successive iteration till a convergence criterion is met. The convergence criterion is given by

$$\delta J = \frac{|J_i - J_{i-1}|}{J_i} < \frac{\varepsilon}{\|\boldsymbol{W}\|} \tag{6.22}$$

where ε can be used to tune the convergence accuracy. The NLS algorithm is summarized in Figure 6.3.

6.2.3 System Configuration

In this study, four beacons are placed on the carrier deck in a simple, coplanar configuration, as shown in Figure 6.4. The relative position vectors from the desired touchdown point to the beacons are expressed in the D-frame as $\boldsymbol{r}_{D1}^D = \begin{bmatrix} x_{D1}^D & y_{D1}^D & 0 \end{bmatrix}^T$, $\boldsymbol{r}_{D2}^D = \begin{bmatrix} x_{D2}^D & y_{D2}^D & 0 \end{bmatrix}^T$, $\boldsymbol{r}_{D3}^D = \begin{bmatrix} x_{D3}^D & y_{D3}^D & 0 \end{bmatrix}^T$, $\boldsymbol{r}_{D4}^D = \begin{bmatrix} x_{D4}^D & y_{D4}^D & 0 \end{bmatrix}^T$. The locations of the beacons are chosen to ensure they are within the field of view of the camera throughout the landing task and are given by $x_{D1}^D = x_{D3}^D = 75\,m$, $x_{D2}^D = x_{D4}^D = 150\,m$, $y_{D1}^D = y_{D2}^D = -15\,m$, $y_{D3}^D = y_{D4}^D = 15\,m$.

The Euler angles of the rotation from the A-frame to the C-frame are chosen as $\phi_{CA} = -75\,deg$, $\theta_{CA} = 0\,deg$, $\psi_{CA} = -90\,deg$ so that the z-axis of the C-frame is directed towards the desired touchdown point for $\theta \approx 6\,deg$ and $\lambda \approx 4\,deg$. The C-frame is located near the nose of the aircraft for maximum visibility; thus, $\boldsymbol{r}_{AC}^A$ is chosen as $\begin{bmatrix} 2 & 0 & 0.5 \end{bmatrix}^T$.

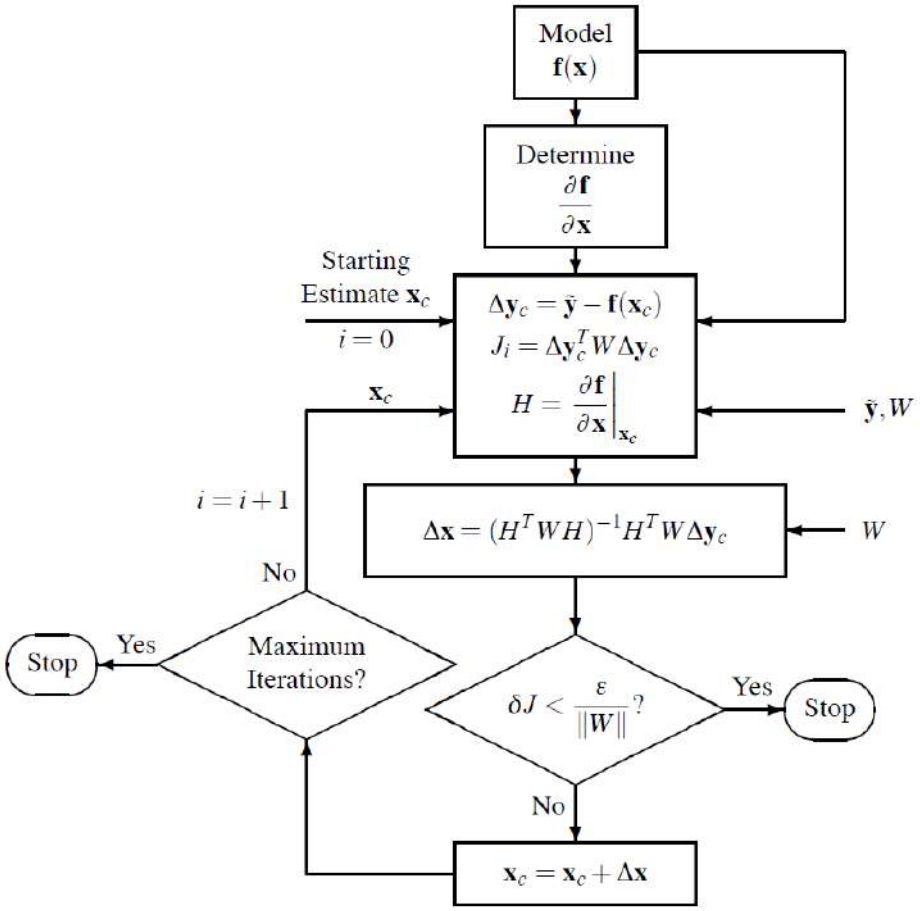

Figure 6.3. NLS algorithm [44].

The estimated position and attitude of the carrier deck are calculated as follows:

$$\begin{aligned} \hat{\boldsymbol{R}}_{DI} &= (\hat{\boldsymbol{R}}_{CD})^T \, \boldsymbol{R}_{CA} \, \boldsymbol{R}_{AI} \\ \hat{\boldsymbol{r}}^I_{ID} &= \boldsymbol{r}^I_{IA} + (\boldsymbol{R}_{AI})^T \, \boldsymbol{r}^A_{AC} - (\hat{\boldsymbol{R}}_{DI})^T \, \hat{\boldsymbol{r}}^D_{DC} \end{aligned} \tag{6.23}$$

where $\boldsymbol{R}_{CA}$ is the constant rotation matrix from the A-frame to the C-frame and given by the Euler angles, $\boldsymbol{\Phi}_{CA} = \begin{bmatrix} \phi_{CA} & \theta_{CA} & \psi_{CA} \end{bmatrix}^T$ and $\boldsymbol{r}^A_{AC}$ is the constant relative position vector from the A-frame to the C-frame.

The measurement error $\boldsymbol{v}_m$ is taken as zero-mean Gaussian with a standard deviation of 1/5000 of the focal length, and the focal length is given as $1\,m$ [44].

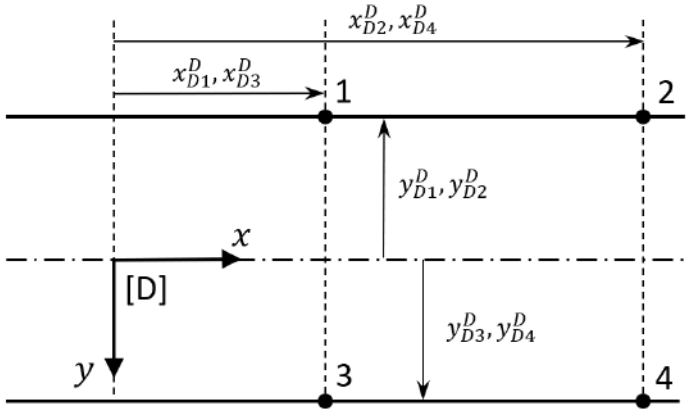

Figure 6.4. Locations of the beacons on the carrier deck.

6.3 Velocity Estimation

The reference trajectory generation and guidance laws require not only the position and attitude of the runway but also the velocity of the desired touchdown point. The velocity of the desired touchdown point is nothing but the derivative of the true position. However, the true value of the position is not known. Instead, we have an estimated value that is corrupted by the noise in the measurement. Therefore, a second-order low pass filter is introduced to filter the high frequencies from the estimated position signal. The second-order, low-pass filter is given by the transfer function:

$$G(s) = \frac{{w_n}^2}{s^2 + 2\zeta w_n s + {w_n}^2} \tag{6.24}$$

Once the high frequencies are filtered, the time derivative gives a better estimate of the true velocity. Let us denote the filtered position signal as $\boldsymbol{x}_1$, and its derivative as $\boldsymbol{x}_2$. Then, we have

$$\begin{aligned} \dot{\boldsymbol{x}}_1 &= \boldsymbol{x}_2 \\ \dot{\boldsymbol{x}}_2 &= -(2\zeta w_n \boldsymbol{x}_2 + {w_n}^2 \boldsymbol{x}_1) + {w_n}^2 \hat{\boldsymbol{r}}_{ID}^I \end{aligned} \tag{6.25}$$

The low-pass filter is designed to be critically damped to ensure near cut-off frequencies are attenuated well enough. The cut-off frequency is chosen as approx-

imately ten times the highest perturbation frequency due to the sea state, which is given in Table 3.2 as $0.5236\,rad/s$. Hence, we have

$$\zeta = 1, \quad w_n = 5\,rad/s \tag{6.26}$$

CHAPTER 7

RESULTS AND DISCUSSION

The performance of the autonomous landing system with airborne deck motion estimation is validated through simulation in this chapter.

Landing dispersion is one of the most important figures of merit in this study. In order to calculate the landing error, touchdown must be detected first. In the simulation, it is assumed that touchdown occurs when the aircraft enters a rectangular prism around the desired touchdown point. This rectangular prism is depicted in Figure 7.1 and defined by three conditions:

$$\begin{aligned} -x_{th_1} \leq (\boldsymbol{r}_{DA}^{D})_x \leq x_{th_2} \\ -y_{th_1} \leq (\boldsymbol{r}_{DA}^{D})_y \leq y_{th_2} \\ -z_{th} \leq (\boldsymbol{r}_{DA}^{D})_z \end{aligned} \tag{7.1}$$

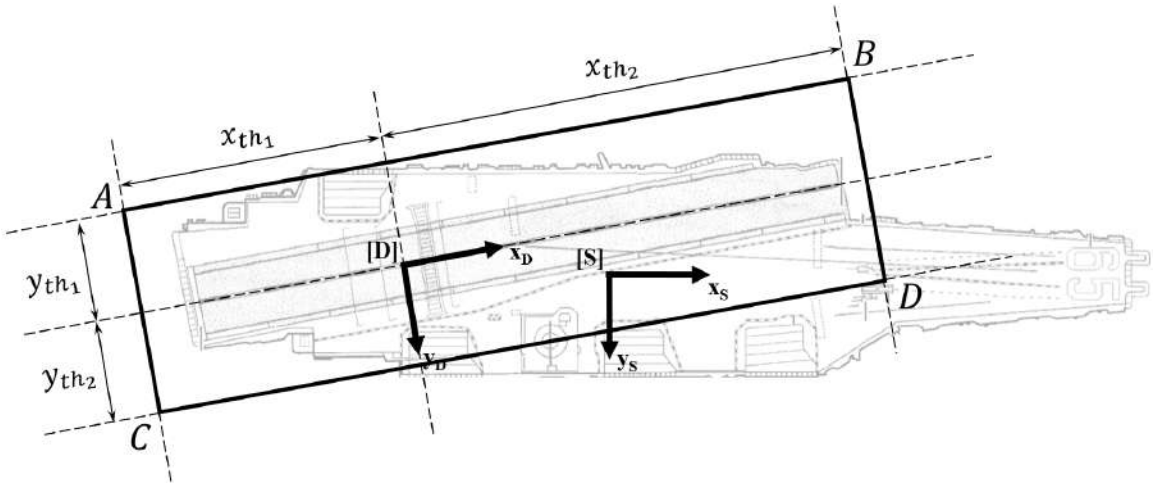

Figure 7.1. Touchdown condition.

Touchdown occurs when all three conditions are satisfied and then the simulation is stopped. The threshold values that define the rectangular prism are dictated by the dimensions of the CVN-65 carrier and chosen as $x_{th_1} = 100\,m$, $x_{th_2} = 250\,m$, $y_{th_1} = y_{th_2} = 40\,m$, $z_{th} = 0.005\,m$

The coordinates of the touchdown point are given by $(\boldsymbol{r}_{DA}^D)_x$ and $(\boldsymbol{r}_{DA}^D)_y$ when $(\boldsymbol{r}_{DA}^D)_z = 0$. The zero-crossing in the z-axis is found assuming the aircraft moves in a straight line in the last time step before the simulation stops. In Figure 7.2, the final time and the last time step of the simulation are indicated by t_f and T_1, respectively. Then, we have

$$\frac{T_1}{T_2} = \frac{Z_1}{Z_2}, \quad Z_1 = (\boldsymbol{r}_{DA}^D)_z\Big|_{t_f} - (\boldsymbol{r}_{DA}^D)_z\Big|_{t_f - T_1}, \quad Z_2 = -\left(\boldsymbol{r}_{DA}^D\right)_z\Big|_{t_f - T_1} \tag{7.2}$$

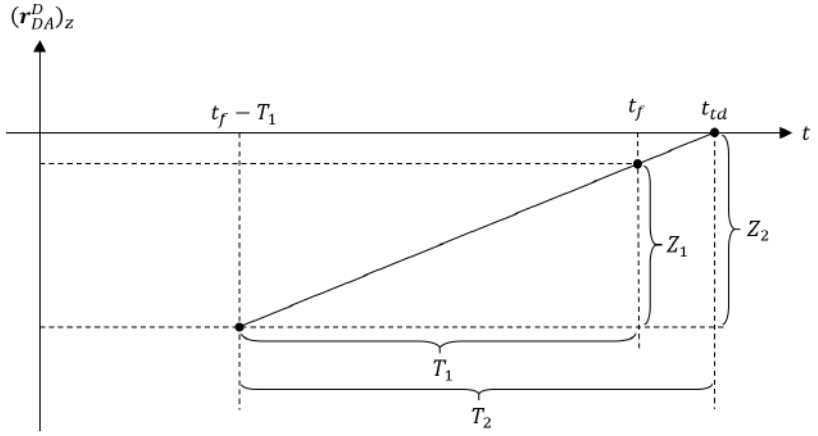

Figure 7.2. Zero-crossing in z-axis.

The longitudinal and lateral landing errors can be calculated as

$$\begin{aligned} X_1 &= (\boldsymbol{r}_{DA}^D)_x\Big|_{t_f} - (\boldsymbol{r}_{DA}^D)_x\Big|_{t_f - T_1}, \quad X_2 = X_1\frac{T_2}{T_1}, \quad e_{long} = X_2 + \left(\boldsymbol{r}_{DA}^D\right)_x\Big|_{t_f - T_1} \\ Y_1 &= (\boldsymbol{r}_{DA}^D)_y\Big|_{t_f} - (\boldsymbol{r}_{DA}^D)_y\Big|_{t_f - T_1}, \quad Y_2 = Y_1\frac{T_2}{T_1}, \quad e_{lat} = Y_2 + \left(\boldsymbol{r}_{DA}^D\right)_y\Big|_{t_f - T_1} \end{aligned} \tag{7.3}$$

According to [19], the ship motion is the dominant cause of the landing errors. The landing dispersion and boarding rates are highly dependent on the sea state. For this reason, it is vital in this study to randomize the initial conditions and perform Monte Carlo simulations to ensure plenty of possible scenarios are covered.

The initial position of the desired touchdown point is defined as the origin of the inertial frame. Hence, the initial position of the carrier becomes

$$\left(\boldsymbol{r}_{IS}^{I}\right)_i = -\left(\boldsymbol{R}_{SI}^{T}\right)_i \boldsymbol{r}_{SD}^{S} \tag{7.4}$$

It follows from Equations 3.2 and 3.6 that the initial velocity and Euler angles of the carrier due to the sea state are given as

$$\left(\boldsymbol{V}_{sea}^{S}\right)_i = \begin{bmatrix} A_{surge} w_{surge} \cos\left(\Delta_{surge}\right) \\ A_{sway} w_{sway} \cos\left(\Delta_{sway}\right) \\ A_{heave} w_{heave} \cos\left(\Delta_{heave}\right) \end{bmatrix}, \quad \left(\boldsymbol{\Phi}_S\right)_i = \begin{bmatrix} A_{\phi} \sin\left(\Delta_{\phi}\right) \\ A_{\theta} \sin\left(\Delta_{\theta}\right) \\ A_{\psi} \sin\left(\Delta_{\psi}\right) \end{bmatrix} \tag{7.5}$$

where the phase angles are randomly assigned from a uniform distribution in the interval $[-\pi, \pi]$. Also, the cruise velocity of the carrier is defined as $V_S = 10\, m/s$.

The initial conditions of the aircraft dynamics are selected from a uniform distribution of random numbers, too. The initial value of each state is calculated as

$$x_i = x_0 + \mathcal{U}(-l, l) \tag{7.6}$$

where x_0 is the mean of the uniform distribution and indicates the steady-state value of the corresponding state. $\mathcal{U}(-l, l)$ indicates a uniform distribution in the interval $[-l, l]$. l is chosen as $0.01\, m/s$, $0.01\, deg$, $0.01\, deg$, $0.1\, deg$, $0.01\, deg$, $0.01\, deg$, $0.1\, deg/s$, $0.1\, deg/s$, $0.1\, deg/s$, 0.01, $0.1\, deg$, $0.1\, deg$, $0.1\, deg$ for V, χ, γ, ϕ, α, β, p, q, r, δ_t, δ_e, δ_a, δ_r, respectively.

The initial inertial position of the aircraft is defined with respect to the reference point. The initial position of the reference point is chosen as $(\boldsymbol{x}_{1c})_i = \begin{bmatrix} d_{ci} & \lambda_{ci} & \eta_{ci} \end{bmatrix}^T = \begin{bmatrix} 1500 & 4\pi/180 & \pi + \psi_{D_i} \end{bmatrix}^T$. From Equation 4.7, we have

$$(\boldsymbol{x}_{5c})_i = \begin{bmatrix} d_{ci} \cos\lambda_{ci} \cos\eta_{ci} \\ d_{ci} \cos\lambda_{ci} \sin\eta_{ci} \\ -d_{ci} \sin\lambda_{ci} \end{bmatrix} \tag{7.7}$$

The location of the aircraft is given by a uniform distribution around the location of the reference point as

$$\boldsymbol{x}_{5i} = (\boldsymbol{x}_{5c})_i + \begin{bmatrix} \mathcal{U}_1(-5,5) & \mathcal{U}_2(-5,5) & \mathcal{U}_3(-5,5) \end{bmatrix}^T \tag{7.8}$$

Note that for $\left(\boldsymbol{r}^I_{ID}\right)_i = 0$, we have $\left(\boldsymbol{r}^I_{IA}\right)_i = \boldsymbol{x}_{5i}$.

7.1 Deck Motion Estimation

The performance of the estimation algorithm is critical for the success of the carrier landing task. The deck motion estimation performance at sea-state 6 for a convergence criterion of $\varepsilon = 10^{-7}$ is given in Figures 7.3-7.5 for a single simulation. The initial conditions are randomly assigned and given as

$$\begin{gathered}
\phi_{Si} = -0.0247\,rad,\ \theta_{Si} = 0.0029\,rad,\ \psi_{Si} = -0.0044\,rad \\
(\boldsymbol{r}^I_{IS})_i = \begin{bmatrix} 68.0729 & 3.1933 & 19.7203 \end{bmatrix}^T m \\
\boldsymbol{x}_{5i} = \begin{bmatrix} -1476.7 & 240.47 & -102.48 \end{bmatrix}^T m \\
V_i = 37.9527\,m/s,\ \chi_i = -1.27 \times 10^{-4}\,rad,\ \gamma_i = -0.0522\,rad \\
\phi_i = 8.60 \times 10^{-4}\,rad,\ \alpha_i = 0.1570\,rad,\ \beta_i = -8.21 \times 10^{-5}\,rad \\
p_i = -0.0015\,rad/s,\ q_i = -0.0016\,rad/s,\ r_i = 0.0012\,rad/s \\
\delta_{ti} = 0.2233,\ \delta_{ei} = -0.1812\,rad \\
\delta_{ai} = -3.80 \times 10^{-4}\,rad,\ \delta_{ri} = -1.66 \times 10^{-4}\,rad
\end{gathered} \tag{7.9}$$

It is observed that the NLS estimation lacks precision when the distance between the aircraft and the desired touchdown point is large. However, as the distance gets smaller the estimated values approach the true values allowing for a successful landing. The maximum position and attitude estimation errors ($|True - Estimated|$) are observed at the beginning of the simulation and are calculated as $14.81\,m$, $2.11\,m$, $0.28\,m$, $0.37\,deg$, $0.36\,deg$, $0.081\,deg$ for $(\boldsymbol{r}^I_{ID})_x$, $(\boldsymbol{r}^I_{ID})_y$, $(\boldsymbol{r}^I_{ID})_z$ and ϕ_D, θ_D, ψ_D, respectively. Remember, the sensitivity of the guidance and control system is inversely proportional to the distance between the aircraft and the desired touchdown point, which helps mitigate the negative effects of estimation errors in the long-range.

The initial conditions for the estimated inertial velocities are all chosen as zero since the true values are unknown. In Figure 7.5, the estimation overshoots the true value at the beginning of the simulation but quickly converges within the first $50\,m$ of the distance covered. The overshoot can be reduced at the expense of settling time by the adjustment of the low-pass filter parameters, ζ and w_n.

The starting estimates for the states of the observation model are chosen as zero in the NLS algorithm, so we have $\boldsymbol{p}_{ci} = (\boldsymbol{r}^D_{DC})_{ci} = 0$. The number of iterations it takes the NLS algorithm to satisfy a convergence criterion that is given by $\varepsilon = 10^{-7}$ for zero initial conditions is given in Figure 7.6. The algorithm converges in a maximum of twelve iterations in a given distance; thus, it can be considered as a candidate for real-time applications.

A Monte Carlo simulation is performed to characterize the estimation performance further. In this effort, the data is collected from multiple simulations, and the results are presented statistically. Figure 7.7 shows the mean and standard deviation of the estimation errors in the first and second columns of plots, respectively. The data is gathered from 100 simulations of the carrier landing. The non-zero mean of the estimation error points out the bias in the estimation. Although the estimation

bias is concerning at the beginning of the simulations, it diminishes as the aircraft approaches the carrier. The standard deviation follows a similar pattern. It diminishes towards the touchdown for every quantity that is being estimated. It is also observed that the estimation error stems primarily from the process bias. The measurement noise is insignificant in comparison to the estimation bias.

The maximum number of iterations in each time step for 100 carrier landings are plotted in Figure 7.8. It is shown that the number of iterations does not exceed 12, which supports the previous findings of the single simulation; that is, real-time applications are feasible.

7.2 Autonomous Carrier Landing System Performance

In this section, the time histories of the states and other quantities that are of importance to the successful landing are presented. Also, similar to the previous section, a Monte Carlo simulation approach is used to evaluate the boarding rate and landing dispersion.

7.2.1 Single Simulation Time Histories

The results from a single simulation are presented to evaluate the overall system performance at sea state 6. The same initial conditions that are given in Equation 7.9 are used.

The performance of the reference trajectory generation and guidance is depicted in Figures 7.9 and 7.10. The time histories show that the aircraft successfully follows the reference trajectory throughout the simulation. The longitudinal and lateral landing errors are calculated as

$$e_{long} = -1.3294\ m, \quad e_{lat} = -1.4323\ m$$

which are well within the limits for a successful landing.

The range dependent sensitivity of the angle-based guidance law (discussed in Section 4.3, Figure 4.2) is apparent from the time histories of elevation and azimuth angles. Notice the actual values of these variables change drastically right before the touchdown. The flight-path commands caused by these drastic changes can be found in Figure 7.12. Thanks to the gradual substitution of the angle-based guidance law with position-based law, these abrupt commands are not in effect. It is also shown in Figure 7.12 that angle-based guidance law is superior to the position-based in the long-range because it generates a smoother flight-path command.

The tracking performance of the system is given in Figure 7.11. Remember, γ tracking is regarded as the most challenging task for the aircraft, and it is most closely related to the longitudinal landing error. Therefore, the controller is designed to track the flight-path angle precisely. In Figure 7.11, flight-path and course angle tracking is characterized by a delay. A potential cause of this delay is the control saturation. Figures 7.15 and 7.16 indicate that neither position nor rate saturation occurs expect for the throttle rate only in the first 0.2 seconds of the simulation. Therefore, the phase shift between the commanded and the actual signals cannot be associated with the control saturation. It is introduced by the aerodynamic capabilities and inertia of the aircraft. Hence, the tracking performance is affected by not only the performance of the LQI controller but also the aerodynamic characteristics of the aircraft. Increased longitudinal maneuverability (governed by $C_{L\alpha}$) and elevator control power (governed by $C_{m\delta_e}$) could potentially decrease the delay and improve γ tracking performance.

The velocity of the aircraft varies within a narrow band ($\pm 0.5\, m/s$) around the reference velocity, $V_{ref} = V_0 = 37.9523\, m/s$. Notice the resemblance of the angle of attack and the velocity wave forms. It is safe to assume that the variations in

velocity are introduced by changes in the angle of attack, which is mainly caused by flight-path angle tracking.

The course angle command is generated to correct the azimuth angle with respect to the glide path or y-axis position with respect to the reference point depending on which guidance law is in effect. No steady-state course angle value is provided to the controller. Thus, it would be expected to have $\chi_c = \psi_D$ for a stationary runway and zero sideslip angle. The forward velocity of the carrier leads to a reference trajectory such that the desired touchdown point is intercepted at a location further down along the estimated path of the desired touchdown point. Also, the estimated interception point, the estimated desired touchdown point, and the reference point are noncollinear on the xy-plane of the inertial frame because of the angled runway. These two factors cause the commanded course angle to be slightly lower than the runway's heading angle in absolute value. The fact that reference trajectory is generated such that the velocity vector is directed towards an estimated interception location rather than the desired touchdown point itself also causes the difference between the flight-path angle and the elevation angle. For a stationary runway, we would expect $|\gamma_c| = |\lambda_c|$.

The performance of the inner-loop control is evident from Figures 7.13 and 7.14. The states of the aircraft are regulated to the steady state. The control input commands from the outer, tracking loop cause oscillations about the steady state. Nevertheless, these oscillations are small enough that one operating point suffices, and gain scheduling is not necessary for this study.

The time histories of the commanded and actual control inputs are given in Figure 7.15. The most aggressive control action is associated with the elevator since the elevator deflection is the most effective means to track the flight-path angle, which is prioritized in the design of the guidance and control system. It is observed

that the gradual switch of the controller and guidance law makes the elevator more sensitive with closing distance as intended. The lateral-directional control actions are kept minimal intentionally to ensure the elevator effectiveness is preserved, and flight-path tracking performance is not degraded by unnecessary expectations of the lateral landing performance.

7.2.2 A Monte Carlo Approach

In this section, the performance of the system is evaluated using a Monte Carlo approach. A wide range of initial conditions that are described by Equations 7.4-7.8 are considered.

A thousand carrier landings are simulated at each sea state and the landing dispersion is presented in Figures 7.17-7.20. Figure 7.17 depicts the landing dispersion at sea state 0, where there are no perturbations due to the sea. The motion of the carrier is defined by its constant forward velocity, V_S. It is observed in this simplest case that all touchdowns are concentrated in a tiny region near the desired touchdown point. Both longitudinal and lateral landing errors are lower than the maximum allowable for every simulation.

The landing dispersion at sea state 6 is shown in Figure 7.20. The data is the most scattered in this sea state amongst all the sea states considered in this study. This is expected since sea state 6 is the most vigorous. The aircraft is ideally trapped by the third arresting wire; however, Figure 7.20 shows that the touchdown occurred beyond the third wire in some simulations. These landings are still potentially successful even though not ideal since the aircraft can be trapped by the fourth wire. It can also be seen from the figure that landing errors are below the maximum allowable limits for all the simulations performed even for the most challenging case.

Figures 7.18 and 7.19 depict the system performance for the intermediate sea states 4 and 5. It is evident from these figures that the landing errors are below maximum allowable limits for sea states 4 and 5, too.

We see from Figure 7.15 that the lateral-directional control surfaces are more stagnant than the elevator. We also mentioned in Section 7.2.1 that the lateral-directional control action may introduce instability in the longitudinal plane and decrease elevator effectiveness; hence, degrade γ tracking performance. Keeping this in mind, it is also evident from Figures 7.17-7.20 that the impact of the sea state is more prominent in the longitudinal axis. Therefore, the lateral landing dispersion at lower sea states can only be improved at the expense of longitudinal landing dispersion at higher sea states. The lateral landing performance could have been improved easily by assigning more aggressive control action to the aileron and the rudder; yet, it is avoided to satisfy the most critical and fragile requirement of the carrier landing, i.e., longitudinal landing dispersion.

The effect of the perturbations caused by the sea states on landing dispersion is analysed in Table 7.1. In this table, the mean, standard deviation and maximum deviation from the desired value are given for longitudinal landing error, lateral landing error and the relative Euler angles between the aircraft and runway at touchdown. From the table, we can conclude that the means of the longitudinal and lateral landing errors are not strongly affected by the sea state. The mean of the longitudinal error is positive, which means the aircraft tends to get past the desired touchdown point. This behaviour may stem from the bias in the estimation of the vertical component of the inertial position of the desired touchdown point. In Figure 7.7, it is observed that the NLS algorithm tends to underestimate this quantity; i.e., the estimated position of the desired touchdown point is higher in altitude.

A correlation between the standard deviation and sea state is observed. The larger the perturbations are the more scattered the data is. It is also observed that the mean of the landing error is correlated with the beacon locations. Keeping the center of the beacons closer to the desired touchdown improves estimation bias near touchdown and decreases the mean of the landing dispersion. Nonetheless, the beacon configuration is not rearranged due to the concerns regarding the field-of-view of the camera and visibility of the beacons for the entirety of the landing.

Table 7.1. Landing statistics

		Sea State			
		0	4	5	6
Longitudinal Error (m)	μ	0.6269	0.8238	0.8572	1.1711
	σ	0.0157	1.3087	2.0184	3.1891
	$max(\lvert x - x_d \rvert)$	0.6562	3.5973	5.7678	9.3561
Lateral Error (m)	μ	-0.3216	-0.3170	-0.2930	-0.3810
	σ	0.2088	0.4884	0.8586	1.0969
	$max(\lvert x - x_d \rvert)$	0.7154	1.6290	2.5166	2.9731
ϕ_{AD} (deg)	μ	-0.0433	-0.0387	0.0615	0.0439
	σ	0.0237	0.6426	1.0773	1.4225
	$max(\lvert x - x_d \rvert)$	0.0880	1.4864	2.6535	3.5129
θ_{AD} (deg)	μ	6.0187	6.0062	5.9918	5.9830
	σ	0.0006	0.4601	0.7226	1.0956
	$max(\lvert x - x_d \rvert)$	0.0201	1.0065	1.6245	2.4089
ψ_{AD} (deg)	μ	2.3770	2.3851	2.3417	2.3925
	σ	0.0255	0.3555	0.7393	0.9620
	$max(\lvert x - x_d \rvert)$	2.4251	3.1831	3.9050	4.3883
$(\dot{\boldsymbol{r}}^D_{AD})_z$ (m/s)	μ	1.9712	1.9600	1.9713	1.9585
	σ	0.0000	0.1807	0.2720	0.4085
	$max(\lvert x - x_d \rvert)$	1.9712	2.2713	2.4457	2.6752

The fact that the criterion for landing dispersion is satisfied is a necessary but not sufficient condition for a successful landing. We must also ensure that the relative Euler angles between the aircraft and runway at touchdown are within the

limits. It is evident from Table 7.1 that the controller successfully aligns the aircraft with respect to the runway. The mean and the standard deviation of the Euler angles are within the limits. The desired values associated with roll, pitch, and yaw angles are taken as $0\,deg$, $6\,deg$, and $0\,deg$, respectively. Maximum deviations from these desired values are critical for several reasons. First, we want a small roll angle to ensure wings of the aircraft are not in danger of hitting the deck surface. The pitch angle is expected to be positive to avoid hitting the nose and not greater than $15\,deg$ for successful hook engagement, ideally 5 to $6\,deg$. The yaw angle is ideally zero for optimal horizontal alignment. Notice that the mean of the yaw angle is introduced because of the difference between χ_c and ψ_D, which caused by the noncollinearity of the estimated locations of the interception, desired touchdown and reference points (see Section 7.2.1).

The component of the impact velocity that is perpendicular to the deck surface is denoted as $(\dot{\boldsymbol{r}}^D_{AD})_z$. It is derived in Equation 2.6, and in Section 2.5, the upper limit for this quantity is designated $3\,m/s$. In Table 7.1, it is shown that the maximum value achieved in the Monte Carlo simulations is $2.6752\,m/s$; thus, impact velocity is within the limits for all simulations.

7.2.2.1 Estimation Sampling Rate

The effects of the sampling rate of the PSD on the landing performance are investigated. In the previous section, a sampling rate of $100\,Hz$ is used both for the PSD measurements and the measurements of the aircraft states for feedback control. In this section, sampling rates of $5\,Hz$, $10\,Hz$, $50\,Hz$, and $100\,Hz$ are considered for the PSD.

Figures 7.21-7.24 show the effect of the PSD sampling rate on the landing performance. A thousand carrier landing simulations are performed for each combination

of the sea state and sampling rate. In these figures, the landing region, which is the smallest rectangle that encloses all the touchdown points, is drawn for each sampling rate.

The effect of the sampling rate on the mean longitudinal error is noticeable but insignificant. The behaviour is most clearly evident at sea state 0 in Figure 7.21. The desired touchdown location is estimated with each measurement of the PSD. Between successive samples, the estimated location stays constant. Hence, the aircraft navigates using the most recent measurement of the PSD. The motion of the carrier between the successive measurements introduces a landing error since the aircraft is not aware of the current desired touchdown location at touchdown. For this reason, as the sampling rate decreases the landing region shifts aft. This shift in the landing region may mistakenly be considered as an improvement since the mean longitudinal landing error is already positive at a sampling rate of $100\,Hz$ due to the biased estimation.

The sampling rate of the PSD has almost no effect on the standard deviation of the longitudinal and lateral landing errors.

Sampling rates below $5\,Hz$ cause instabilities in the system and must be avoided. In his study, in 1999, Junkins et. al. [45] stated that a beacon's line-of-sight vector can be determined accurately by a PSD with an update rate of $50\,Hz$. Therefore, a sampling rate below $5\,Hz$ is not a concern for vision-based systems relying on the PSD technology.

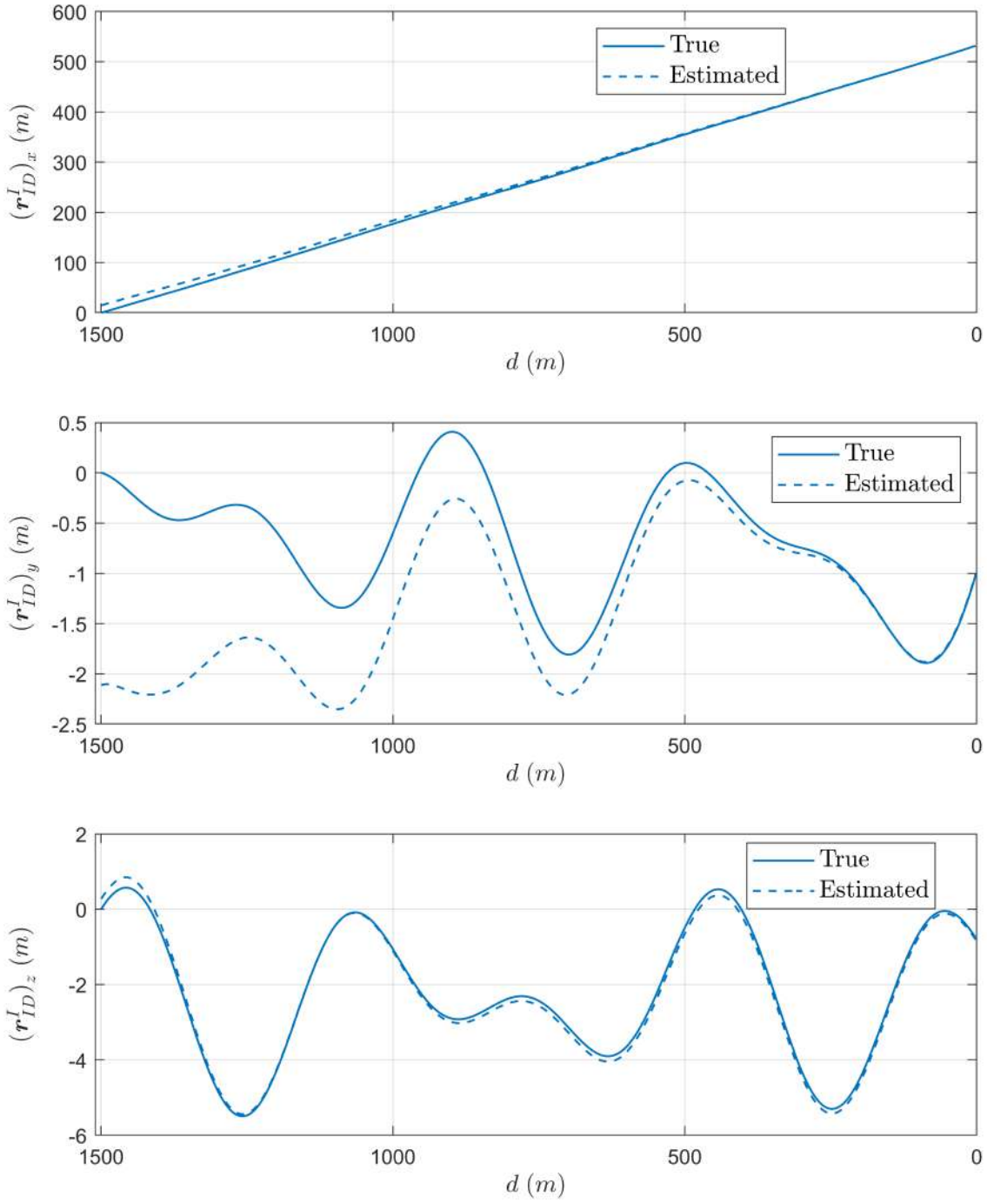

Figure 7.3. Estimation of the inertial position of the desired touchdown point.

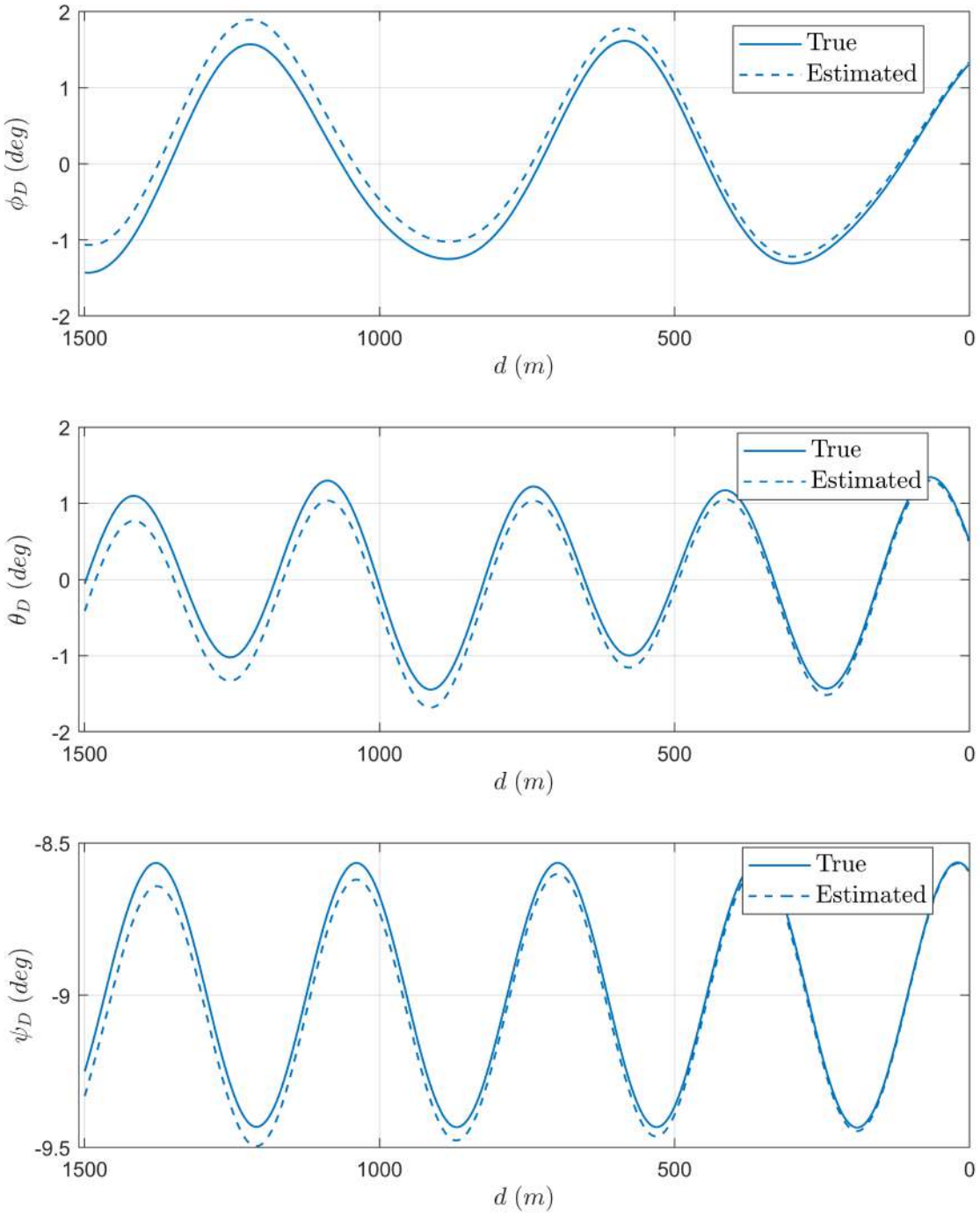

Figure 7.4. Estimation of the attitude of the runway with respect to inertial frame.

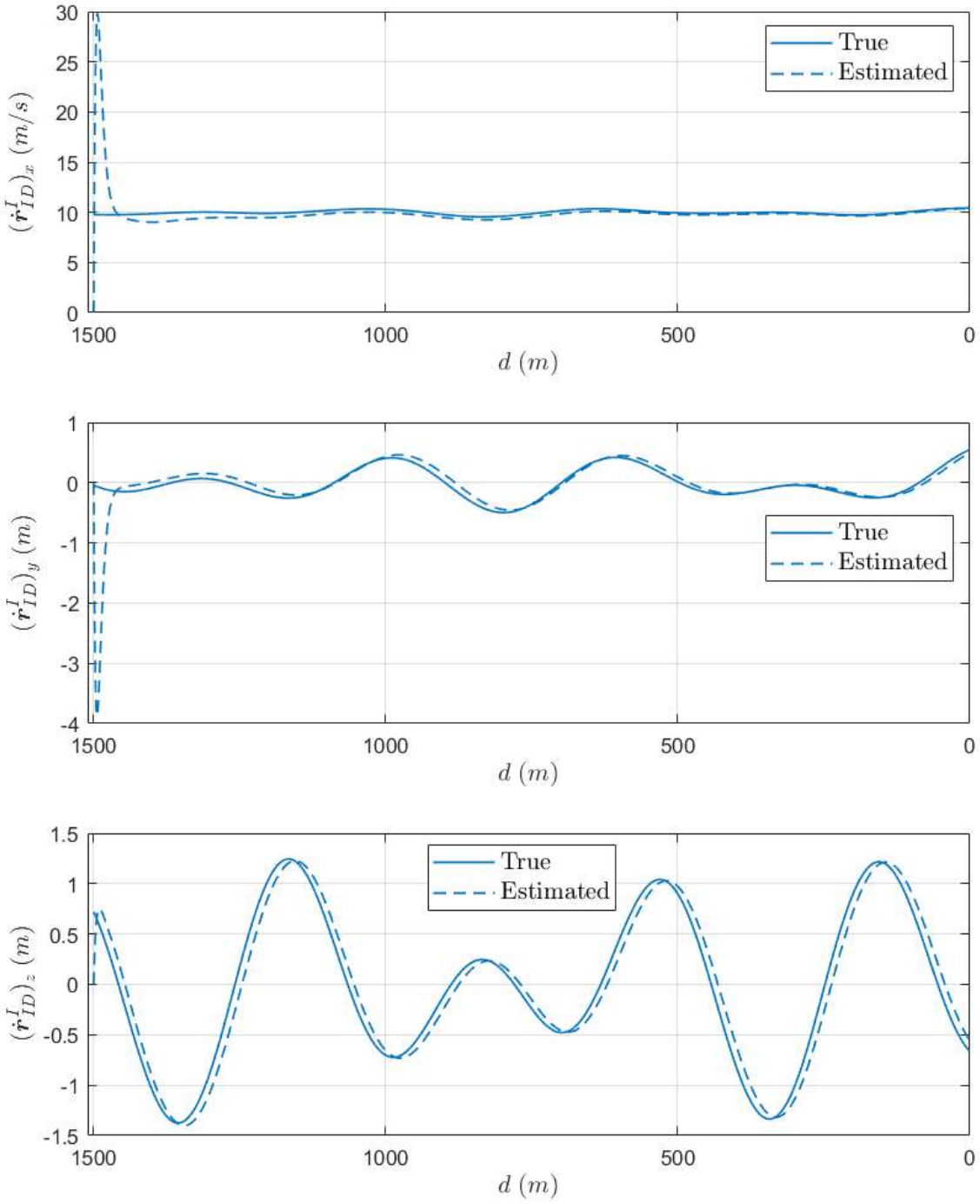

Figure 7.5. Estimation of the inertial velocity of the desired touchdown point.

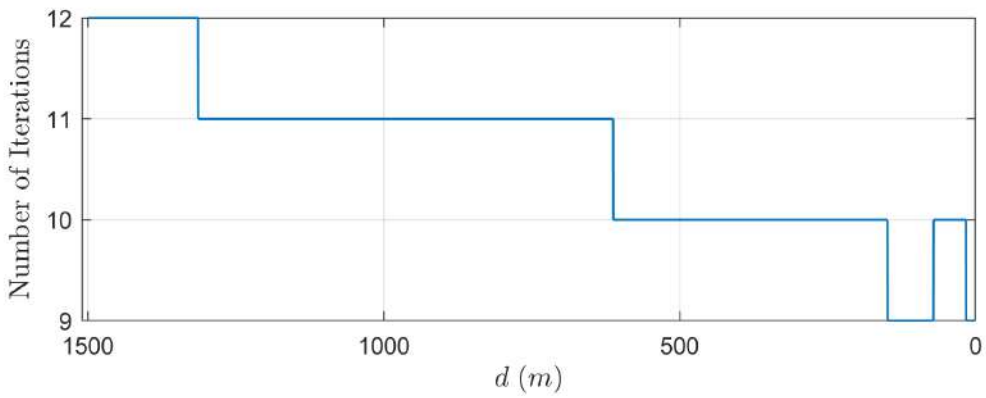

Figure 7.6. Number of iterations for $\varepsilon = 10^{-7}$.

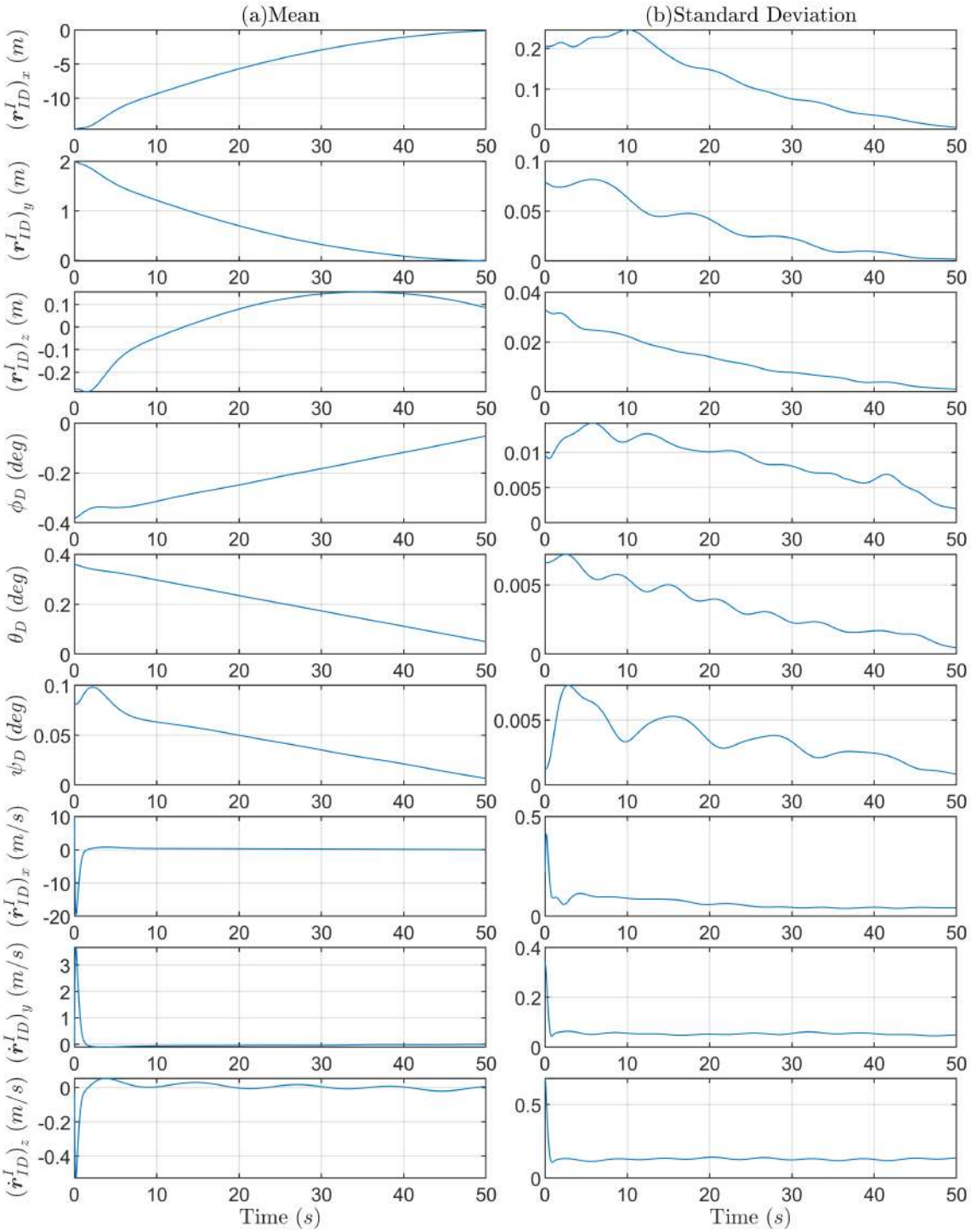

Figure 7.7. (a) The mean and (b) the standard deviation of the deck motion estimation error calculated from 100 carrier landing simulations.

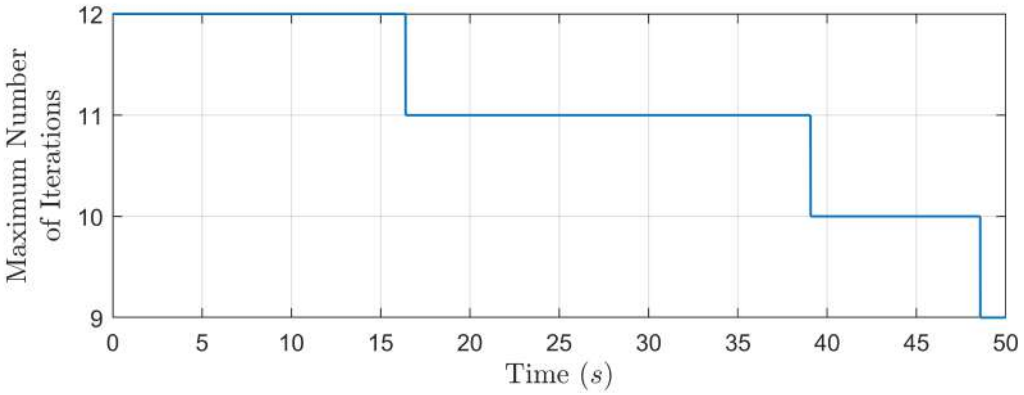

Figure 7.8. The maximum number of iterations in each time step for 100 carrier landings.

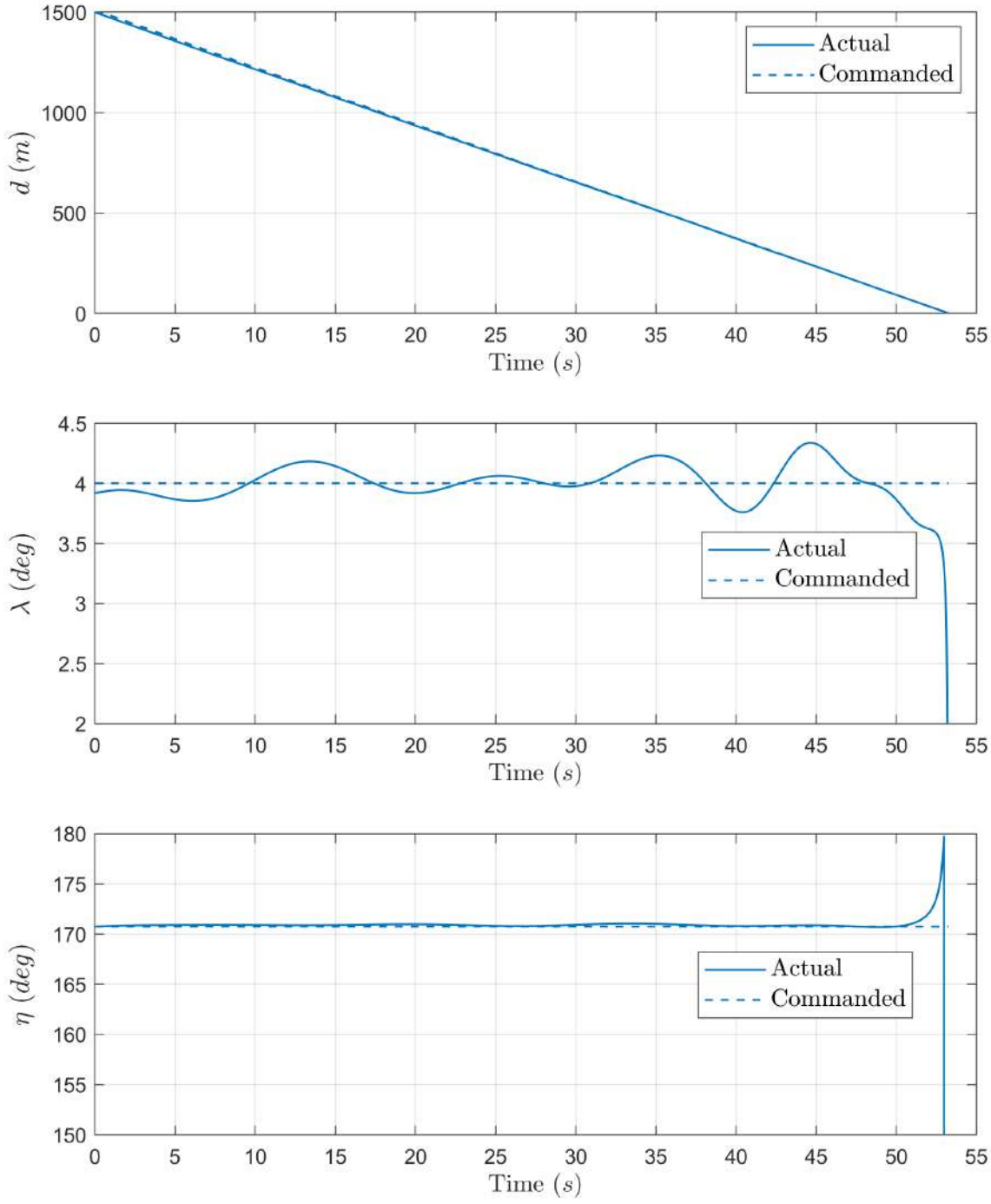

Figure 7.9. Time histories of components of $\boldsymbol{x}_1$; distance (d), elevation angle(λ) and azimuth angle(η) at sea state 6.

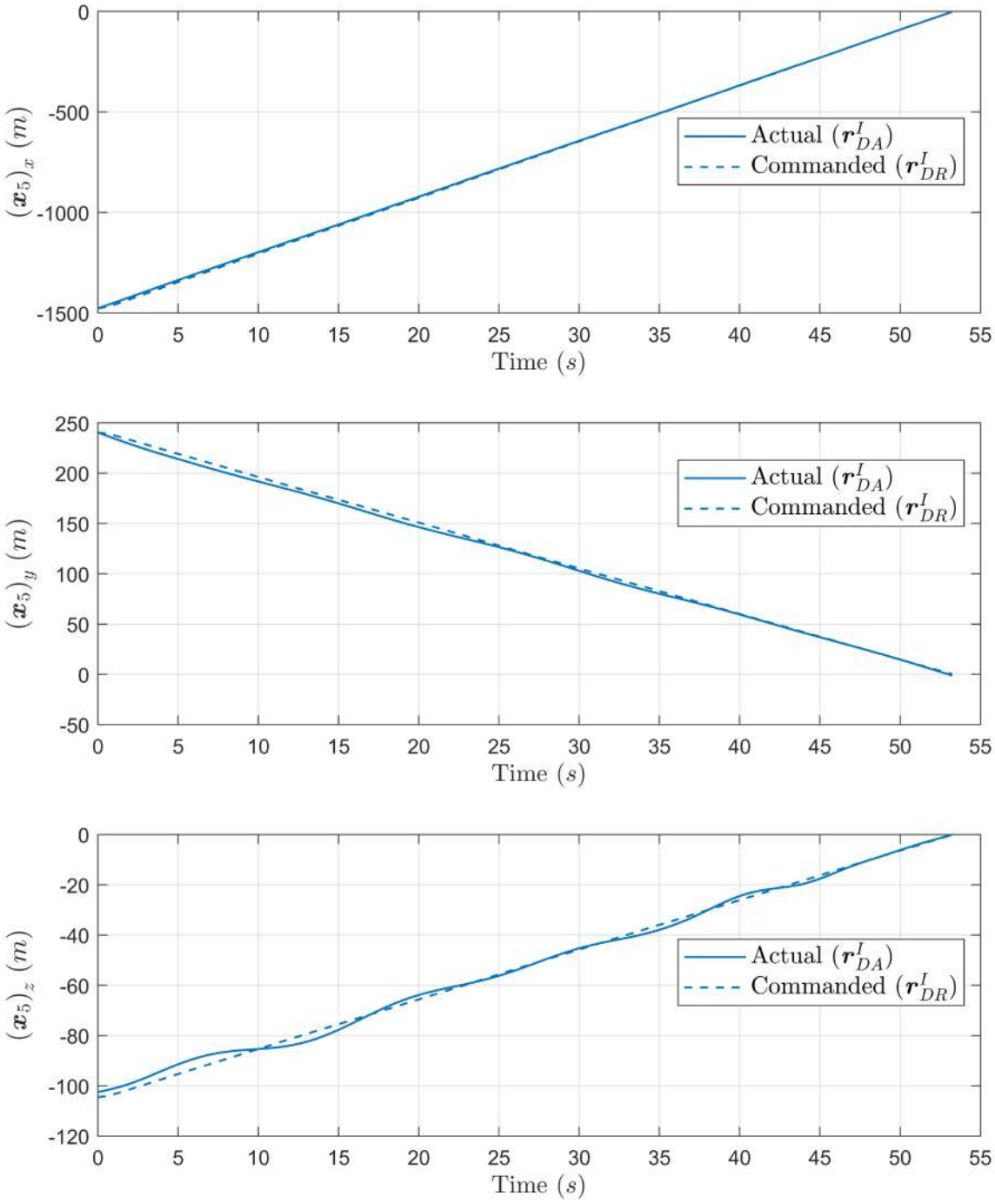

Figure 7.10. Time histories of components of $\boldsymbol{x}_5$; longitudinal ($(\boldsymbol{x}_5)_x$), lateral ($(\boldsymbol{x}_5)_y$) and vertical($(\boldsymbol{x}_5)_z$) at sea state 6.

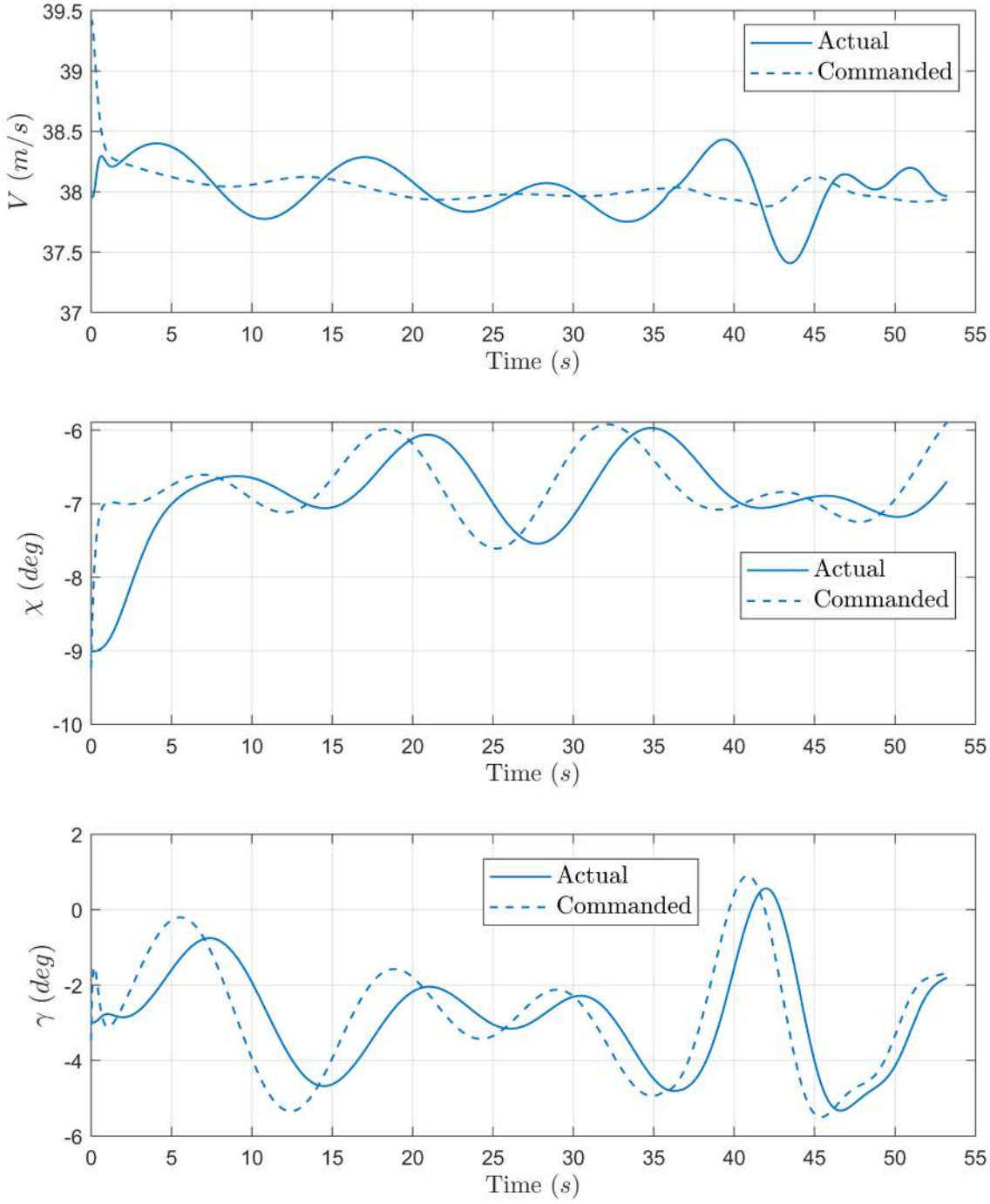

Figure 7.11. Time histories of components of $\boldsymbol{x}_2$; velocity (V), course angle (χ) and flight-path angle (γ) at sea state 6.

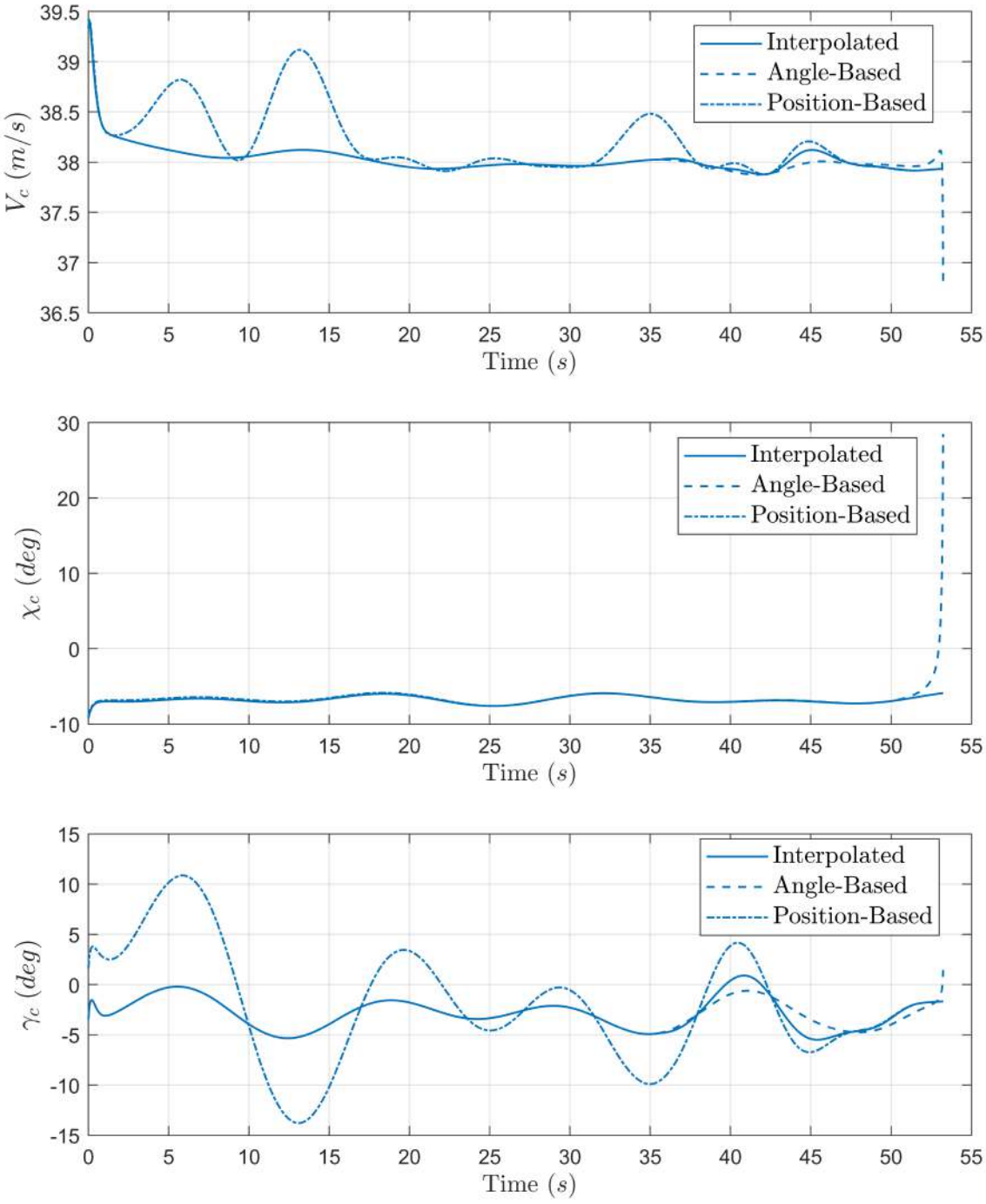

Figure 7.12. Time histories of flight-path commands generated by angle-based and position-based guidance laws at sea state 6.

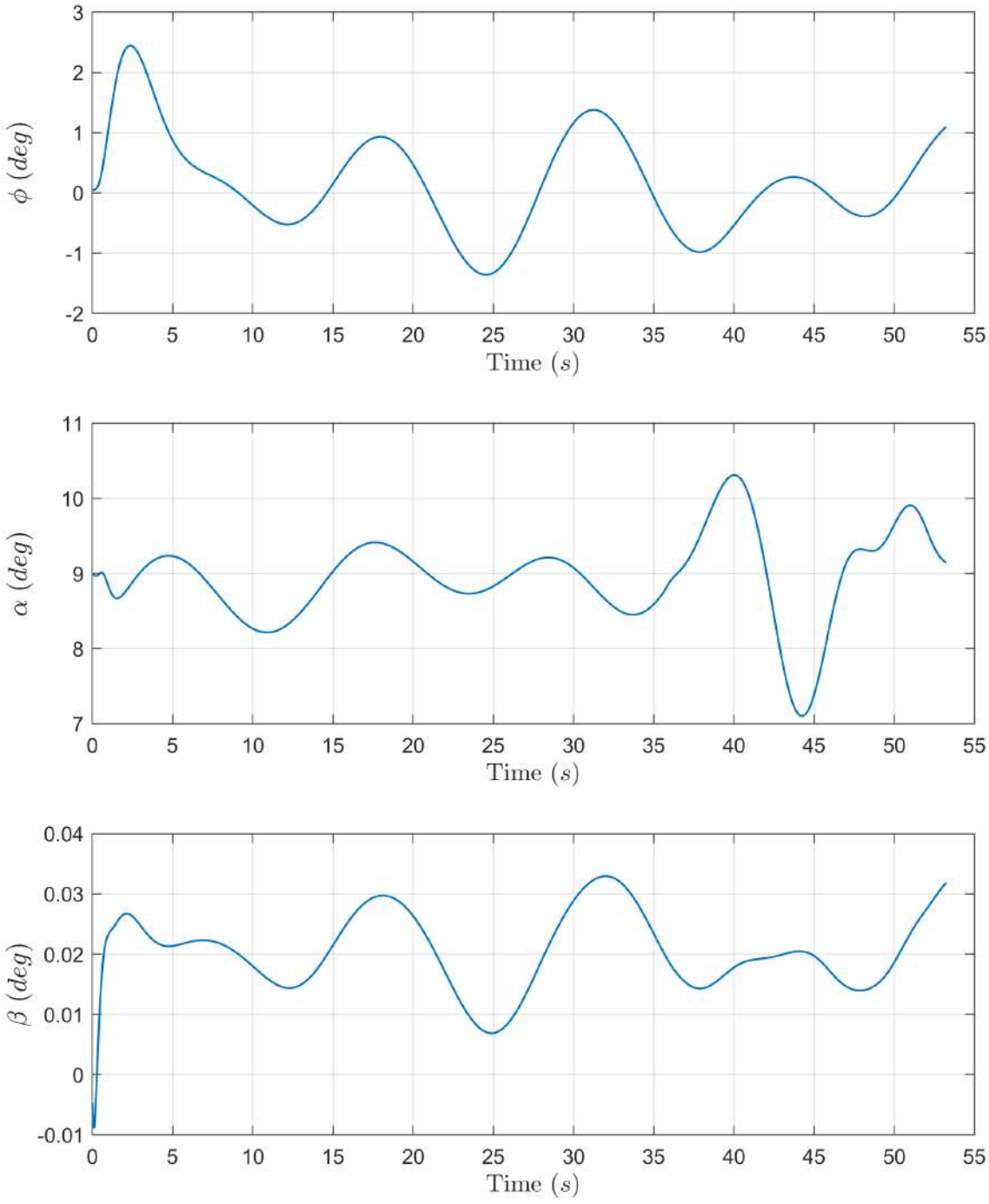

Figure 7.13. Time histories of components of $\boldsymbol{x}_3$; roll angle (ϕ), angle of attack (α) and sideslip angle (β) at sea state 6.

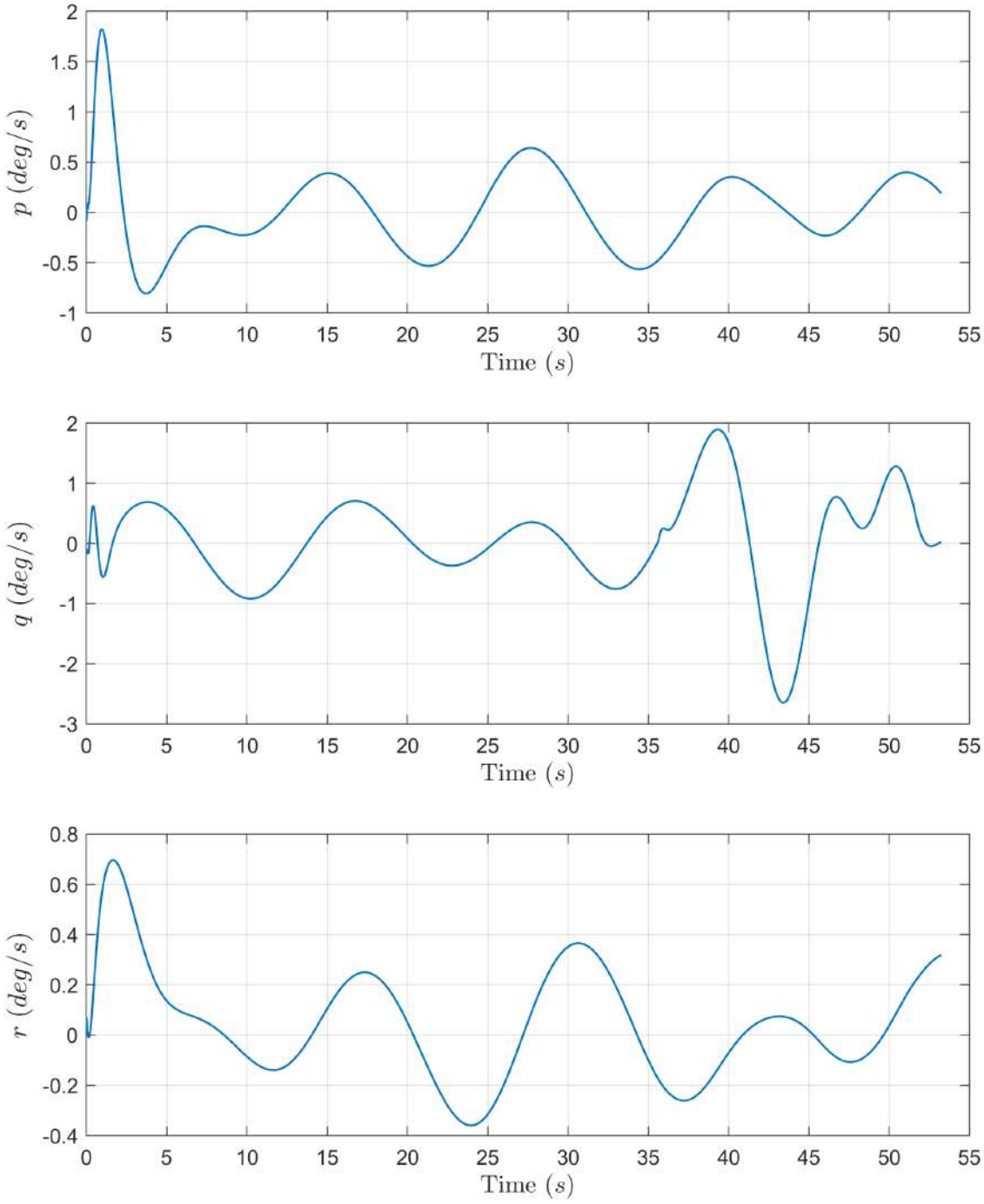

Figure 7.14. Time histories of components of $\boldsymbol{x}_4$; angular velocities about body-fixed axes, p, q and r at sea state 6.

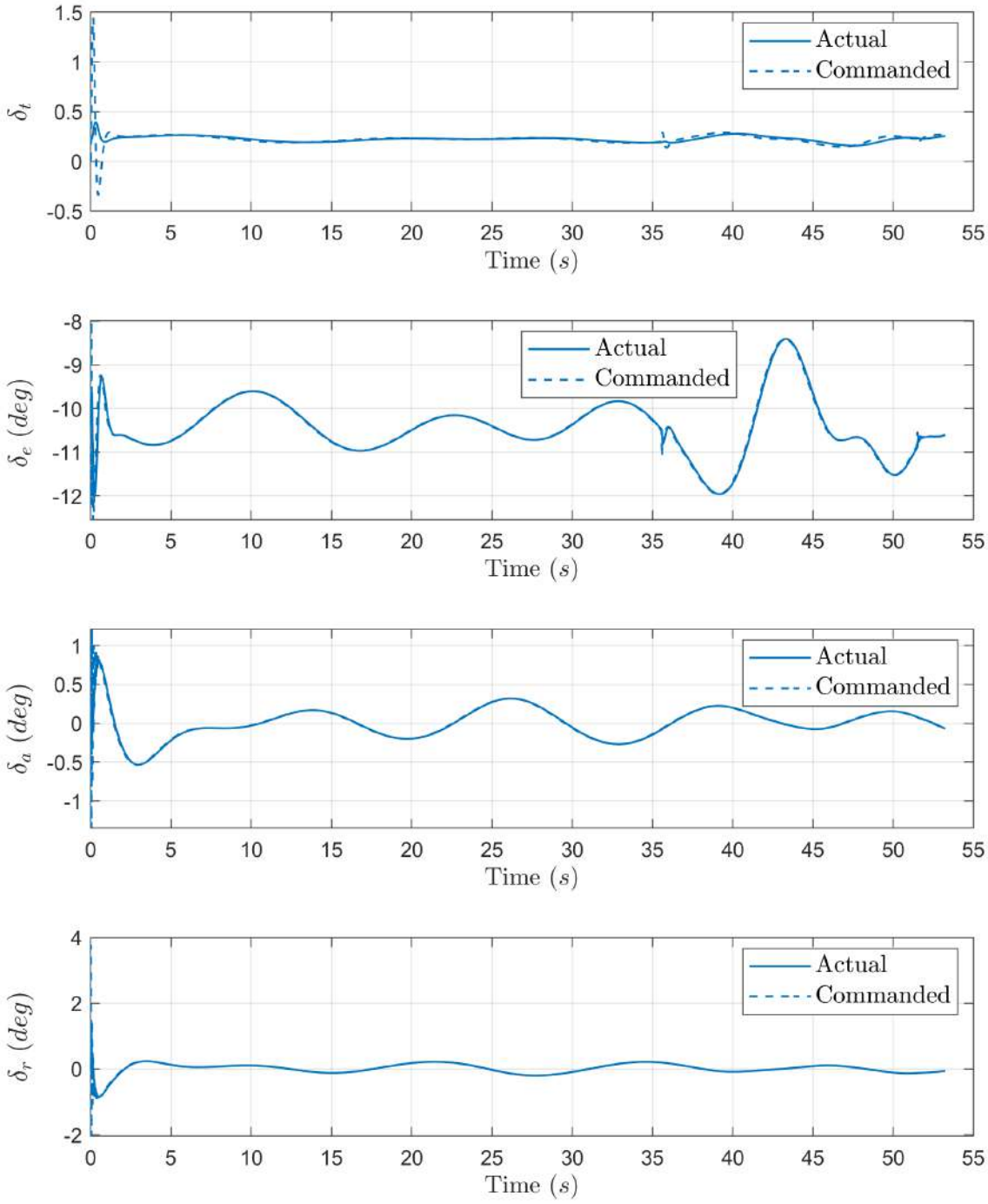

Figure 7.15. Time histories of components of $\boldsymbol{\delta}$; throttle (δ_t), elevator deflection (δ_e), aileron deflection (δ_a) and rudder deflection (δ_r) at sea state 6.

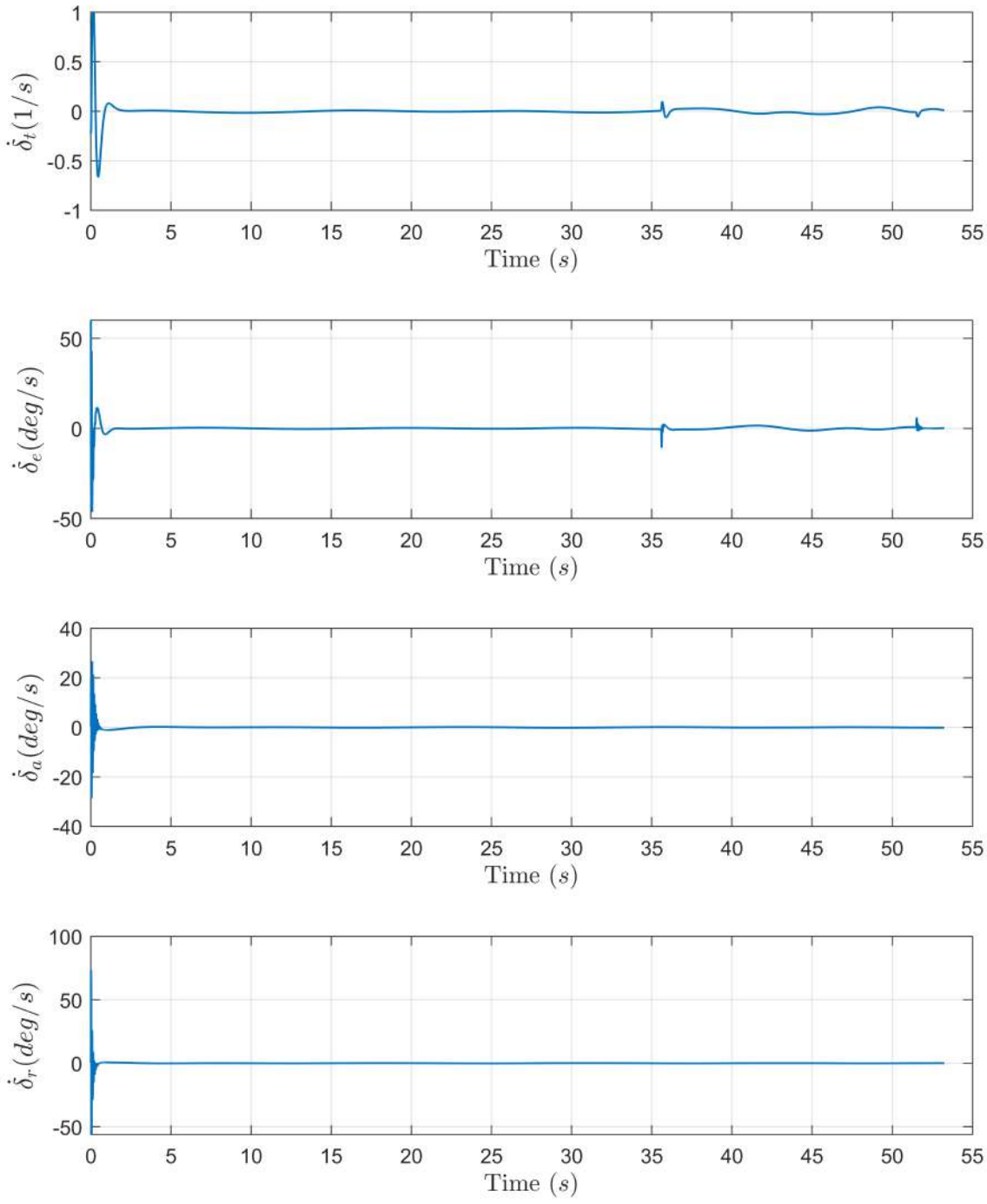

Figure 7.16. Time histories of components of $\dot{\boldsymbol{\delta}}$; throttle rate($\dot{\delta}_t$), elevator deflection rate ($\dot{\delta}_e$), aileron deflection rate ($\dot{\delta}_a$) and rudder deflection rate ($\dot{\delta}_r$) at sea state 6.

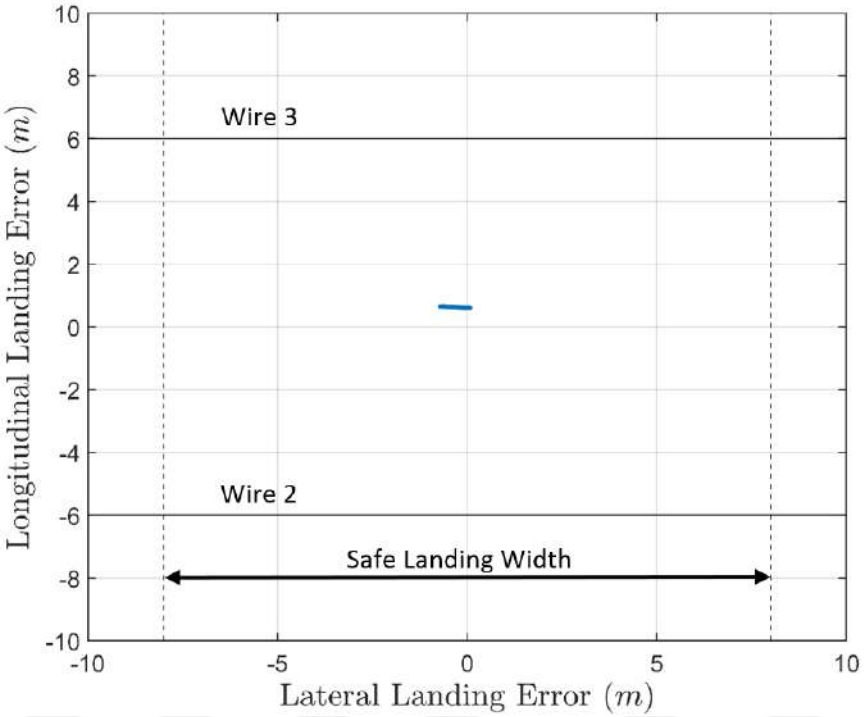

Figure 7.17. Landing dispersion at sea state 0.

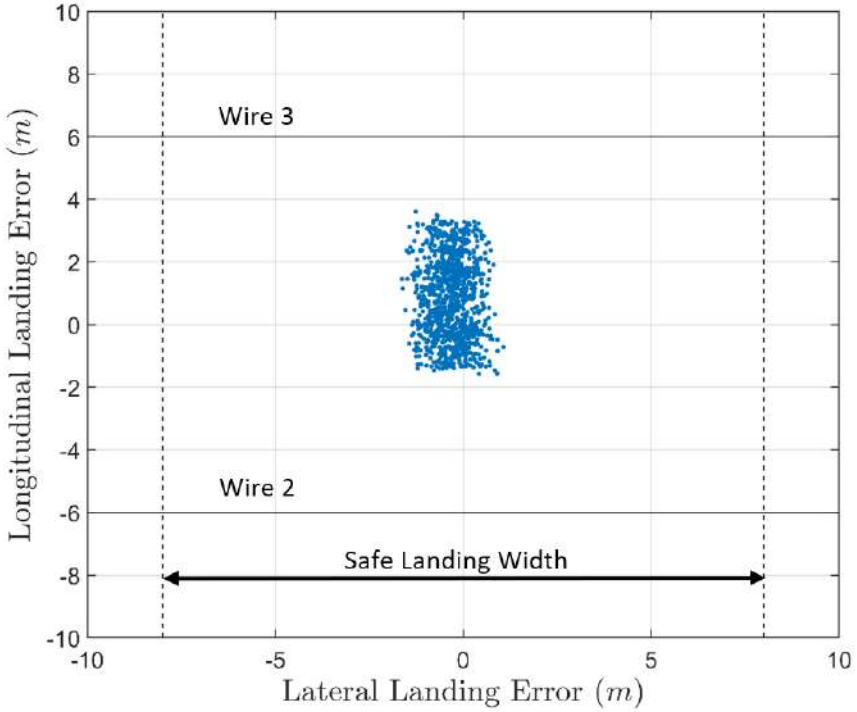

Figure 7.18. Landing dispersion at sea state 4.

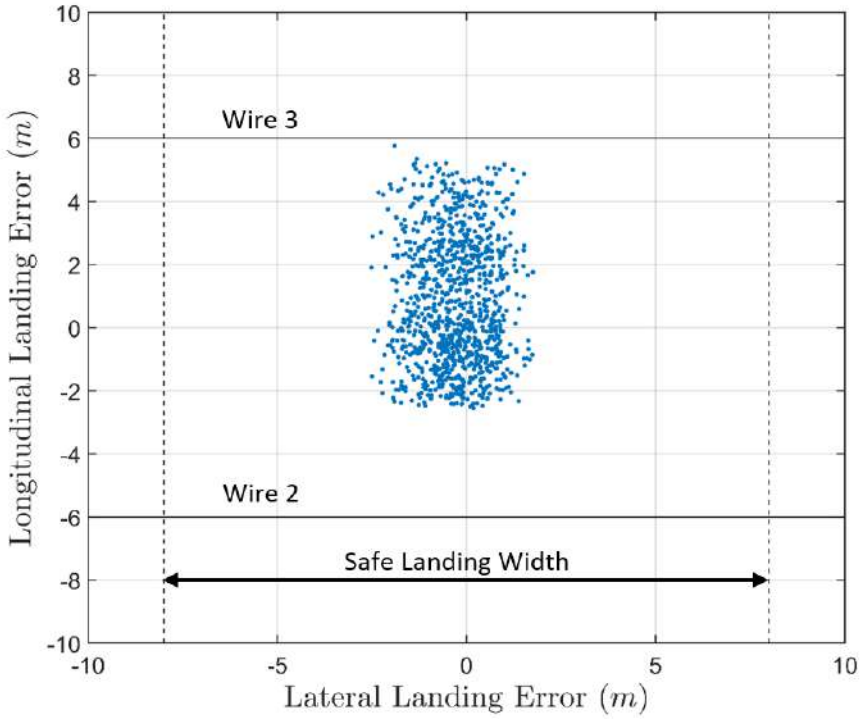

Figure 7.19. Landing dispersion at sea state 5.

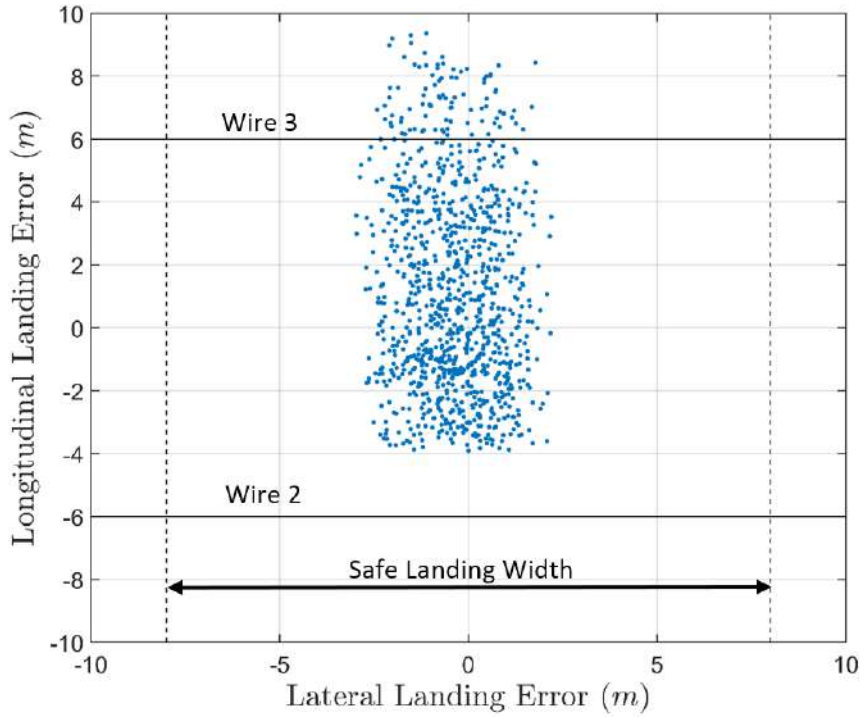

Figure 7.20. Landing dispersion at sea state 6.

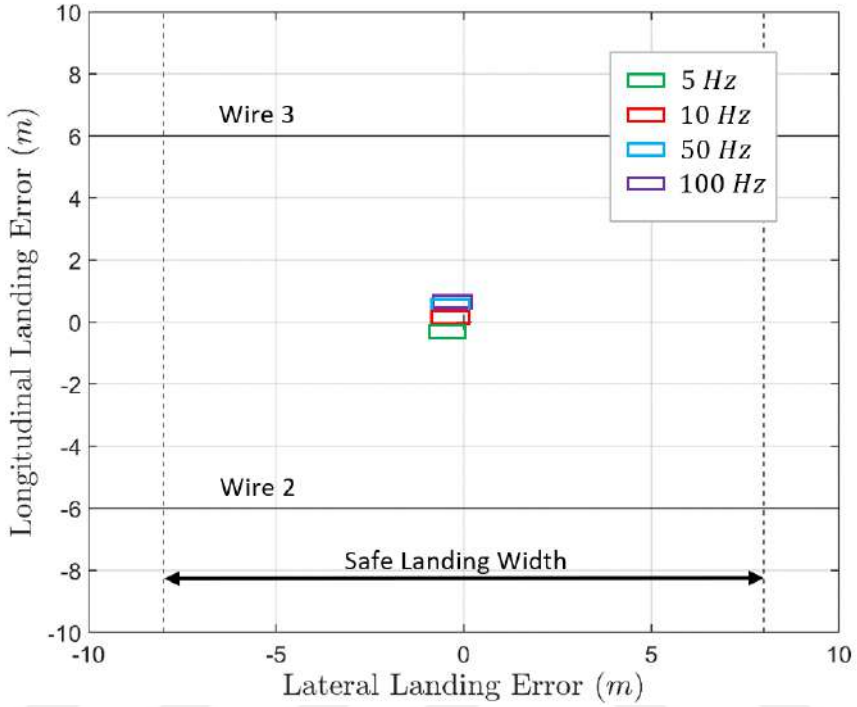

Figure 7.21. Landing region at sea state 0 for various PSD sampling rates.

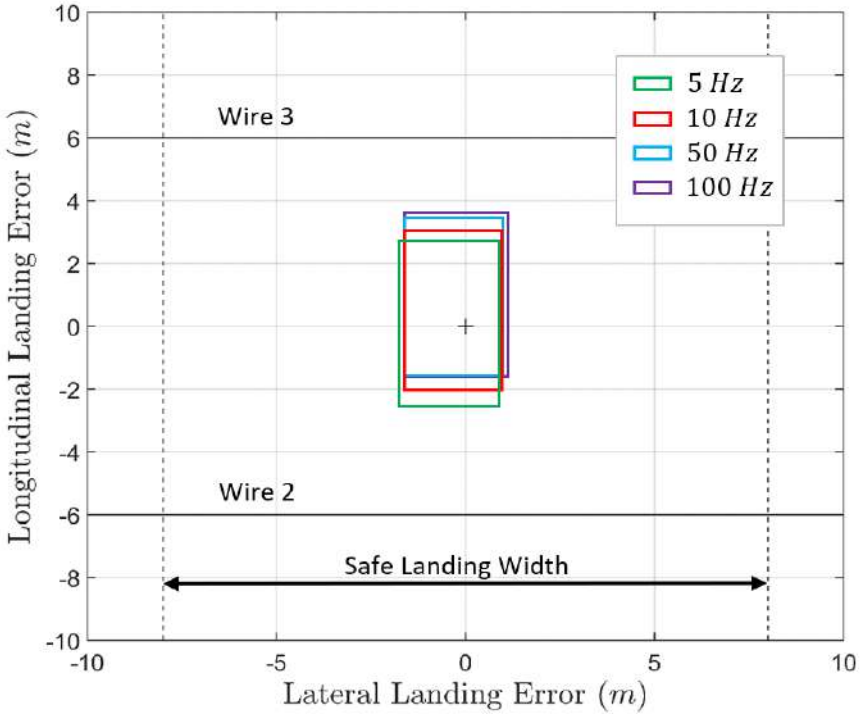

Figure 7.22. Landing region at sea state 4 for various PSD sampling rates.

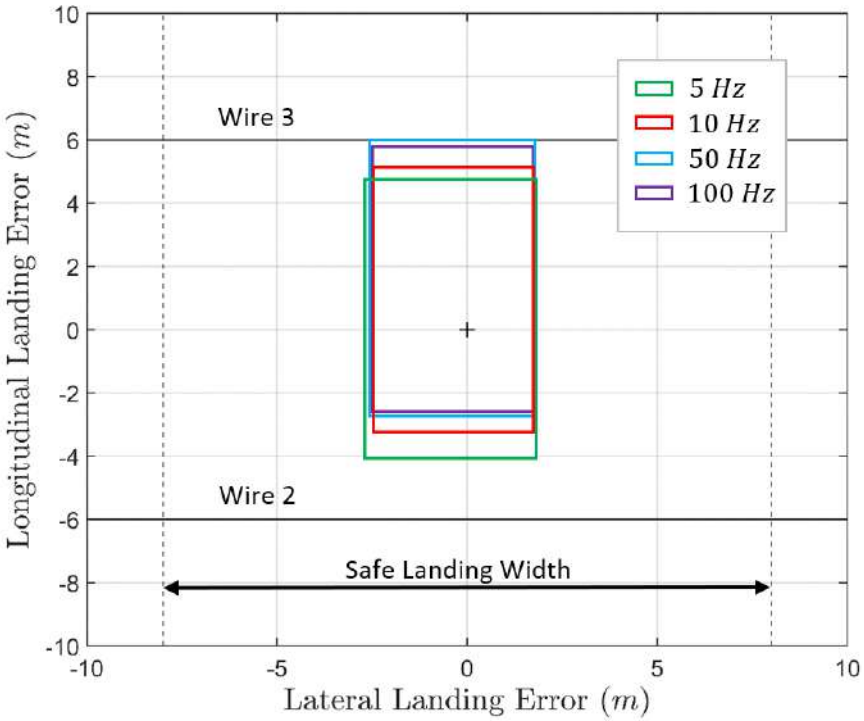

Figure 7.23. Landing region at sea state 5 for various PSD sampling rates.

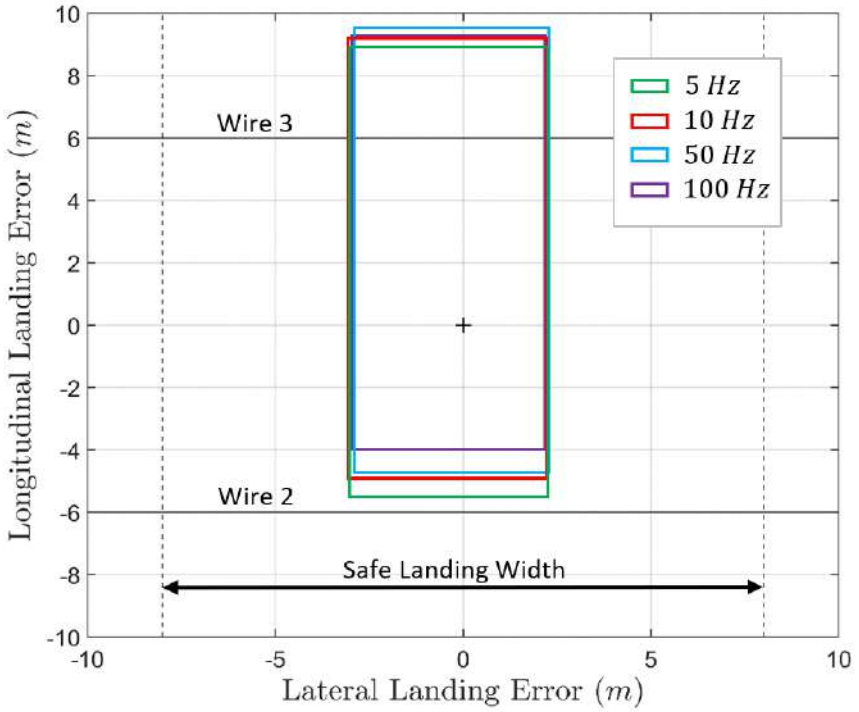

Figure 7.24. Landing region at sea state 6 for various PSD sampling rates.

CHAPTER 8

CONCLUDING REMARKS AND FUTURE WORK

The objective of this study was to design and implement an autonomous carrier landing system for a fixed-wing UAV. A three-dimensional landing scenario was considered. A ship motion model is built to simulate the carrier dynamics, which account for the forward carrier velocity and perturbations that are introduced by various sea states. These perturbations are defined for each sea state in terms of sinusoidal waves with specific amplitudes and frequencies for both translational and rotational dynamics. The aircraft dynamics are modeled using the flat-Earth assumption describing the motion of the aircraft over a small area of a non-rotating Earth, with constant gravity [16]. The linear aerodynamics of the aircraft at a flight condition is considered instead of multidimensional look-up tables because of the data availability. This assumption is justified since the landing operation is restricted to a tiny region within the flight envelope. The aerodynamic stability derivatives of the SIAI Marchetti S211 aircraft are considered because of its longitudinal maneuverability characteristics. The first-order dynamics of the engine and actuators are taken into account with the position and rate limiters.

The landing kinematics are studied, and a reference trajectory for the aircraft is generated. In this effort, a glide path with constant azimuth and elevation angles is used to express the location of a reference point. The desired dynamics of the reference point are assigned using a reference inertial speed and the dynamics of the desired touchdown point.

The guidance laws are used to generate the flight-path commands that would drive the aircraft towards the reference point. An error signal is formed between the actual trajectory of the aircraft and the reference trajectory. The desired dynamics to this error signal are assigned. A virtual guidance input, which would yield the desired dynamics for the error signal, is calculated using the feedback linearization method. The flight-path command is calculated exploiting the one-to-one correspondence between the inertial velocity and the flight-path command. Two guidance laws are proposed and implemented during the approach and touchdown phases of the landing task. The first guidance law considers the angular error between the reference point and aircraft location; hence, it becomes more sensitive to positional errors as the aircraft approaches the touchdown point. The second guidance law considers the positional error between the reference point and the aircraft, and is proposed to compensate for the oversensitive angle-based guidance law near touchdown. An interpolation scheme based on the estimated distance to the touchdown point is proposed as a way to switch the guidance laws in flight.

A controller is designed based on a linear approximation of the nonlinear plant dynamics. Wings-level descent is considered as the steady-state flight condition in the selection of an equilibrium point at which the plant is linearized. Several hard and soft constraints are applied to the optimization algorithm to find a desirable equilibrium amongst many solutions. These constraints are dictated by several factors, including aerodynamic stall margin and optimal hook engagement. The aircraft dynamics are linearized using MATLAB's linear analysis toolbox, which linearizes the system numerically by perturbing all the states and control inputs one at a time and measuring the system response. The actuator and engine models are also linearized and appended to the aircraft dynamics. A type 1 servo system architecture is used to track the flight-path command that is provided by the guidance laws while regulating

the other states to their steady-state values. The feedback gain matrix is calculated using an LQI optimal controller. An intuitive way to select appropriate $\boldsymbol{Q}$ and $\boldsymbol{R}$ weighting matrices based on the maximum allowable deviations from steady-state values is employed.

The carrier motion is estimated using an autonomous vision-based navigation system. The projections of four coplanar target points on the focal plane of an airborne PSD are used to estimate the position of the desired touchdown point and attitude of the runway. The estimation problem is proposed as a P4P problem, and the solution is found using the NLS algorithm. In this algorithm, corrections to a current estimation are made in successive iterations to minimize the error between the estimated and actual value of the measurement. The inertial velocity of the desired touchdown point is estimated using a second-order, low-pass filter.

The autonomous carrier landing system is successfully designed and implemented in a simulation environment. The single simulation results show satisfactory navigation, guidance, and control performance. The system is further evaluated using a Monte Carlo approach to ensure a wide range of initial conditions is covered. The Monte Carlo simulation results show that the system can successfully land the aircraft on a carrier for all the sea states considered in this study. The effect of the sea state is observed to be most prominent on landing dispersion. The standard deviations regarding longitudinal landing error, lateral landing error, and relative Euler angles between the aircraft and the runway increase significantly with increasing sea state, although the means of the same variables stay more or less constant. The Monte Carlo simulations involve 1000 carrier landing for each sea state, and a 100% boarding rate is achieved.

The impact of the PSD sampling rate on landing performance is also evaluated. A wide range of sampling rates is considered and the system performance is not

significantly affected by the PSD sampling rate as long as it is above $5\,Hz$. Sampling rates below $5\,Hz$ might introduce instability to the system. It is noted that this is not a concerning factor since sampling rates of $50\,Hz$ and above can easily be achieved by the PSDs.

The system proposed in this study achieves the objectives of an autonomous carrier landing within the scope and assumptions of this study. Nevertheless, it can be improved and extended further before it is applied to more realistic scenarios. A gust model and an over-the-deck wind model can be included for this purpose as they are considered to be substantial sources of landing errors in carrier landing operations [7].

Choosing the $\boldsymbol{Q}$ and $\boldsymbol{R}$ weighting matrices is proven to be very challenging in this study. While an intuitive approach was taken, fine adjustments relying on trial and error were still required. The system performance is observed to be very sensitive to these matrices. A more challenging scenario including gust and over-the-deck wind models might require even further adjustments, which might be very time consuming and cumbersome. For this reason, a more systematic method for the selection of $\boldsymbol{Q}$ and $\boldsymbol{R}$ might be necessary.

The results shows that the measurement noise associated with the vision-based sensor is insignificant in comparison to the estimation bias. For future work, the system can be evaluated in the presence of a more significant measurement noise. Another measurement system and algorithm might be needed together with a Kalman filter to combine multiple estimates of multiple navigation systems if the system performance drops below an acceptable level. Furthermore, even though system robustness is shown through a Monte Carlo approach, no mathematical proof of stability is suggested for this system; hence, an algorithm to evaluate the landing risks and to decide whether or not to abort the operation can be proposed as a safety measure.

Also, a backup system that would carry out bolter routines can be included to ensure the aircraft can be recovered safely, even if the wire engagement does not occur.

REFERENCES

[1] Periscope Film LLC. U.S. Navy Aircraft Mishaps & Crashes Training Film. Retrieved from `https://www.youtube.com/watch?v=SPlqoeaPUu4&t=146s`. [Accessed on November 2, 2019].

[2] S. Lee, J. Lee, S. Lee, H. Choi, Y. Kim, S. Kim, and J. Suk. Sliding Mode Guidance and Control for UAV Carrier Landing. *IEEE Transactions on Aerospace and Electronic Systems*, 55(2):951–966, April 2019.

[3] Douglas V. Smith. *One Hundred Years of U.S. Navy Air Power*. U.S. Naval Institute, 2010.

[4] J. M. Urnes and R. K. Hess. Development of the F/A-18A automatic carrier landing system. *Journal of Guidance, Control, and Dynamics*, 8(3):289–295, 1985.

[5] Ziyang Zhen, Shuoying Jiang, and Kun Ma. Automatic carrier landing control for unmanned aerial vehicles based on preview control and particle filtering. *Aerospace Science and Technology*, 81:99 – 107, 2018.

[6] Jovan Boskovic and Joshua Redding. An Autonomous Carrier Landing System for Unmannned Aerial Vehicles. In *AIAA Guidance, Navigation, and Control Conference*, 2009.

[7] Nicholas A. Denison. Automated Carrier Landing of an Unmanned Combat Aerial Vehicle Using Dynamic Inversion. Master's thesis, Air Force Institute of Technology, 2007.

[8] Ke Lu and Chunsheng Liu. A L1 Adaptive Control Scheme for UAV Carrier Landing Using Nonlinear Dynamic Inversion. *International Journal of Aerospace Engineering*, May 2019.

[9] G. Anitha and R.N. Gireesh Kumar. Vision Based Autonomous Landing of an Unmanned Aerial Vehicle. *Procedia Engineering*, 38:2250 – 2256, 2012. International Conference on Modelling Optimization and Computing.

[10] L. Coutard, F. Chaumette, and J. Pflimlin. Automatic Landing on Aircraft Carrier by Visual Servoing. In *2011 IEEE/RSJ International Conference on Intelligent Robots and Systems*, pages 2843–2848, Sep. 2011.

[11] Yang Gui, Pengyu Guo, Hongliang Zhang, Zhihui Lei, Xiang Zhou, Jing Du, and Qifeng Yu. Airborne Vision-Based Navigation Method for UAV Accuracy Landing Using Infrared Lamps. *Journal of Intelligent & Robotic Systems*, 72, 11 2013.

[12] S. Saripalli, J. F. Montgomery, and G. S. Sukhatme. Visually guided landing of an unmanned aerial vehicle. *IEEE Transactions on Robotics and Automation*, 19(3):371–380, June 2003.

[13] C. S. Sharp, O. Shakernia, and S. S. Sastry. A vision system for landing an unmanned aerial vehicle. In *Proceedings 2001 ICRA. IEEE International Conference on Robotics and Automation (Cat. No.01CH37164)*, volume 2, pages 1720–1727 vol.2, May 2001.

[14] O. A. Yakimenko, I. I. Kaminer, W. J. Lentz, and P. A. Ghyzel. Unmanned aircraft navigation for shipboard landing using infrared vision. *IEEE Transactions on Aerospace and Electronic Systems*, 38(4):1181–1200, Oct 2002.

[15] Yue Meng, Wei Wang, and Zhenxing Ding. Research on the visual/inertial integrated carrier landing guidance algorithm. *International Journal of Advanced Robotic Systems*, 15(2):1729881418764728, 2018.

[16] Brian L. Stevens, Frank L. Lewis, and Eric N. Johnson. *Aircraft Control and Simulation: Dynamics, Controls Design and Autonomous Systems*. John Wiley & Sons, Inc., 3rd edition, 2016.

[17] Atilla Dogan and William Blake. *Flight Mechanics of Aerial Refueling: Mathematical Modeling and Simulation*. The AIAA Press, 2010.

[18] NAVSEA Shipbuilding Support Office. Enterprise (CVN 65). Retrieved from `https://www.nvr.navy.mil/SHIPDETAILS/SHIPSDETAIL_CVN_65.HTML`, 2017. [Accessed on September 3, 2019].

[19] Joseph F. Sweger. Design Specifications Development for Unmanned Aircraft Carrier Landings: A Simulation Approach. Trident Scholar Project Report 316, United States Naval Academy, May 2003.

[20] CVN-65 Enterprise. Retrieved from `https://www.globalsecurity.org/military/systems/ship/cvn-65-schem.htm`. [Accessed on August 6, 2019].

[21] Marcello R. Napolitano. *Aircraft Dynamics: From Modeling to Simulation*. John Wiley & Sons, Inc., 2012.

[22] Ralph M. Garder and Lawrence V. Kirk. Conditional Inspections: Determination of Non-normal Landings. Retrieved from `http://www.boeing.com/commercial/aeromagazine/aero_14/conditional_story.html`. [Accessed on November, 2019].

[23] Fragaszy, Dorothy and Mangalam, Madhur. Tooling. *Advances in the Study of Behavior*, 50, April 2018.

[24] Mullins R. Baxter. MAE3405 Flight Dynamics, Lecture 5 Notes, University of Texas at Arlington, 2018.

[25] N-UCAS Advanced Development Program Office. Unmanned Combat Air System Shipboard Interface Reference Document. Technical Report NA-4150-USRD-1005, Naval Air Systems Command, February 2007.

[26] National Oceanic and Atmospheric Administration. WOCE Upper Ocean Thermal Data. Retrieved from https://www.nodc.noaa.gov/woce/woce_v3/wocedata_1/woce-uot/document/wmocode.htm, 2002. [Accessed on March 15, 2019].

[27] S. N. Singh, M. L. Steinberg, and A. B. Page. Nonlinear adaptive and sliding mode flight path control of F/A-18 model. *IEEE Transactions on Aerospace and Electronic Systems*, 39(4):1250–1262, Oct 2003.

[28] Jan Roskam. *Airplane Flight Dynamics and Automatic Flight Controls: Part I*. Design, Analysis and Research Corporation (DARcorporatin), 1998.

[29] Luat T. Nguyen, Marilyn E. Ogburn, William P. Gilbert, Kemper S. Kibler, Phillip W. Brown, and Perry L. Deal. Simulator Study of Stall/PostStall Characteristics of a Fighter Airplane With Relaxed Longitudinal Static Stability. Technical Paper 1538, NASA Langley Research Center, December 1979.

[30] Katsuhiko Ogata. *Modern Control Engineering*. Prentice Hall, Inc., 5th edition, 2010.

[31] Norman S. Nise. *Control Systems Engineering*. John Wiley & Sons, Inc., 7th edition, 2015.

[32] The Mathworks Inc. Trim: Find Trim Point of a Dynamic System. Retrieved from https://www.mathworks.com/help/simulink/slref/trim.html, 2019. [Accessed on July, 2019].

[33] Jean-Jacques E. Slotine and Weiping Li. *Applied Nonlinear Control*. Prentice-Hall, Inc., 1991.

[34] The Mathworks Inc. Exact Linearization Algorithm. Retrieved from https://www.mathworks.com/help/slcontrol/ug/exact-linearization-algorithm.html, 2019. [Accessed on July, 2019].

[35] Animesh Chakravarthy. AE5364 Guidance, Navigation and Control of Aerospace Vehicles, Lecture 9 Notes, University of Texas at Arlington, 2019.

[36] Frank L. Lewis, Draguna Vrabie, and Vassilis L. Syrmos. *Optimal Control*. John Wiley & Sons, Inc., 3rd edition, 2012.

[37] Yoshio Ebihara, Tomomichi Hagiwara, and Mituhiko Araki. Sequential tuning methods of LQ/LQI controllers for multivariable systems and their application to hot strip mills. *International Journal of Control*, 73(15):1392–1404, 2000.

[38] Arthur E. Jr. Bryson and Yu-Chi Ho. *Applied Optimal Control: Optimization, Estimation and Control*. Taylor & Francis Group, 1975.

[39] Yue Meng, Wei Wang, Hao Han, and Jingxuan Ban. A visual/inertial integrated landing guidance method for UAV landing on the ship. *Aerospace Science and Technology*, 85:474 – 480, 2019.

[40] Zhenhua Yang, Lixin Tang, and Lingsong He. A new analytical method for relative camera pose estimation using unknown coplanar points. *Journal of Mathematical Imaging and Vision*, 60:1–17, 06 2017.

[41] Bodo Rosenhahn, Christian Perwass, and Gerald Sommer. Foundations about 2D-3D Pose Estimation. Retrieved from `http://homepages.inf.ed.ac.uk/rbf/CVonline/LOCAL_COPIES/ROSENHAHN1/CVOnlinePose.html`. [Accessed on April 3, 2019].

[42] Carsten Steger. Algorithms for the Orthographic-n-Point Problem. *Journal of Mathematical Imaging and Vision*, 60(2):246–266, Feb 2018.

[43] K. Zhou, X. Wang, Z. Wang, H. Wei, and L. Yin. Complete initial solutions for iterative pose estimation from planar objects. *IEEE Access*, 6:22257–22266, April 2018.

[44] John L. Crassidis and John L. Junkins. *Optimal Estimation of Dynamic Systems*. Chapman & Hall/CRC Applied Mathematics and Nonlinear Science Series, 2nd edition, 2012.

[45] John Junkins, Declan Hughes, Karim Wazni, and Vatee Pariyapong. Vision-Based Navigation For Rendezvous, Docking And Proximity Operations. In *4th International Conference College of Aeronautics, Cranfield University*, volume 101, January 1999.

BIOGRAPHICAL STATEMENT

Metin Kus was born in Istanbul, Turkey, in 1993. He completed his B.Sc. degree in mechanical engineering at the Middle East Technical University as a high honor student, in 2016. He worked for Turkish Aerospace Industries, Inc. as a design engineer after graduation. In 2017, he was appointed for an M.Sc. degree program in aerospace engineering at the University of Texas at Arlington, in which Turkish Aerospace Industries, Inc. sponsored him to study on the autonomous takeoff/landing of air vehicles. He discovered his interest in flight dynamics and nonlinear aircraft control during this program and is currently working on sliding mode control and novel estimation algorithms to improve upon the findings of his master's thesis.